Doctoral Dissertation

博士論文

Mechanisms and impacts of salinity anomalies associated with the positive Indian Ocean Dipole

(正のインド洋ダイポールモード現象に伴う塩分変動のメカニズムおよびインパクト)

A Dissertation Submitted for the Degree of Doctor of Philosophy

December 2019

令和元年12月博士（理学）申請

Department of Earth and Planetary Science, Graduate School of Science, The University of Tokyo

東京大学大学院理学系研究科

地球惑星科学専攻

Shoichiro Kido

木戸　晶一郎

Abstract

Accompanied by the anomalous atmospheric circulation and precipitation pattern, surface and subsurface salinity in the tropical Indian Ocean are known to undergo significant variations associated with the Indian Ocean Dipole (IOD), which is a dominant climate mode in the tropical Indian Ocean. Though recent advances in salinity observation have revealed many interesting features of salinity variations in the tropical oceans, comprehensive descriptions of underlying physical processes and their impacts on the upper ocean fields, such as sea surface temperature (SST) and currents are yet to be established. Thus, this thesis is devoted to quantitatively elucidate the mechanisms and impacts of salinity variations in the tropical Indian Ocean, with a particular emphasis on their link with the IOD.

Through analyses of observational datasets, it is found that negative (positive) sea surface salinity (SSS) anomalies appear in the central-eastern equatorial Indian Ocean (southeastern tropical Indian Ocean) during the mature phase of the positive IOD (pIOD) events. In addition to SSS, significant variations in the subsurface salinity are also detected, with distinct saltening (freshening) in the eastern equatorial Indian Ocean (southern tropical Indian Ocean). The main driver of these surface and subsurface salinity variation is the IOD, rather than the remote influences from the El Niño-Southern Oscillation (ENSO).

Mechanisms of salinity anomalies associated with the pIOD are then investigated through a series of sensitivity experiments and an online budget analysis using a regional ocean model. The results from sensitivity experiments show that anomalous surface saltening in the southeastern tropical Indian Ocean are primarily caused by reduction in precipitation and partly by enhanced evaporation due to increased wind speed, while surface freshening in the central-eastern equatorial

Indian Ocean are generated by zonal advection anomalies induced by anomalous wind stress, consistent with previous studies. Completely new results are that the modulation of nonlinear salinity advection associated with mesoscale eddies also plays an important role in determining the spatial pattern of SSS anomalies, especially in the southeastern tropical Indian Ocean. On the other hand, subsurface salinity anomalies are almost entirely caused by wind stress effects mediated by ocean dynamical processes. Further decomposition of advective anomalies suggests that they are mainly explained by the pIOD-related current anomalies governed by equatorial wave dynamics. However, a vertical shift of nonlinear freshening due to high-frequency variability also substantially contributes to the generation of subsurface saltening in the eastern equatorial Indian Ocean. The significance of low-frequency modulation of the rectified effects due to high-frequency variability is further justified by an additional set of sensitivity experiments using a linear continuously stratified ocean model (LCSM), which isolates the essential physics under a simple framework. It is shown that large-scale oceanic changes in response to the pIOD-related atmospheric anomalies are the key drivers of the observed salinity anomalies, while some nonlinear effects also seem to be at work.

Impacts of salinity anomalies associated with the pIOD-related salinity anomalies are assessed through observational data analysis. It turns out that density stratification in the eastern equatorial Indian Ocean is enhanced due to anomalous surface freshening and subsurface saltening during the pIOD. On the other hand, surface saltening and subsurface freshening in the southeastern tropical Indian Ocean leads to weakening of density stratification there. By decomposing observed densities into contribution from temperature and salinity anomalies, it is shown that the contribution from anomalous salinity stratification mentioned above is comparable to that from anomalous thermal stratification. Furthermore, a regression analysis of SST evolution against salinity anomalies, as well as the singular value decomposition analysis between them, implies that enhanced stratification in

the eastern equatorial Indian Ocean may lead to SST warming there.

To quantify the impacts of these pIOD-related salinity anomalies, we have carried out novel sensitivity experiments using the regional ocean model and detailed diagnostics of heat and momentum budget. During the pIOD, the enhanced stratification in the eastern equatorial Indian Ocean causes momentum inputs from the wind forcing to be more strongly trapped in the surface layer, and zonal and vertical current anomalies to be more confined to the upper layer. As a result, upward transports of cold water from below the thermocline to the surface layer are significantly suppressed, and the cooling in the eastern-equatorial Indian Ocean is suppressed by as much as 1.0°C. The above arguments are further corroborated by a set of sensitivity experiments using a linear continuously stratified ocean model, which can isolate the effect of stratification change caused by salinity anomalies associated with the pIOD, detected by the regional ocean model experiments. Our results suggest that salinity does play an active role in the evolution of the pIOD, rather than being passively affected by large-scale anomalous atmospheric and oceanic conditions.

Acknowledgements

Most of all, I am deeply indebted to my supervisor, Tomoki Tozuka for his supervision of this work. He gave me a lot of useful suggestions on my work and provided valuable advice for writing this thesis. Without his patient encouragement, I could not complete my Ph.D work. I also express my sincere gratitude toward his former and current group members, Takahito Kataoka, Shun Ohishi, Yoko Yamagami, Satoru Endo, Chiho Tanizaki, Marvin Seow Xiang Ce, Kazumichi Murata, Ryo Kobayashi, Natsumi Tanuma, Hidehiro Kusunoki, Mai Nakazato, and Lianyi Zhang for their helpful discussions and support.

I am also grateful to the dissertation committee members, Yukio Masumoto, Toshiyuki Hibiya, Ichiro Yasuda, and Yu Kosaka for their constructive comments, which lead to significant improvement of this thesis. In particular, their suggestion to construct schematic diagrams leads to clear illustration of the essence of each chapter. Critical comments from Toshio Yamagata, Masahide Kimoto, Hisashi Nakamura, Kaoru Sato, Masahiro Watanabe and Hiroaki Miura are also greatly appreciated.

Significant part of his work has been conducted when I stayed the Department of Atmospheric and Oceanic Sciences (ATOC) at the University of Colorado, Boulder in the summer of 2018. I would like to sincerely thank Weiqing Han for her warm advice and guidance during my stay. My thanks also goes to members of Weiqing's group, Yuanlong Li, Lei Zhang, Xiaolin Zhang, Yun Qiu, Wen Xing, Gang Wang, and Jason B. West for their kind supports and comments during the group seminars. I also thank Aixue Hu, Qing Hu, and Kelly Duong for their hospitality during my visit.

This thesis is benefited from stimulus and fruitful discussions with following people: Hidenori Aiki, Kentaro Ando, H. Annamalai, Kunihiro Aoki, Swadhin K. Behera, Andrew Delman,

Takeshi Doi, Yan Du, Ming Feng, Katsutoshi Fukuzawa, Takanori Horii, Takashi Ijichi, Iskhaq Iskandar, Shota Katsura, Tsubasa Kohyama, Takahiro Kusumi, Tong Lee, Chorong Lee, Hailong Liu, Jing-Jia Luo, Christophe Maes, Takuro Matsuta, Julian P. McCreary, Shoshiro Minobe, Yushi Morioka, Taira Nagai, Akira Nagano, Motoki Nagura, Matthew Newman, Masami Nonaka, Ebenezer Nyadjro, Tomomichi Ogata, Yohei Onuki, Bo Qiu, Tangdong Qu, Kelvin Richards, Hideharu Sasaki, Yoshinori Sasaki, Niklas Schneider, Toshiaki Shinoda, Janet Sprintall, Shusaku Sugimoto, Bunmei Taguchi, Anne Takahashi, Yuki Tanaka, Hiroki Tokinaga, Iwao Ueki, Jérôme Vialard, P.N. Vinayachandran, Yuhong Zhang, Linlin Zhang, and Lei Zhou. Their critical comments and constructive suggestions greatly led to improvement of the present work. I also thank all past and present members of Atmospheric and Oceanic Science Group for their valuable comments, encouragement, and help.

I would like to acknowledge the financial support by Research Fellowship of Japan Society for the Promotion of Science (JSPS) and Research Fellowship of Leading Graduate Course for Frontiers of Mathematical Sciences and Physics, MEXT, Japan.

Contents

Chapter 1

General introduction

Chapter 1: General introduction

1.1 Air-sea interaction in the tropics

Due to its large area and strong variability owing to high sea surface temperature (SST), the tropics serve as a pacemaker of the global climate. In particular, the El Niño-Southern Oscillation (ENSO), which refers to an interannual fluctuation of the trade winds and zonal SST gradient in the tropical Pacific, is the most prominent climatic signal on Earth (Hartmann, 2016; Philander, 1990). Changes in the atmospheric circulation and precipitation pattern associated with the ENSO cause catastrophic disasters (e.g. flood, drought, and heatwaves) over many countries surrounding the Pacific Ocean. In addition, anomalous atmospheric conditions in the tropical Pacific are transmitted to extratropics via teleconnection and affect local weather and climate all over the world (Horel & Wallace, 1981; Trenberth et al., 1998). Furthermore, changes in the ocean circulation associated with the ENSO, such as the modulation in the strength of coastal upwelling, have profound impacts on marine ecosystems and fisheries in many regions (Stenseth, 2002). For these reasons, its accurate understanding and prediction are of great importance not only for scientific interests but also from a socioeconomic viewpoint.

It is now well recognized that the interaction between the ocean and the atmosphere plays a fundamental role in determining the mean state and variability of the tropics, as represented by the ENSO. In his seminal work, Bjerknes (1969) has first pointed out that the ENSO is amplified by the positive feedback owing to an air-sea interaction. When an El Niño occurs, positive SST anomalies in the eastern equatorial Pacific excite an anomalous convection and diabatic heating in the overlying atmosphere and induce westerly wind anomalies to the west. The westerly wind anomalies excite downwelling oceanic Kelvin waves, which propagate eastward and push the thermocline downward. Resulting weakening of upwelling in the east suppresses the intake of cold water to the surface layer and is conducive to the growth of the initial positive SST anomalies, giving rise to further

amplification of them. This positive feedback, which involves a circular chain of atmospheric and oceanic processes, is now widely recognized and referred to "Bjerknes feedback". After the discovery, significant progresses have been made in understanding the basic features and mechanisms of amplification/decay of air-sea coupled modes in the tropics (Hirst, 1986; Philander et al., 1984). In particular, several conceptual model of the ENSO, such as the delayed oscillator (Battisti & Hirst, 1989; Schopf & Suarez, 1988), the zonal advective oscillator (Picaut et al., 1996), and the recharge-discharge oscillator (Jin, 1997), have been proposed to explain its key properties including turnarounds (see review by Neelin et al. (1998) and references therein). These theoretical works, as well as many observational and modeling studies, have paved the way to deeper understanding and skillful prediction of the ENSO (McPhaden et al., 2006). At the same time, some "brothers of El Niño", which has their roots in similar, but not identical coupled feedbacks to the ENSO, have been discovered in other basins, such as the Atlantic zonal mode (Zebiak, 1993) in the tropical Atlantic Ocean and the Indian Ocean Dipole (IOD; Saji et al 1999, Webster et al. 1999) in the tropical Indian Ocean (IO). The existence of climate modes with unstable air-sea interaction is also detected in some subtropical coastal areas, such as the Benguela Niño (Richter et al., 2010; Shannon et al., 1986) and the Ningaloo Niño (Feng et al., 2013; Kataoka et al., 2014), and dubbed as the "coastal Niño". All of these finding have significantly contributed to improvements in the predictability of regional and global climate variations at seasonal to interannual timescales.

As described in the explanation of the Bjerknes feedback, the growth and decay of the air-sea coupled mode are achieved by the two-way communication between the atmosphere and the ocean, namely, the *atmospheric response to SST anomalies* and the *oceanic change in response to the anomalous atmospheric forcing*. Thus, from the standpoint of the oceanography, a key question that should be addressed is how and to what extent, anomalous atmospheric forcing can exert

influences on the upper ocean fields and generate SST anomalies. The temperature of the ocean is determined by intricate balance between dynamical (e.g. advective and diffusive heat transport) and thermodynamical (e.g. heat input at the sea surface) processes. To highlight the key point of our discussion below, we note that there are three information that are delivered by the atmosphere to the ocean; namely, the momentum, heat, and freshwater fluxes across the air-sea interface, as schematically illustrated in Fig. 1.1.

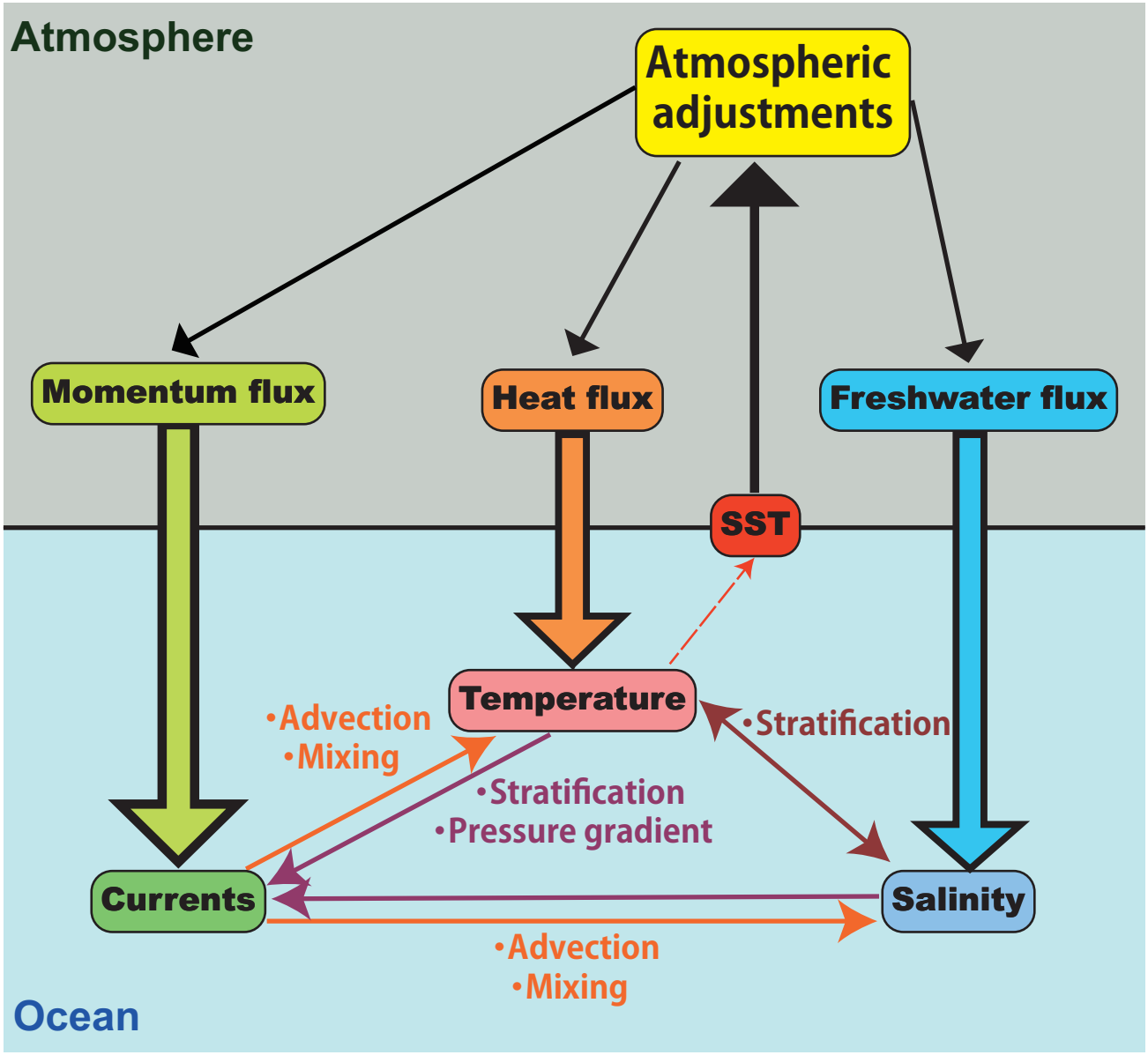

Figure 1.1: Schematic diagram illustrating air-sea interaction processes operating in the tropics. See the main text for details.

Among the three factors, the dynamical wind forcing is believed to be the dominant contributor to the SST evolution. For example, as exemplified in the explanation of the Bjerknes feedback, changes in momentum fluxes into the ocean associated with wind stress anomalies modulate advective heat transports by the upper ocean currents and contribute to the generation of SST anomalies. The momentum flux anomalies could also affect the SST by altering the strength of vertical mixing and mixed layer depth (MLD). Indeed, changes in the MLD are important to the formation of SST anomalies in various regions (e.g. Alexander et al., 2000; Kataoka et al., 2019; Morioka et al., 2010; Tozuka & Cronin, 2014).

Heat flux anomalies also alter the evolution of SST through thermodynamical processes. For example, changes in the wind speed lead to those in turbulent (i.e., sensible and latent) heat fluxes across the sea surface. Specifically, accelerated (decelerated) wind speed at the surface implies greater (smaller) loss of turbulent heat flux to the atmosphere and leads to anomalous surface cooling (warming) Associated changes in SST may lead to further changes in wind speed and amplify the original wind anomalies. This positive feedback is referred to the wind-evaporation-SST (WES) feedback (Xie & Philander, 1994), and invoked to explain many observed features and variations seen in the tropics (Chang et al., 1997; Vimont et al., 2003). Also, the cloud is one of the essential elements in the air-sea coupling, and its changes can reduce or increase the amount of shortwave and longwave radiation reaching to the surface and modulate the heat balance. The cloud-SST feedback is known to operate as both positive (Klein & Hartmann, 1993; T. Li & Philander, 1996) and negative feedback (T. Li et al., 2000; Ramanathan & Collins, 1991), depending on the type of clouds.

Different from momentum and heat fluxes, freshwater flux anomalies do not have a direct influence on the SST, but they do alter the upper ocean salinity. Given that salinity variations have

potential to modulate the current and temperature of the upper ocean (a detailed discussion on this issue will be provided in section 1.3), it is reasonable to conjecture that there are some feedback processes mediated by freshwater flux, salinity, and SST anomalies. Salinity may also be linked to other air-sea coupled feedbacks, as it is also closely linked to many dynamical and thermodynamical processes. To portray these distinctive roles played by salinity, we will discuss the mechanisms governing salinity variation in the tropics and how they are linked to other components of the climate system in the following two sections.

1.2 A brief overview of salinity research in the tropics

The ocean salinity, as well as temperature, is a key parameter in physical oceanography. Its spatiotemporal variation is determined by a complex balance between freshwater flux (precipitation, evaporation, and river runoff) and three-dimensional advection and mixing mediated by the ocean dynamics. This can be inferred from Fig. 1.2, which displays the annual mean climatology of freshwater flux (precipitation minus evaporation) and sea surface salinity (SSS). Generally speaking, regions with positive freshwater flux (i.e. precipitation is larger than evaporation), such as the equatorial region, have lower SSS, while regions with higher SSS tend to collocate with those with negative freshwater flux (e.g. subtropical oceans). However, the correspondence between the two parameters is not exact, implying the presence of ocean dynamical processes. Since temperature and salinity control the density of the seawater, understanding their spatiotemporal variations is crucial for an accurate description of many physical processes operating in the ocean.

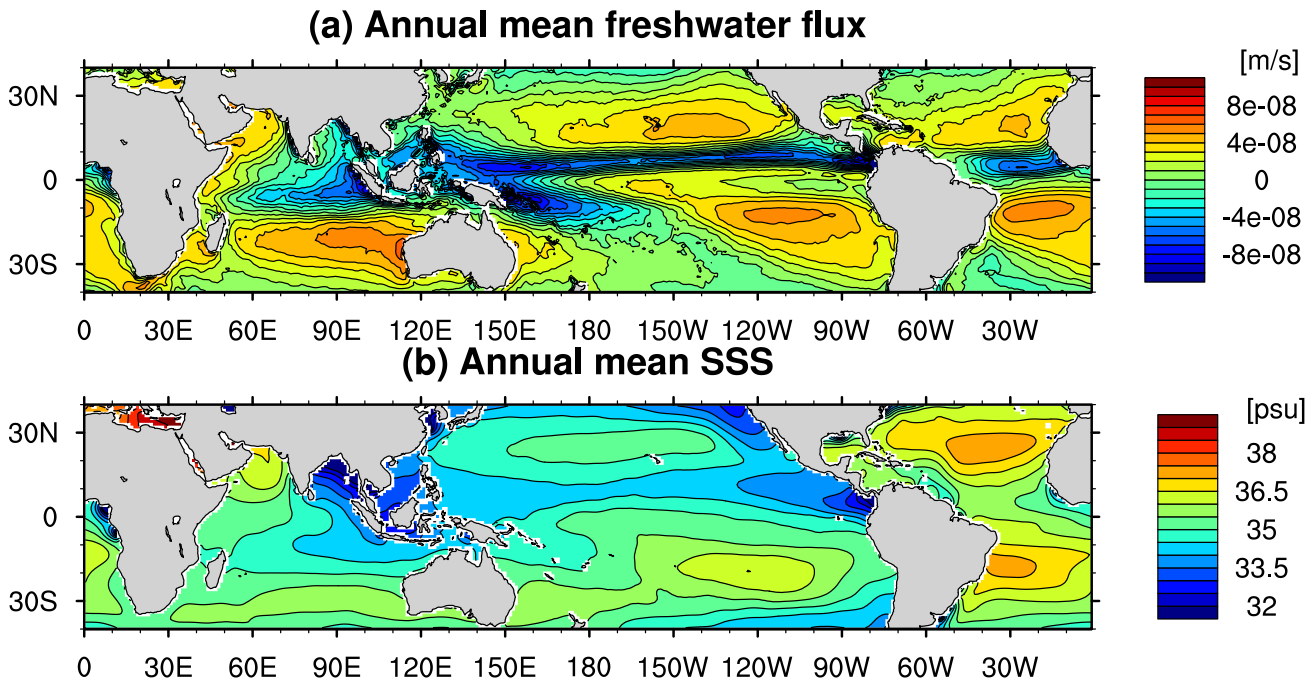

Figure 1.2: Annual mean of freshwater flux (evaporation minus precipitation) (a: in [m/s]) and sea surface salinity (SSS) (b: in [psu]). For precipitation, we use the Tropical Rainfall Measuring Mission's (TRMM) 3b43 V7 product (Kummerow et al., 1998), while the Objectively Analyzed air-sea FLUXes (OAFLUX) product (L. Yu & Weller, 2007) is adopted for evaporation, and the period of both data is 1999-2013. For SSS, the climatology of the World Ocean Atlas 2013 (Zweng et al., 2013) is used.

Though tremendous efforts have been made to clarify the mechanisms of temperature variability and its links with air-sea interaction (for example, see review by Deser et al., 2010), salinity has received less attention due to scarcity of observational data and absence of its direct impacts on the atmosphere. Before the late 1980s, observational studies on salinity variation have relied only on the data from research cruises and merchant ships, whose resolutions were very sparse both in time and space. Also, salinity has been taken to be constant or not explicitly treated in many numerical ocean models at that time.

The situation has rapidly changed from the late 1980s to the early 1990s. The intensive observational program conducted in the tropical Pacific (the Tropical Ocean-Global Atmosphere: TOGA program) (Webster & Lukas, 1992) led to the identification of strong salinity stratification in the upper ocean (Godfrey & Lindstrom, 1989; Lukas & Lindstrom, 1991). For example, Lukas and Lindstrom (1991) pointed out that the excess of precipitation over evaporation and the subduction of salty water from subtropics generate strong salinity stratification in the western tropical Pacific. Such salinity stratification in the upper ocean plays a key role in determining MLD, which controls the effective heat capacity of the surface water. The layer between the mixed layer and the isothermal layer is often called "barrier layer", since it prevents entrainment of the cold water below the thermocline like a barrier. Subsequently, Sprintall and Tomczak (1992) demonstrated that the barrier layer also exists in other tropical and subtropical oceans. After the identification of the barrier layer, numerous observational (Ando & McPhaden, 1997; Delcroix & Hénin, 1991; Picaut et al., 1996) and modeling studies (Vialard & Delecluse, 1998) have examined the upper ocean salinity variability in the tropical Pacific and discussed its relation to the ENSO, though their descriptions were rather qualitative.

Advances in salinity observation and improvement of numerical ocean models in the 2000s have provided further opportunities to obtain more comprehensive insights into ocean salinity in the tropics. The accumulation of data from Argo profiles and satellite observation of SSS, as well as improved estimate of freshwater fluxes over the open oceans, enabled us to explore the variability of salinity and related physical processes responsible on various temporal scales, including diurnal (Drushka et al., 2014), intraseasonal (T. Lee et al., 2012; Y. Li et al., 2015), seasonal (Bingham et al., 2012; Ren & Riser, 2009), interannual (Hasson et al., 2013; Katsura et al., 2013), and decadal timescale (Cravatte et al., 2009; Du et al., 2015). In addition, long-term trends in the upper ocean

salinity have been detected by various observational datasets (Boyer et al., 2005; Durack & Wijffels, 2010; Hosoda et al., 2009), and their relations with changes in global hydrological cycle associated with global warming have received broad attentions from science community (Durack et al., 2012, 2013). Recently, links of salinity with mesoscale eddies have also been discussed extensively (Delcroix et al., 2019; Melnichenko et al., 2017).

As described above, considerable progresses have been made in understanding features and mechanisms of salinity variability in recent decades. However, we are still on our way to obtain the complete picture, as there are several unsolved issues. In particular, more quantitative assessments of processes contributing to the observed salinity variations, as well as accurate descriptions of interactions among phenomena with different timescales, are necessary to further understand the multiple aspects of salinity variation.

1.3 Role of salinity in the tropical climate variability

How, and to what extent, does salinity affect the physical processes in the upper ocean and the climate system? There are two major pathways that connect salinity with other upper ocean variables (Fig. 1.3). First, changes in stratification due to salinity anomalies affect the strength of vertical mixing in the upper ocean and alter vertical transports of heat, freshwater and momentum (Miller, 1976) (Fig. 1.3a). Second, changes in pressure gradient generated by density perturbation due to salinity modulate current and associated transport of tracers and momentum, thereby giving rise to changes in temperature and ocean circulation (Cooper, 1988; Han et al., 2001; Howden & Murtugudde, 2001) (Fig. 1.3b). In the real ocean, these two processes coexist and reinforce or compensate each other. In addition, the resulting changes in motions of the fluid and density fields may in turn, alter the original salinity anomalies. Thus, the detection of these elusive signals arising from mutual interactions between several processes is not an easy task, particularly from

observational datasets alone. For this reason, many researchers have relied on numerical ocean general circulation models (OGCMs) to tackle this formidable problem.

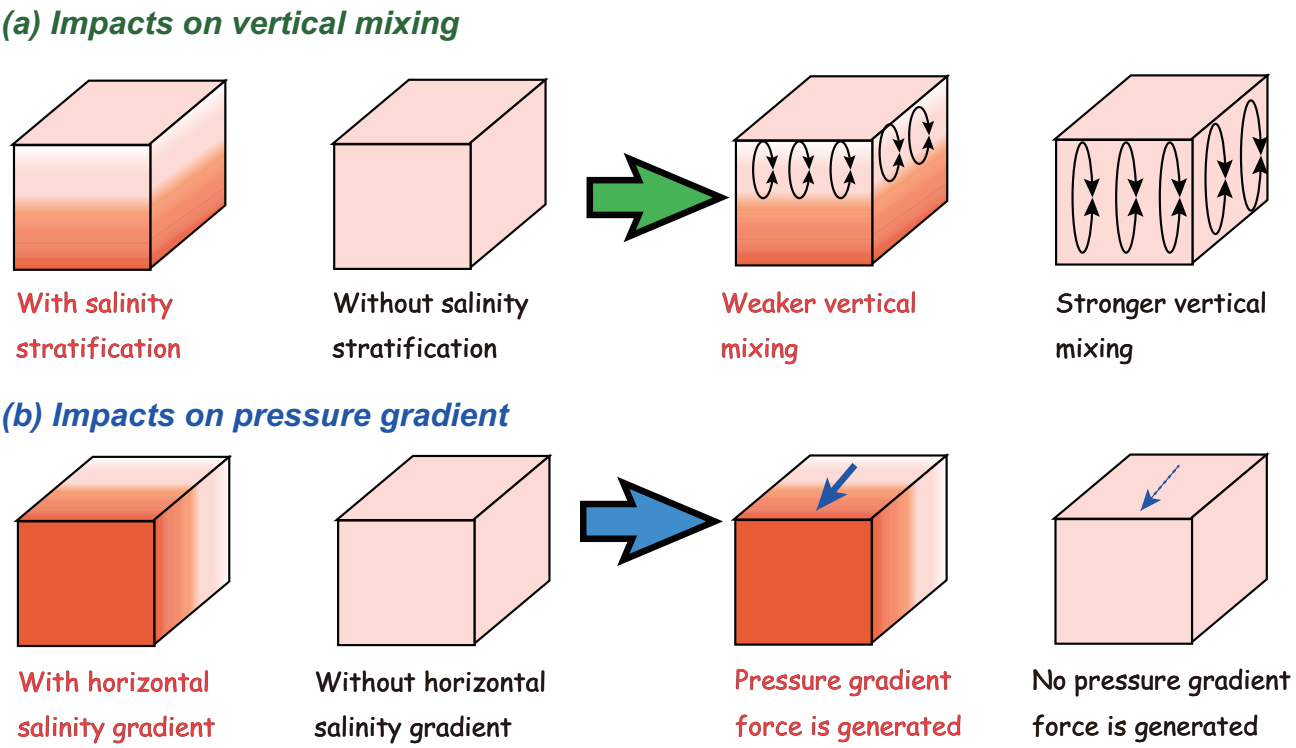

Figure 1.3: Schematic diagrams describing the impacts of (a) vertical and (b) horizontal salinity gradient on the upper ocean conditions. See the main text for details.

The pioneering work by Cooper (1988) attempted to investigate the role of salinity using an OGCM with a particular focus on the tropical IO. By switching on and off the salinity effects in his model, he has highlighted the importance of pressure gradient force generated by horizontal gradients of salinity in controlling the upper ocean circulation. A similar approach has been applied to other tropical oceans to assess the impacts of salinity (Carton, 1991; R. R. Murtugudde & Busalacchi, 1998). After the aforementioned identification of strong salinity stratification and associated barrier layer in the western tropical Pacific in the early 1990s (Lukas & Lindstrom, 1991; Sprintall & Tomczak, 1992), the impacts of salinity stratification on vertical mixing have been

discussed by comparing OGCM simulations with and without dependence of vertical mixing coefficients on salinity stratification. For example, Vialard and Delecluse (1998) have shown that salinity stratification in the western equatorial Pacific leads to stronger eastward current by trapping the momentum injected by wind anomalies. This technique has been used by various studies that discussed the role of salinity stratification and barrier layer in the tropical oceans (Maes, 2002; Maes et al., 2005; Masson et al., 2003, 2004, 2005). However, these experiments have been designed to assess the collective effects of salinity stratification, which contain contributions from both mean and anomaly. For this reason, the specific impacts of salinity anomalies generated by large-scale climate modes are not properly isolated by that approach.

As discussed above, isolating the specific role played by salinity is not straightforward, due to the complex interactions among various factors. Even though many studies have demonstrated the importance of salinity assimilation into operational seasonal prediction systems of the ocean and climate (Ballabrera-Poy et al., 2002; Hackert et al., 2011; Zhu et al., 2015), the physical processes behind them have not been fully understood in many cases. In this study, we will address these issues through a series of regional ocean model experiments with a novel strategy, focusing on the salinity variation associated with the IOD. In the next section, we will review the current status of our understanding of salinity variability in the tropical IO and its relation to large-scale climate modes.

1.4 Salinity variability in the tropical Indian Ocean

As seen in Fig. 1.2, there is a remarkable zonal SSS gradient in the tropical IO, similar to the tropical Pacific. Regions with strong salinity stratification in the upper ocean are also widely observed in the tropical IO, particularly near the equator and the Bay of Bengal (Qu & Meyers, 2005). Given that links between salinity variations and the large-scale climate mode (i.e., ENSO) are

found in the tropical Pacific, it is natural to ask whether salinity also plays an active role in the interannual variability of the tropical IO. Indeed, significant surface (Fig. 1.4a) and subsurface (Fig. 1.4b) salinity variation are observed in the tropical IO, and it is of great interest to investigate their origins.

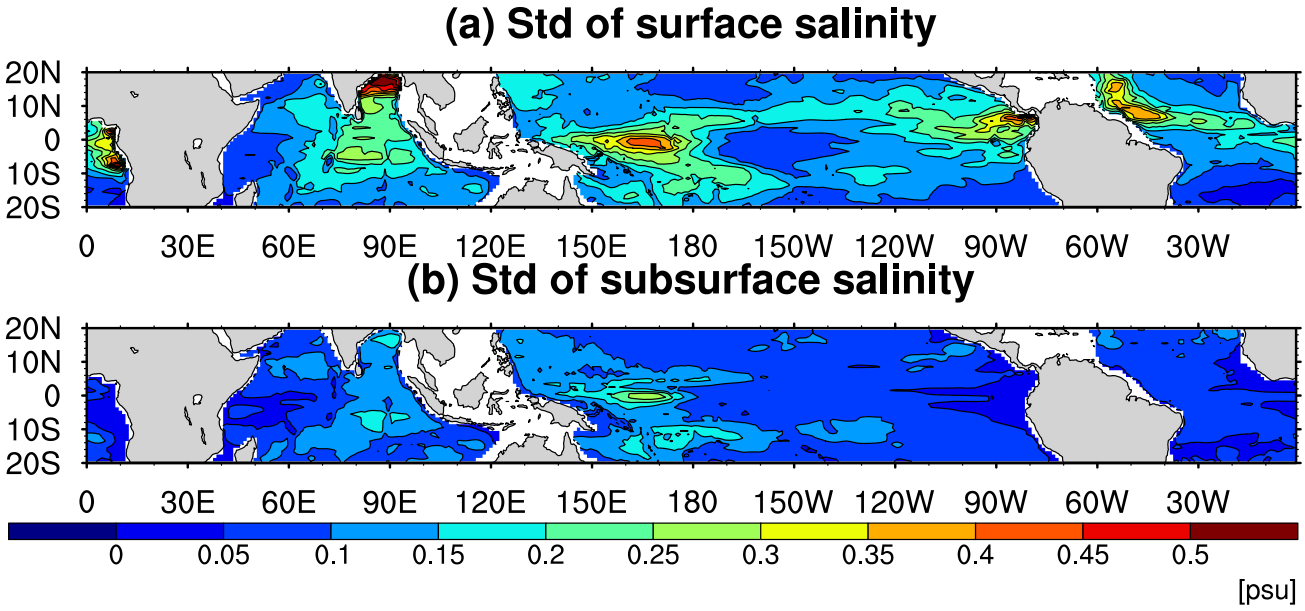

Figure 1.4: Standard deviation of surface (vertically averaged from 0 [m] to 30 [m] depth) and subsurface (vertically averaged from 50 [m] to 100 [m]) salinity anomalies in the tropics with monthly climatology removed. The gridded Argo data (Roemmich & Gilson, 2009) is used for the period from 2004 to 2015.

Similar to the ENSO in the tropical Pacific, the IOD serves as a dominant climate mode in the tropical IO (Saji et al., 1999; Webster et al., 1999). When a positive IOD (pIOD) event occurs, SST in the southeastern (western) tropical IO becomes anomalously low (high), with its peak in boreal fall (September to November). Accompanied by these SST anomalies, anomalous easterly wind is observed along the equator and the eastern (western) part of the tropical IO receives less

(more) precipitation than usual. Since SST anomalies associated with the IOD exert strong impacts on precipitation in the IO rim countries as well as the global climate (e.g., Saji & Yamagata, 2003), its accurate understanding and prediction is of great importance.

Due to much fewer salinity observation and difficulty in accurate simulation of salinity distribution in OGCMs, little is known about salinity variability in the tropical IO compared to the tropical Pacific. However, the recent increase in our ability to monitor salinity led to identification of the link between SSS and the IOD (Grunseich et al., 2011; Thompson et al., 2006). According to their results, negative (positive) SSS anomalies emerge in the central-eastern equatorial (southeastern tropical) IO in concert with the development of the pIOD. These SSS anomalies are caused not only by anomalous rainfall, but also by changes in the ocean circulation associated with the pIOD (J. Li et al., 2016; Y. Zhang et al., 2013). Anomalies with the opposite sign also appear during the negative IOD (nIOD) (Grunseich et al., 2011; Sun et al., 2019). These SSS signals are also captured by recent satellite salinity observation (Du & Zhang, 2015; Durand et al., 2013), and seen in a coupled model that can simulate the IOD-like variability (Vinayachandran & Nanjundiah, 2009). In addition, Qiu et al. (2012) found that variability of barrier layer thickness in the tropical IO is closely linked to the occurrence of the IOD by analyzing Argo data. They pointed out that variability of barrier layer thickness is primarily controlled by that of isothermal layer depth, and argued that it may affect the strength of the thermocline feedback, which plays an important role in the generation of SST anomalies.

The impacts of salinity on the IOD have been also investigated by several studies (J. Li et al., 2018; Masson et al., 2004; Y. Zhang et al.., 2016). However, these studies have focused only on a specific aspect (e.g. salinity impacts on the strength of vertical mixing, salinity contribution to pressure gradient) and not considered integrated effects of salinity and quantified their relative

importance. Therefore, our understanding on the roles played by salinity in the IOD is still fragmental and a more comprehensive study is required.

1.5 The purposes of the present thesis

As reviewed above, recent advancements of observational platforms and numerical ocean models lead to a rapid progress in our understanding of ocean salinity, especially in the tropical Pacific. This situation also applies to the tropical IO, but the endeavor to clarify the mechanisms and roles of salinity is still on the way and there remain several issues that warrant further investigation. Specifically, though qualitative descriptions of various factors contributing to salinity variations in the tropical IO have been provided by a large body of literatures, quantitative assessments of these processes are yet to be conducted. In addition, the extent to which salinity anomalies modulate the ocean circulation and SST is not conclusive and rigorously quantified, though many previous studies have speculated that they may have significant impacts on the upper ocean dynamics of the IO. Motivated by these situations, the mechanisms and impacts of interannual variability of salinity in the tropical IO are investigated , with a specific emphasis on their link to the IOD. In this thesis, we set the following two scientific questions that should be addressed:

(i) What is the relative importance of various factors responsible for the observed salinity anomalies associated with the IOD? Are there any important processes overlooked by previous studies?

(ii) Are there any significant impacts of the IOD-related salinity anomalies on the upper ocean circulation and SST? If so, how large are they?

The rest of this thesis is organized as follows. In the next chapter, we will first investigate the observed salinity variation associated with the IOD using observational dataset and an ocean reanalysis product. Then, using a regional ocean model that can realistically simulate the observed

features, we conduct salinity budget analysis and a series of sensitivity experiments to understand the mechanisms responsible for these salinity anomalies. Further decomposition of advective anomalies and an additional set of sensitivity experiments using a linear continuously stratified ocean model (LCSM) are performed to elucidate the physical processes behind them. After identifying the essential processes determining the salinity anomalies, we quantify their impacts through analysis of observational datasets and a novel sensitivity experiments in Chapter 3. We also used the LCSM in this chapter to confirm the validity of our findings. Summary of findings and discussion, will be presented in the final chapter.

Chapter 2

Features and mechanisms of salinity variation associated with the positive IOD

This chapter has been published as:

1. Kido, S., & Tozuka, T. (2017). "Salinity variability associated with the positive Indian Ocean Dipole and its impact on the upper ocean temperature", *Journal of Climate*, 30, 7885-7907, doi: https://doi.org/10.1175/JCLI-D-17-0133.1

2. Kido, S., Tozuka, T., & Han, W. (2019). "Anatomy of salinity anomalies associated with the positive Indian Ocean Dipole", *Journal of Geophysical Research: Oceans*, 124. doi; https://doi.org/10.1029/2019JC015163

2.1. Introduction

As discussed in Chapter 1, the Indian Ocean Dipole (IOD) is known as a dominant climate mode of the tropical Indian Ocean (IO) (Saji et al., 1999; Webster et al., 1999). During a positive IOD (pIOD) event, easterly wind anomalies along the equator strengthen the coastal upwelling along the Sumatra-Java coast, leading to a significant surface cooling in the eastern equatorial IO (EEIO) (Ragu Murtugudde & Busalacchi, 1999). At the same time, downwelling Rossby waves excited by these wind anomalies propagate westward and depress the thermocline in the western tropical IO, giving rise to anomalous warming there (L. Yu & Rienecker, 1999). The resulting SST anomalies with a dipole structure modulate the sea level pressure (SLP) and instigate further intensification of the original wind anomalies. As mentioned above, the IOD is amplified by a positive air-sea coupled feedback, analogous to the Bjerknes feedback described in Section 1.1 (Saji et al., 1999). Due to the seasonal change in the strength of the air-sea coupling in the tropical IO, a typical pIOD tends to be initiated during boreal spring and summer, and then reach its peak in boreal fall (September-November), followed by a rapid termination during boreal winter (Annamalai et al., 2003; T. Li et al., 2003). As the ocean plays a pivotal role in the evolution of the IOD, it is crucial to accurately understand the related oceanic processes.

The signature of the IOD in the IO can be identified in various oceanic variables, such as upper ocean temperature, salinity, sea level height, and current (S. A. Rao et al., 2002; S. A. Rao & Behera, 2005; Schott et al., 2009; Thompson et al., 2006). The mechanisms responsible for these observed oceanic signals have been extensively investigated since the discovery of the IOD (Delman et al., 2018; Halkides & Lee, 2009; T. Li et al., 2002; Vinayachandran et al., 2002). Among others, recent advancement of in-situ and satellite observations enables us to explore salinity variability associated with the IOD (Durand et al., 2013; Grunseich et al., 2011; Y. Zhang et al., 2013). During

positive IOD (pIOD) years, significant decrease in sea surface salinity (SSS) is observed in the central-eastern equatorial IO, while the southeastern tropical IO (SEIO) experiences anomalous saltening near the surface (J. Li et al., 2016; Thompson et al., 2006; Y. Zhang et al., 2013). In addition, Qiu et al. (2012) documented prominent changes in the barrier layer thickness over the tropical IO during IOD events based on the Argo profiles. However, less has been known regarding subsurface salinity variations, though it is well known that subsurface temperature undergoes significant variation associated with the IOD (S. A. Rao et al., 2002; S. A. Rao & Behera, 2005). Given that the ocean processes plays a critical role in the growth and decay of the IOD, an accurate description of salinity variation, including its vertical structure, and understanding of their generation mechanisms are important for the IOD itself.

There are several factors that are significantly affected by the IOD and have potential to alter the upper ocean salinity. Anomalous atmospheric conditions associated with the IOD, such as the weakening or reversal of equatorial zonal wind, variation of precipitation pattern due to the shift of convection center, and modulation of wind speed, all affect ocean current and air-sea freshwater fluxes, and thereby contribute to the evolution of salinity anomalies. Though many studies have pointed out the importance of anomalous winds and precipitation in causing salinity variations in a qualitative manner, quantitative understanding of their relative contribution to observed salinity anomalies has not been fully established.

To identify the key processes governing the evolution of salinity anomalies, salinity budget analysis has been widely used. For the IOD-related SSS anomalies, Y. Zhang et al. (2013) performed a mixed-layer averaged salinity budget analysis using an ocean reanalysis product. They found that positive SSS anomalies in the SEIO during the pIOD are primarily due to reduction of freshwater flux, while negative SSS anomalies along the central-eastern equatorial IO is caused by reduced

eastward advection of high salinity water from the Arabian Sea. These results were further confirmed by a modeling study of J. Li et al. (2016). However, their results based on a reanalysis product are hampered by a large residual term arising from uncertainties in the estimation of each processes and absence of direct computation of the vertical salinity diffusion term. The difficulty in closing salt budget using observational data or outputs from reanalysis products (so-called "offline analysis") is well-known and hinders accurate assessment of physical processes at work. In their modeling study of the tropical Pacific, Hasson et al. (2013) showed that salinity budget terms estimated from monthly outputs (i.e. the offline estimates) differ largely from those directly obtained by an online calculation. They found that these discrepancies are caused by cumulative effects of high-frequency variability, which cannot be accurately sampled by a monthly time resolution. Given that vigorous high-frequency variability also exists in the tropical IO (Schott et al., 2009), and its rectification substantially contributes to the seasonal cycle of the upper ocean temperature (Duncan & Han, 2012) and salinity (Köhler et al., 2018) there, as well as the interannual variability of the eastward surface jets that transport salty water from the Arabian Sea to the eastern IO (Han et al., 2004), it is desirable to revisit the validity of mechanisms responsible for the pIOD-related salinity anomalies through an online salinity budget analysis that allows exact closure of the salinity budget. The key questions of this chapter are as follows: To what extent the processes proposed by previous studies are appropriate? How large are the contributions from high-frequency variability?

In this chapter, we perform a series of sensitivity experiments and an online salinity budget analysis using outputs from a regional ocean model to address these questions. The remainder of this chapter is organized as follows. In section 2.2, we describe the observational datasets, the configurations of the ocean model used in this study, and the design of sensitivity experiments. A linear continuously stratified model (LCSM), which is used to further clarify the physical processes

at work, is also introduced. In section 2.3, we discuss the main features of the IOD-related salinity variability in the IO and validate the model against the observation. In section 2.4, we report the results from sensitivity experiments and a salinity budget analysis and explore the causes for salinity anomalies associated with the pIOD. Additional LCSM experiments are also carried out to substantiate the arguments derived from the diagnostic analysis described above. Finally, in section 2.5, we provide a summary and discussion.

2.2 Data and model

2.2.1 Observational datasets

We use 1° × 1° gridded temperature and salinity data (Roemmich & Gilson, 2009) to examine the thermohaline variation during IOD events. This gridded data is constructed based only on individual Argo profiles using an optimum interpolation method. Its vertical resolution is about 10 m in the upper 150 m, and we analyze monthly data from January 2004 to December 2014. From 2004 to 2007, the spatial coverage of Argo profiles was relatively sparse in the tropical IO, although it exceeded 80% of the planned level (1 float per 3° longitude ×3° latitude box) (Cai & Qiu, 2013). For this reason, we need to be careful when we compare results from this dataset with those from other datasets during the earlier period.

To complement the short data period of the Argo observation, we also use data from the Ocean Reanalysis System version 4 (ORAS4) provided by the European Centre for Medium-Range Weather Forecasts (ECMWF) (Balmaseda et al., 2013). This product has been widely used for studies in the tropical IO and validated against various in-situ observations (Chen et al., 2015; Chen, Han, Shu, et al., 2016; Nyadjro & McPhaden, 2014). The dynamical core model of the ORAS4 is the Nucleus for European Modeling of the Ocean (NEMO) and it is forced by daily atmospheric fluxes (solar radiation, total heat flux, evaporation-minus-precipitation, and wind stress) obtained from the ERA40 reanalysis (from September 1957 to December 1988) (Uppala et al., 2005), the ERA-interim reanalysis (from January 1989 to December 2009) (Dee et al., 2011), and the ECMWF operational archive (after January 2010). The ORAS4 assimilates temperature, salinity and satellite derived sea surface height (SSH) anomalies using variational assimilation system called NEMOVAR. This product has a 1° × 1° horizontal resolution and 42 vertical levels with 18 of them in the upper 200 m. Monthly SSH, temperature, salinity, and velocity data from 1958 to 2014 are used for the present analysis. Since vertical velocity is not available, we estimate it by integrating horizontal divergence

downward from the surface, with the surface value set to the time derivative of SSH.

We note that qualitatively the same results are obtained even if we use the Grid Point Value of the Monthly Objective Analysis (MOAA-GPV) (Hosoda et al., 2008) for the Argo data and the Simple Ocean Data Assimilation (SODA) version 2.2.4 datasets (Carton & Giese, 2008) and the Ocean Reanalysis System version 3 (ORAS3) (Balmaseda et al., 2008) as the ocean reanalysis products. Since we focus on phenomena with interannual timescale in this study, we apply 3-month running mean to anomaly fields (original value minus seasonal mean) in order to filter out subseasonal signals.

2.2.2 ROMS description

The model used in this study is the Regional Ocean Modeling System (ROMS) (Shchepetkin & McWilliams, 2005), which solves the primitive equations on a horizontal curvilinear and terrain-following vertical coordinate under the hydrostatic and Boussinesq approximations. The ROMS has been extensively used for studying ocean circulations including the recent studies on the IO (C. Lee et al., 2018; J. Li et al., 2016). The model is configured for the tropical IO (30°-110°E, 46°S-32°N) with a horizontal resolution of 1/3°×1/3°. The bathymetry of the model is adopted from ETOPO2 data with 1.5°×1.5° spatial smoothing. The model has 40 vertical sigma layers, and vertical coordinate stretching parameters are set to theta_s=10.0, theta_b=0.4, and Tcline=200.0. With this parameter choice, there are 25 vertical levels in the upper 200 [m] when the depth is 4000 [m]. Along the eastern and southern boundaries, the mixed radiation-nudging boundary condition (Marchesiello et al., 2001) is used, and temperature, salinity, and horizontal velocity are relaxed to the monthly value from the ORAS4 with the nudging time scale of 360 days (3 days) for the outflow (inflow) case. The northern and western boundaries are closed, and a non-slip condition is imposed along the continental boundary. A similar approach has been used in the past modeling studies on the tropical

IO (C. Lee et al., 2018). For calculation of vertical viscosity and diffusion coefficients, we use the turbulent closure scheme of Furuichi et al., (2012), which is a modified version of the Mellor-Yamada schemes. Penetration of shortwave radiation is computed assuming Jerlov water type I (Paulson & Simpson, 1977) over the entire domain.

The surface forcing fields are 3-hourly shortwave/longwave radiation, 10 m wind, surface temperature/humidity, and precipitation of the JRA55-do (Tsujino et al., 2018). To isolate themodynamical and dynamical roles of wind forcing, wind stress and wind speed are separately given to the model in the present configuration. More specifically, surface wind speed (V_{10}), and zonal and meridional wind stress (τ^x, τ^y) are calculated based on the 10 m zonal and meridional wind (u_{10}, v_{10}) using the standard bulk formula as follows:

$$V_{10} = \sqrt{u_{10}^2 + v_{10}^2} \tag{2.1}$$

$$(\tau^x, \tau^y) = \rho_a c_d V_{10}(u_{10}, v_{10}), \tag{2.2}$$

where $\rho_a = 1.175$ kg m^{-3} is the density of air and $c_d = 0.0015$ is the drag coefficient following Y. Li et al. (2013). The sensible heat, latent heat, and evaporation are calculated using the Coupled Ocean-Atmosphere Response Experiment (COARE) 3.0 algorithm (Fairall et al., 2003) based on sea level pressure, 10 m temperature/humidity, wind speed and model's SST. In addition, daily river runoff data from the JRA55-do (Suzuki et al., 2018; Tsujino et al., 2018) is used to realistically reproduce the salinity pattern in the IO. In our model, freshwater from rivers are used as the lateral boundary condition of momentum and tracers, and it is assumed that they are uniformly distributed in the vertical direction. The salinity of freshwater is set to 0 [psu], whereas the temperature is assumed to be equal to the value of the grid point adjacent to river mouths.

2.2.3 Sensitivity experiments using the ROMS

The model is spun up for 30-yr from the initial condition derived from the World Ocean Atlas 2013 (WOA13) using 3-hourly atmospheric, daily river, and monthly boundary climatological forcing. Then, the hindcast run is conducted from 1958 to 2015 using interannually varying forcing. We will refer to this run as the main run (MR), and all outputs have been archived as 3-day averaged data.

To quantify the relative importance of IOD-related atmospheric anomalies on salinity anomalies, we have conducted a series of sensitivity experiments. For this purpose, we have processed "Non-IOD forcing" from the original forcing for all the pIOD years (9 years; see section 2.3.1 for the specific years and a detailed description of their selection criteria). For atmospheric forcing (with 3-hourly temporal resolution; $A_{original}$), we have first converted them to daily data and computed anomalies by subtracting the long-term climatology. Then, a 120-day Lanczos low-pass filter (Duchon, 1979) is applied to daily anomalies of the whole period to extract low-frequency variation. Note that these low-passed anomalies during pIOD years contain both influences from the El Niño and the pIOD, due to the frequent co-occurrence of these two climate modes (e.g. Yamagata et al., 2004). As our purpose here is to isolate the collective impacts of the IOD-related anomalies on salinity, we do not explicitly distinguish the influences from the IOD and those from other interannual climate modes (e.g. ENSO), and simply refer these low-passed anomalies as A_{IOD} (more detailed discussions on the relative importance of the ENSO and IOD are presented in Section 2.3.1).

These "IOD-related" signals are linearly interpolated into 3-hourly data and then we subtracted them from the original data with a weighting function to obtain "Non-IOD forcing" as follows:

$$A_{NoIOD} = A_{original} - w(t) \cdot A_{IOD} \tag{2.3}$$

$$w(t) = \begin{cases} 0 & (t < t_{Mar}) \\ \dfrac{t - t_{Mar}}{t_{May} - t_{Mar}} & (t_{Mar} \le t \le t_{May}) \\ 1 & (t > t_{May}). \end{cases} \tag{2.4}$$

Here, t_{Mar} (t_{May}) denotes the number of days from January 1st to March 1st (May 1st). Note that a time-dependent tapering function $w(t)$ is introduced to take the seasonality of the IOD (it starts around late boreal spring and peaks in boreal fall) into account. Though there may be some arbitrariness in the functional form of $w(t)$, here we have decided to choose Eq. (2.4) based on careful inspection of the seasonally-stratified composited atmospheric anomalies associated with the IOD. A similar approach is also used for the processing of the "Non-IOD" boundary forcing.

Using these "Non-IOD" forcing described above, we have performed six parallel experiments in addition to the MR (see Table 2.1). In the NoIOD run, the model is started from the initial conditions from the MR for each pIOD year, and is forced by the "Non-IOD" atmospheric and boundary forcing from January 1st to December 31st. The difference between MR and NoIOD run (i.e. MR-NoIOD) isolates the total impacts of pIOD-related atmospheric and boundary forcing. In the NoPRCP run, we rerun the model using the same forcing as the MR, but replace precipitation with the "Non-IOD" forcing. The difference, MR-NoPRCP, measures the precipitation effects on salinity anomalies. The NoSWR run is similar, except that the "Non-IOD" shortwave radiation is used. In the NoWIND run, the model is forced by the "Non-IOD" wind stress and speed (again, other atmospheric and boundary forcing is same as the MR), while only wind stress is replaced with the "Non-IOD" forcing in the NoSTRESS run. The difference, MR-NoSTRESS measures the wind stress effect, which alters salinity by changing advection and mixing, and NoSTRESS-NoWIND extracts the wind-speed effect, which affects salinity through surface evaporation. Finally, in the

NoBDRY experiment, we force the model using the original atmospheric forcing and the "Non-IOD" lateral boundary forcing. This experiment is designed to isolate the impacts of remote forcing on salinity anomalies in the tropical IO (MR-NoBDRY measures such effects). These experiments are conducted for all 9 pIOD years, and results presented below are shown as the ensemble average (i.e. composite) of these events to highlight signals common to pIOD events. We have assessed the statistical significance of the anomalies based on Student's two-tailed t test with 8 degrees of freedom.

Table 1: Summary of ROMS sensitivity experiments

Experiments	Atmospheric & boundary forcing	Description
MR	3 hourly forcing	
NoIOD	No IOD forcing	Remove contribution from IOD-related anomalies in atmospheric and boundary forcing
NoPRCP	Low-passed precipitation	Remove contribution from IOD-related precipitation anomalies
NoSWR	Low-passed shortwave radiation	Remove contribution from IOD-related shortwave radiation anomalies
NoWIND	Low-passed wind stress/speed	Remove contribution from IOD-related wind stress/speed anomalies
NoSTRESS	Low-passed wind stress	Remove contribution from IOD-related wind stress anomalies
NoBDRY	Low-passed boundary forcing	Remove IOD-related boundary effects

2.2.4 Linear continuously stratified model (LCSM)

To help understanding the dynamics behind the changes associated with salinity stratification, we also used a LCSM (McCreary, 1980, 1981). In the LCSM, the equations of motion, continuity equation, and density tendency equation are linearized around a background state of rest

and a specified stratification with flat ocean bottom (with depth of H). The governing equations are

$$\frac{\partial u}{\partial t} = -\frac{1}{\rho_0}\frac{\partial p}{\partial x} + fv + \nu_h \nabla^2 u + \frac{\partial}{\partial z}(\nu_v \frac{\partial u}{\partial z}), \tag{2.5a}$$

$$\frac{\partial v}{\partial t} = -\frac{1}{\rho_0}\frac{\partial p}{\partial y} - fu + \nu_h \nabla^2 v + \frac{\partial}{\partial z}(\nu_v \frac{\partial v}{\partial z}), \tag{2.5b}$$

$$\frac{\partial p}{\partial z} = -\rho g, \tag{2.5c}$$

$$\frac{\partial \rho}{\partial t} = \frac{N^2}{g} w + \frac{\partial^2}{\partial z^2}(\kappa_v \rho), \tag{2.5d}$$

$$\frac{\partial u}{\partial x} + \frac{\partial v}{\partial y} + \frac{\partial w}{\partial z} = 0, \tag{2.5e}$$

where (u, v, w) denotes the zonal, meridional, and vertical velocity, respectively, p is the pressure, ρ is the density, f is the Coriolis parameter, g $(= 9.8\ [m/s^2])$ is the gravitational acceleration, ρ_0 $(= 1024\ [\mathrm{kg/m^3}])$ is the reference density, $N^2 = -\frac{g}{\rho_0}\frac{\partial \bar{\rho}}{\partial z}$ is the squared buoyancy frequency with the background density $\bar{\rho}(x, y, z)$, ν_h, ν_v are the horizontal and vertical viscosity coefficients, respectively, and κ_v is the vertical diffusion coefficient. Note that the influence of salinity is implicitly incorporated in Eq. (2.5d) via its effects on the density. These equations are subject to the following boundary conditions at the sea surface and bottom:

$$\upsilon_v \frac{\partial u}{\partial z}(z = 0) = \frac{\tau^x}{\rho_0}, \tag{2.6a}$$

$$\upsilon_v \frac{\partial v}{\partial z}(z = 0) = \frac{\tau^y}{\rho_0}, \tag{2.6b}$$

$$\rho(z = 0) = w(z = 0) = 0, \tag{2.6c, d}$$

$$\upsilon_v \frac{\partial u}{\partial z}(z = -H) = \upsilon_v \frac{\partial v}{\partial z}(z = -H) = 0, \tag{2.6e, f}$$

$$\rho(z = -H) = w(z = -H) = 0. \tag{2.6g, h}$$

Here, τ^x and τ^y represent the zonal and meridional components of the surface wind stress, respectively. The modal functions at each grid point can be obtained by solving the following

eigenvalue problem,

$$\frac{d}{dz}\left(\frac{1}{N^2}\frac{d\psi_n}{dz}\right) = -\frac{1}{c_n^2}\psi_n, \tag{2.7}$$

with the boundary conditions

$$\frac{d\psi_n}{dz} = 0 \; at \; z = 0 \; and \; z = -H. \tag{2.8}$$

Here, $c_n(x, y)$ and $\psi_n(x, y, z)$ are the phase speed and vertical modal function of the $n-$th vertical baroclinic mode, respectively. Due to orthogonality of the vertical modal functions, each variable can be represented as

$$u = \sum_{n=1}^{N} u_n\psi_n \, , v = \sum_{n=1}^{N} v_n\psi_n \, , p = \sum_{n=1}^{N} p_n\psi_n, \tag{2.9}$$

$$w = \sum_{n=1}^{N} w_n \int_{-H}^{z} \psi_n \, , \rho = \sum_{n=1}^{N} \rho_n \frac{d\psi_n}{dz}.$$

To obtain governing equations of the modal coefficients, we assume that the values of vertical viscosity and diffusion coefficients are equal and inversely proportional to the squared buoyancy frequency,

$$\nu_v = \kappa_v = \frac{A}{N^2}, \tag{2.10}$$

with $A = 1.3\times10^{-8}$[m^2/s]. By substituting Eq. (2.9) to the governing equations (2.5a-2.5e) and using Eqs. (2.6), (2.7), (2.8) and (2.10), we obtain equations for expansion coefficients (see McCreary (1980) for details):

$$\left(\frac{\partial}{\partial t} + \frac{A}{c_n^2}\right)u_n = -\frac{1}{\rho_0}\frac{\partial p_n}{\partial x} + fv_n + \nu_h\nabla^2 u_n + b_n\tau_n^x, \tag{2.11a}$$

$$\left(\frac{\partial}{\partial t} + \frac{A}{c_n^2}\right)v_n = -\frac{1}{\rho_0}\frac{\partial p_n}{\partial y} - fu_n + \nu_h\nabla^2 v_n + b_n\tau_n^y, \tag{2.11b}$$

$$\left(\frac{\partial}{\partial t} + \frac{A}{c_n^2}\right)p_n = -c_n^2\left(\frac{\partial u_n}{\partial x} + \frac{\partial v_n}{\partial y}\right), \tag{2.11c}$$

$$w_n = \left(\frac{\partial}{\partial t} + \frac{A}{c_n^2}\right)\frac{p_n}{c_n^2}. \tag{2.11d}$$

The wind projection coefficients, b_n, can be written as

$$b_n = \frac{1}{\int_{-H}^{0} \psi_n^2 dz}. \tag{2.12}$$

These equations are essentially the same with the original version of the LCSM used by McCreary (1980,1981), except that ψ_n are calculated at each grid point using spatially varying stratification. The phase speeds c_n, on the other hand, are computed from horizontally averaged background stratification. These approaches are identical to those by Keenlyside and Kleeman (2002).

The horizontal resolution and land-sea mask of the LCSM are exactly the same with those of the ROMS. The ocean bottom is assumed to be flat with a depth of 4000 [m], and gravest 30 vertical baroclinic modes are used for calculation (i.e. $H = 4000$ [m] and $N = 30$). The results presented below are not sensitive to slight changes in these parameters. The inputs necessary to drive the model are wind stress forcing and (spatially varying) background stratification, and detailed specification of these inputs in the sensitivity experiments will be described in the corresponding sections (section 2.4.3 and 3.5.3).

2.3. Features of observed and modeled IOD-related variability

2.3.1 Features of observed salinity variation

First, we take a look at pIOD-related salinity anomalies captured by the Argo observation. As an example of a typical pIOD event, we select the 2006 event, which is the strongest pIOD year during the Argo observation period. As documented by previous studies (Grunseich et al., 2011; Y. Zhang et al., 2013), there are prominent negative SSS anomalies in the central-eastern equatorial IO (Fig. 2.1, left two columns). These anomalies develop during boreal fall and reach their peak toward the end of the year, followed by gradual decay in January-March of the next year. Through salinity budget analysis, previous studies have shown that a decrease in the transport of high salinity water from the western IO associated with weakening of the climatological eastward current in boreal fall (so called the Wyrtki Jet; Wyrtki, 1973) is the main factor for the generation of these negative SSS anomalies (J. Li et al., 2016; Y. Zhang et al., 2013). In addition, weak positive SSS anomalies extend over the SEIO. Similar features can be found in the ORAS4 (Fig. 2.1, the second column), but the amplitude of these SSS anomalies is larger than that of the Argo data. This may be due to deficiency in the ocean model used to construct the reanalysis product, or insufficient number of Agro floats in the key regions.

On the other hand, the spatial pattern of salinity anomalies near the pycnocline (we have chosen the range of vertical averaging from 50 to 100 [m] depth as an example) is somewhat different from that of SSS (Fig. 2.1, right two columns). Despite the salient surface freshening, there are remarkable positive salinity anomalies in the EEIO. They appear and develop during boreal summer to fall and decay suddenly after the demise of the IOD. Their persistence seems to be slightly shorter than that of the surface signals. Other notable features are negative salinity anomalies in the eastern off-equatorial IO (Fig. 2.1). To some extent, they seem to be related to the surface signals, but their spatial structure (a pair of negative anomalies straddling the equator) is markedly

different. Again, qualitatively similar anomalies are seen in the ORAS4, though their amplitude is slightly larger than that of the Argo data (Fig. 2.1, the fourth column). These results imply that processes contributing to the development of these subsurface salinity anomalies are greatly different from those of SSS.

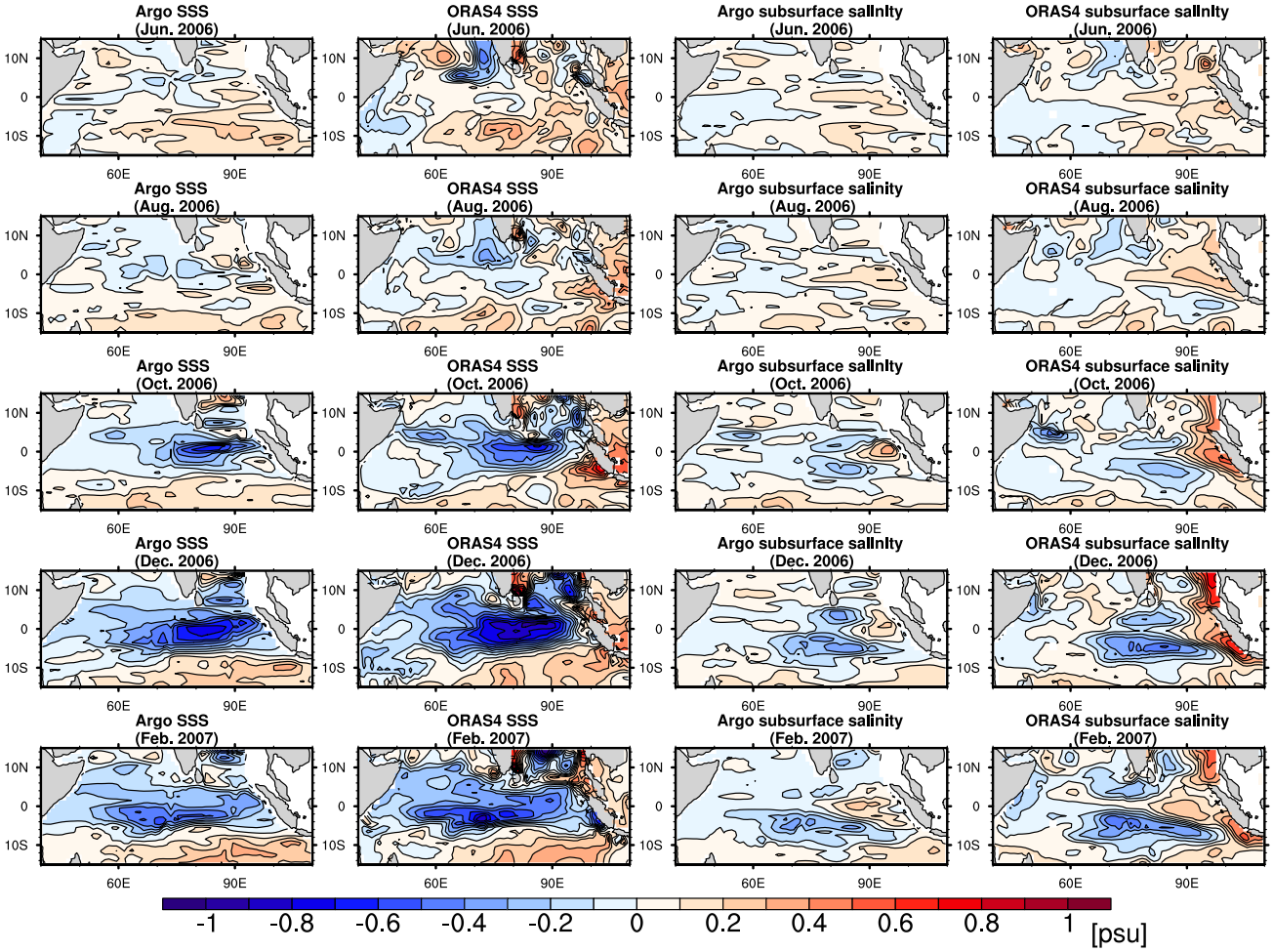

Figure 2.1: Time evolution of surface (the first and second columns) and subsurface (the third and fourth columns: vertically averaged over 50 [m]-100 [m] depth) salinity anomalies in the tropical Indian Ocean from June 2006 to February 2007 (in psu). The results from Argo data are shown in the first and third columns, while those from the ORAS4 are presented in the second and fourth columns. The contour intervals are 0.1 [psu].

To see whether these anomalies are common features of all pIOD years, we construct composites of salinity anomalies using the ORAS4, which can realistically reproduce the observed pattern seen in the 2006 pIOD case. For this purpose, we calculate the Dipole Mode Index (DMI), which is defined as the difference between area-averaged SST anomalies over the western box (10°S–10°N, 50°–70°E) and the eastern box (10°S–0°, 90°–110°E) (Saji et al., 1999). Then, we define the pIOD year as the year when the DMI in September-November (SON) all exceeds 1.0 standard deviation. This definition excludes so-called unseasonable IOD (Du et al., 2013) and aborted IOD (S. A. Rao & Yamagata, 2004) so that only canonical pIOD events are selected. According to this criterion, 9 years (1961, 1963, 1972, 1977, 1982, 1987, 1994, 1997, and 2006) are identified as the pIOD years.

Figure 2.2 displays composites of salinity anomalies constructed from all pIOD years. We can see that SSS anomalies are similar to the observed pattern, although their amplitude is slightly different from the Argo observation. In addition, subsurface salinity anomalies are in good agreement with the Argo observation. These results suggest that surface and subsurface salinity anomalies captured by the Argo observation in 2006 are robust features of the pIOD. Furthermore, an empirical orthogonal function (EOF) analysis is applied to the SON-averaged surface and subsurface salinity anomalies of the tropical IO (40°-105°E, 15°S-15°N) to check whether the IOD is the dominant factor responsible for the observed upper-ocean salinity variations. Here, we have concatenated surface and subsurface salinity anomalies for the spatial direction to construct the data matrix (see also section 3.2.2). The first EOF mode explains 30.4% of the total variance, and well separated from the second mode (which accounts for 8.6% of the total variance). The spatial pattern of salinity anomalies of the EOF is very similar to those derived from the composite analysis based on the DMI (Fig. 2.3), and the first principal component is highly correlated with the SON-averaged

DMI (with a correlation coefficient of 0.91). These results demonstrate that salinity variations in the tropical IO during the boreal winter are mainly dominated by the IOD.

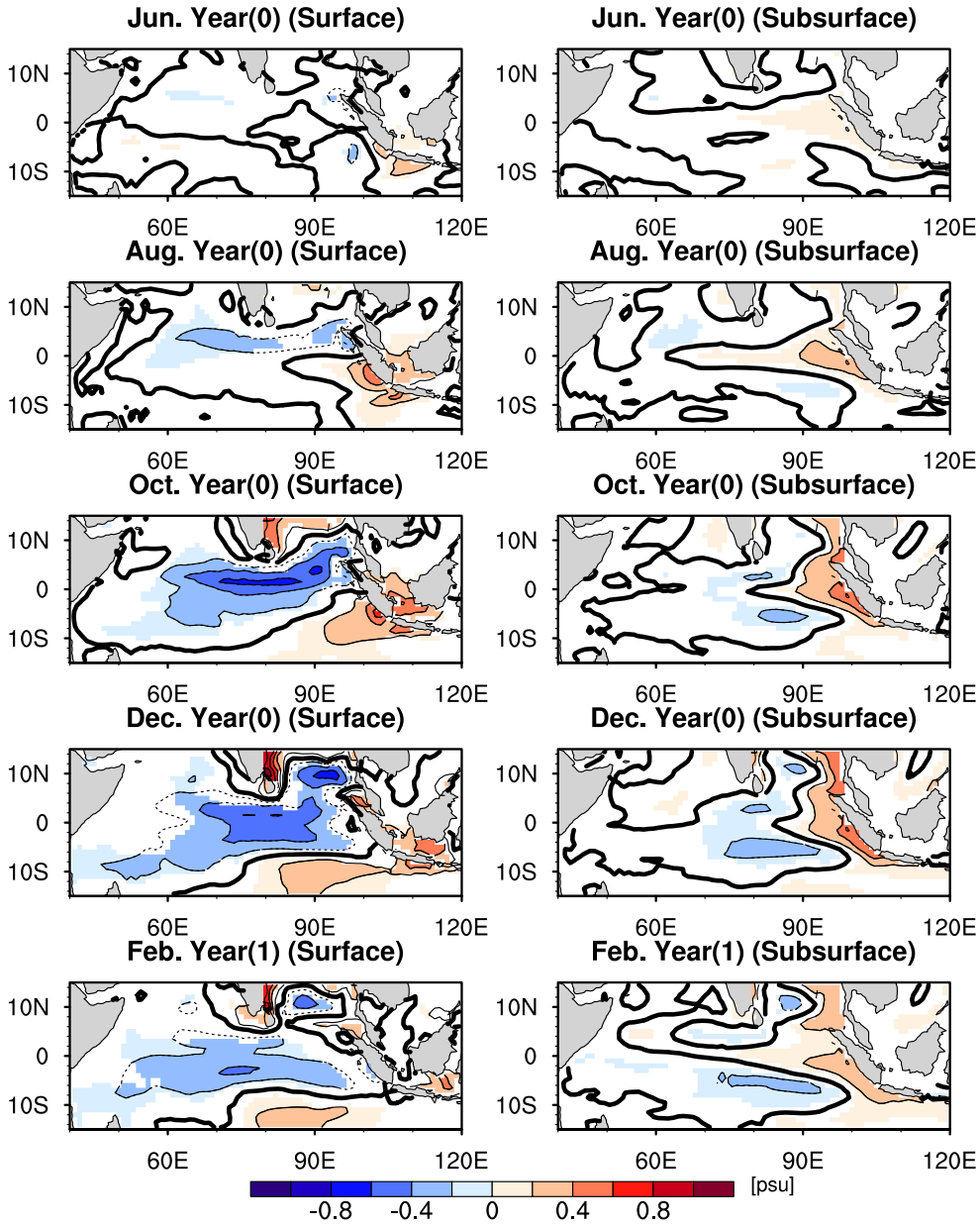

Figure 2.2: Composite of surface (left) and subsurface (right: vertically averaged over 50 [m]-100 [m] depth) salinity anomalies in the tropical Indian Ocean during the positive Indian Ocean Dipole (pIOD) events (constructed from ORAS4) (in [psu]). Year 0 denotes the year when the pIOD develops and Year 1 means the following year. The contour intervals are 0.2 psu. Anomalies significant at the 90% confidence level by a two-tailed t-test are shaded.

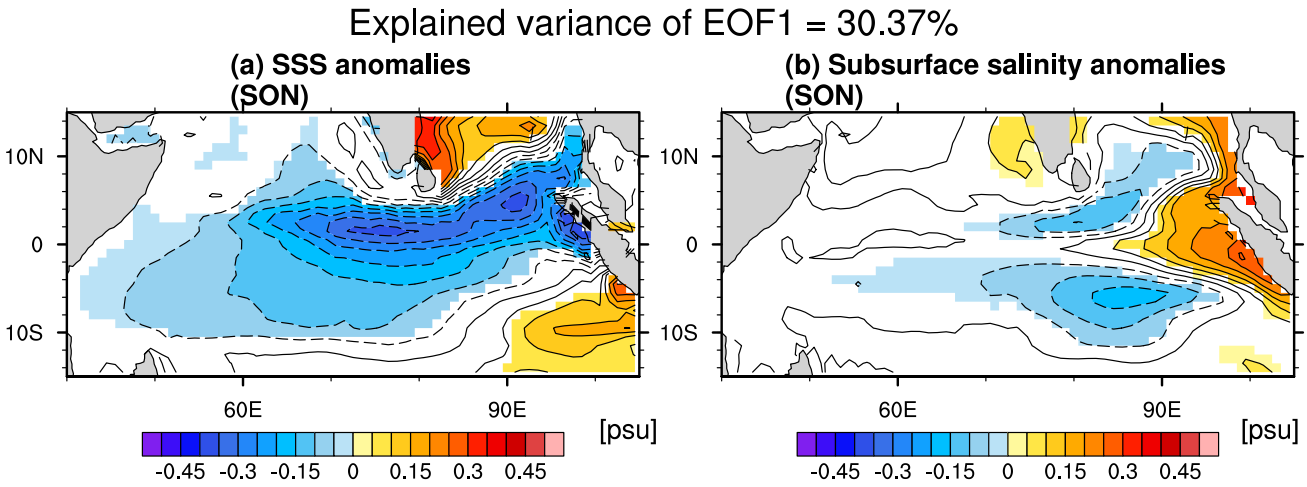

Figure 2.3: Regression coefficients of the September-November (SON) averaged (a) surface and (b) subsurface (vertically averaged from 50 [m] to 100 [m] depth) against the normalized principal component of the first empirical orthogonal function (EOF) mode (in [psu]). The contour are 0.05 [psu], and regression coefficients significant at the 90% confidence level by a two-tailed t-test are shaded. The percentage of variance explained by the first EOF mode is shown in the top.

Since El Niño and pIOD events sometimes co-occur (Yamagata et al., 2004), one may wonder which climate mode is more important for the generation of these salinity anomalies. To answer this question, we adopt partial regression techniques that can isolate these two signals (Currie et al., 2013; Keerthi et al., 2013). We use the Niño 3.4 index (SST anomalies averaged over 120°W–170°W, 5°S–5°N) and the DMI as a representative of the ENSO and the IOD, respectively. To isolate the IOD-induced signals, the ENSO-related signals are first removed from the SON-averaged DMI (DMI^{SON}) and the targeted variable A by calculating their linear regression against the DJF-averaged Niño 3.4 index ($Niño3.4^{DJF}$) as follows:

$$DMI^{SON}_{noENSO} = DMI^{SON} - Reg(DMI^{SON}, Niño3.4^{DJF}) \times Niño3.4^{DJF}$$

$$A_{noENSO} = A - Reg(A, Niño3.4^{DJF}) \times Niño3.4^{DJF}$$

Here, SON and DJF refer to September-November and December-February, respectively. Then, we compute the regression coefficients between A_{noENSO} and DMI^{SON}_{noENSO} ($Reg(A_{noENSO}, DMI^{SON}_{noENSO})$) and use them as measures of the IOD-induced signals. The ENSO-induced signals can be calculated in a similar manner. We note that the following results are not sensitive to a slight shift in the representative season of each index. Also, qualitatively similar results are obtained even if we use the Niño 3 (SST anomalies averaged over 150°W–90°W, 5°S–5°N) or Niño 4 (SST anomalies averaged over 160°E–150°W, 5°S–5°N) index instead of the Niño 3.4 index.

The spatial pattern of partial regression coefficients of surface and subsurface salinity anomalies against the DMI and the Niño 3.4 index are presented in Fig. 2.4. During boreal summer and fall, the IOD-related signals have large amplitudes and exhibit patterns similar to composites for both depth ranges (Fig. 2.2). On the other hand, the magnitude of ENSO-related signals are generally smaller than that of the IOD-related signals, though weak signals can be found in the eastern tropical IO in boreal winter (the third and fourth columns). Therefore, we may conclude that the IOD is the main driver of salinity anomalies in boreal fall. Although previous studies showed the dominant influence of the IOD over the ENSO on thermocline (S. A. Rao & Behera, 2005; W. Yu et al., 2005) and SSS (Y. Zhang et al., 2013) variability in the tropical IO north of 10°S, this study is the first to show such dominance in subsurface salinity variability.

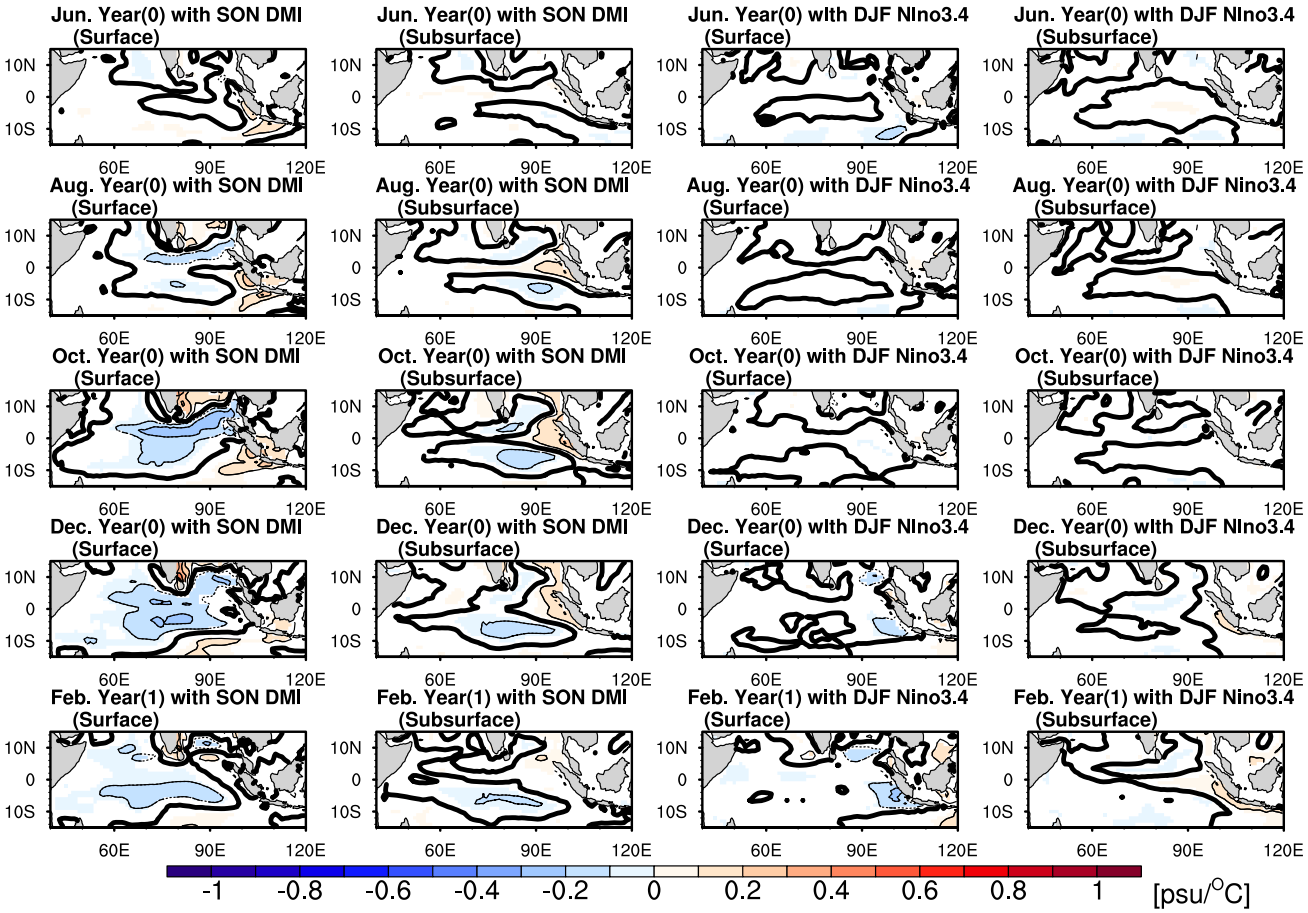

Figure 2.4: (First and second columns) Partial regression coefficients of surface and subsurface (vertically averaged over 50 [m]-100 [m] depth) salinity anomalies against the December-February (DJF) Niño 3.4 index, having removed the influence of the September-November (SON) Dipole Mode Index (DMI) (in [psu $°C^{-1}$]). (Third and fourth columns) As in the first and second columns, but for partial regression coefficients against the SON DMI, having removed the influence of the DJF Niño 3.4 index (in [psu $°C^{-1}$]). The contour intervals are 0.1 [psu $°C^{-1}$]. Regression coefficients significant at the 90% confidence level by a two-tailed t-test are shaded.

2.3.2 Comparison of modeled and observed salinity variation

Before investigating the detailed mechanisms of the IOD-related salinity variability, we need to check the validity of the model. For this purpose, we first compare the salinity field from the

ROMS and ORAS4. Figure 2.5 displays their mean SSS (averaged over the upper 30 m) and subsurface salinity (near the halocline: averaged over 50-100 m) pattern. We note that qualitative results described below are not so sensitive to slight changes in the depth range of vertical averaging (e.g. averaging over 0-20 [m] and 80-120 [m] gives similar results for SSS and subsurface salinity, respectively). From the SSS distribution in the ORAS4 (Fig. 2.5b), we can identify a striking spatial contrast over the IO. More specifically, regions with low SSS in the Bay of Bengal and the equatorial region are flanked by high SSS region in the Arabian Sea and subtropical southern IO. These features are also detected by other in-situ and satellite SSS data, and linked to regional differences in freshwater flux (precipitation, evaporation, and river runoff) and ocean dynamical processes (Han & McCreary, 2001; R. R. Rao & Sivakumar, 2003). A similar pattern with a weaker contrast is also observed for subsurface salinity (Fig. 2.5d). The ROMS reasonably reproduces these features (Figs. 2.5a, c), despite no SSS relaxation is applied in the model. However, significant biases do exist in the model. Compared to the ORAS4, salinity in the model is generally too high, especially in the Bay of Bengal, Arabian Sea, and southern IO, and biases are more prominent in SSS than subsurface salinity. These discrepancies may stem from inaccuracy of atmospheric/river runoff forcing, shortcomings of the parameterization adopted in the model (e.g. the vertical mixing scheme), insufficient horizontal/vertical resolution of the model, and/or assimilation technique for construction of ocean reanalysis data. These mean state biases may potentially affect the amplitude and structure of interannual anomalies.

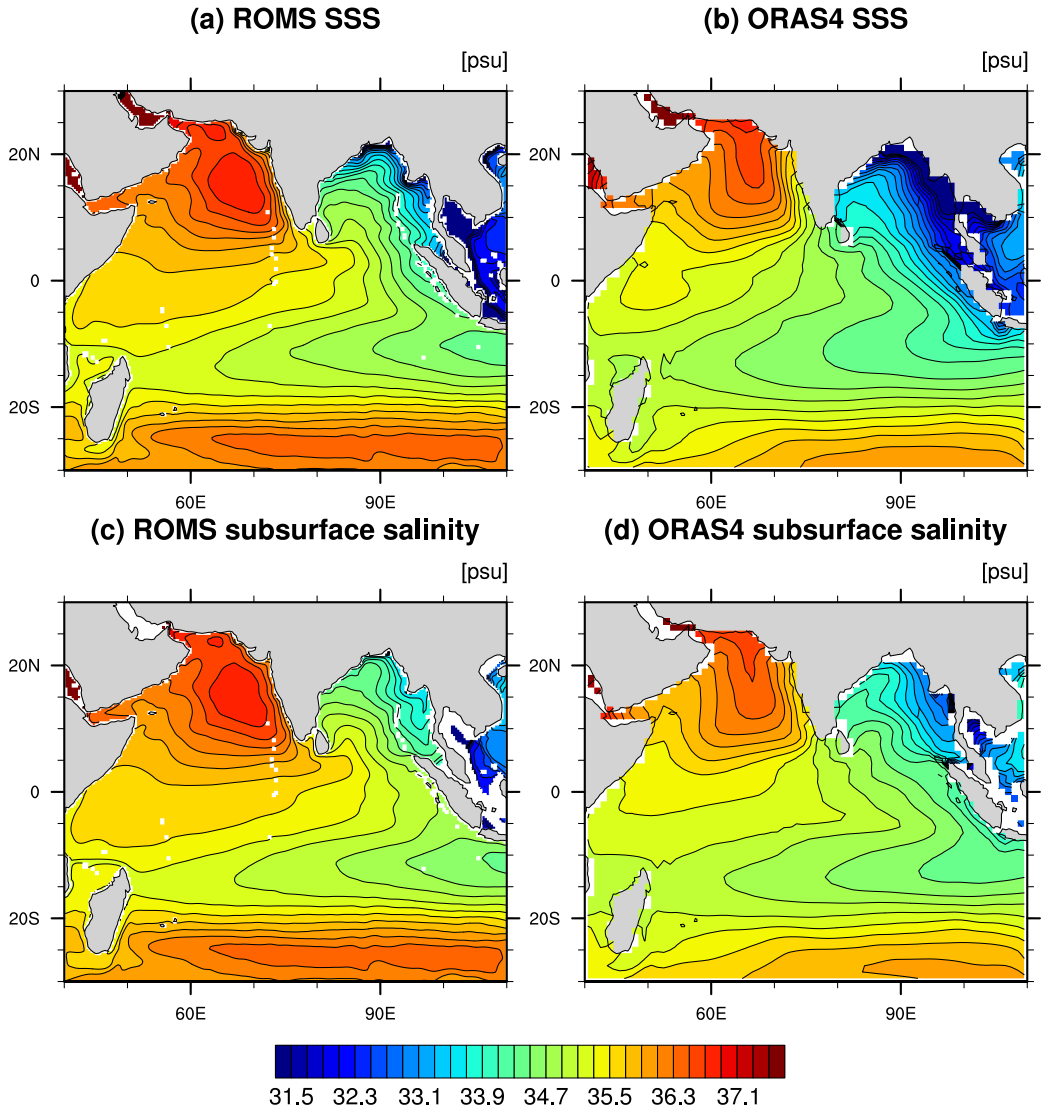

Figure 2.5: (a) Spatial pattern of mean sea surface salinity (SSS) (vertically averaged over the upper 30 [m]) from the ROMS MR (in [psu]). (b) As in (a), but from the ORAS4. (c) As in (a), but for subsurface salinity (vertically averaged between 50 [m] and 100 [m] depth). (d) As in (c), but for the ORAS4. The contour intervals are 0.2 [psu].

Next, we check the modeled and observed DMI. Figure 2.6a shows the time series of the normalized DMI from the ROMS MR and ORAS4. Though the model tends to overestimate the amplitude of the DMI, major pIOD and negative IOD events are well captured. Also, the DMI has

maximum amplitude during boreal fall (Fig. 2.6b) for both ROMS and ORAS4, suggesting that the model faithfully reproduces the seasonality of the IOD. Therefore, we use the same 9 pIOD years those obtained from the ORAS4 in the following composite analyses.

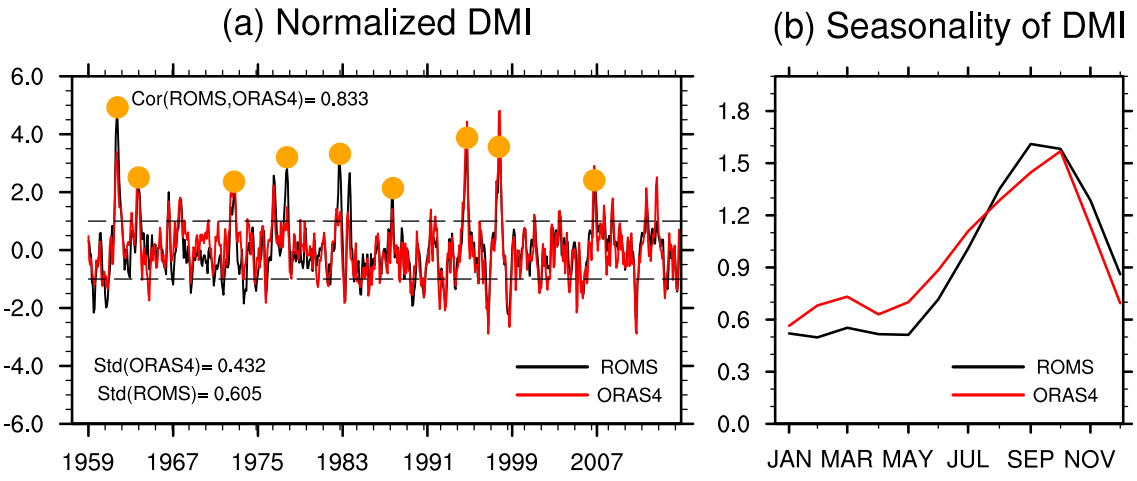

Figure 2.6: (a) Time series of the normalized DMI for the ROMS MR (black) and ORAS4 (red). The standard deviation of the DMI is shown in the lower left, whereas the correlation coefficient between ROMS and ORAS4 is shown in the upper left. The dashed black lines represent ±1 standard deviation, and orange markers indicate pIOD years. (b) Standard deviation of the normalized DMI as a function of calendar month.

Figure 2.7 compares surface and subsurface temperature anomalies during the mature phase of pIOD events. The zonal dipole structure of SST anomalies with anomalous cooling (warming) in the eastern (western) IO is evident in both ROMS and ORAS4 (Figs. 2.7a, b). However, negative anomalies in the east are overestimated and extend too far to the west in the model. For subsurface temperature (vertically averaged from 50 to 100 [m] depth), regions with anomalous significant warming are seen along off-equatorial bands of the western tropical IO, whereas prominent cooling is evident off the Sumatra-Java coast (Fig. 2.7d), consistent with previous studies

(S. A. Rao et al., 2002; Shinoda et al., 2004). The model nicely captures these structures (Fig. 2.7c), though the amplitude of subsurface signals is weaker than that of the ORAS4. The coincidence of stronger anomalies near the surface and weaker anomalies near the thermocline may be partly due to inadequate representation of vertical mixing processes.

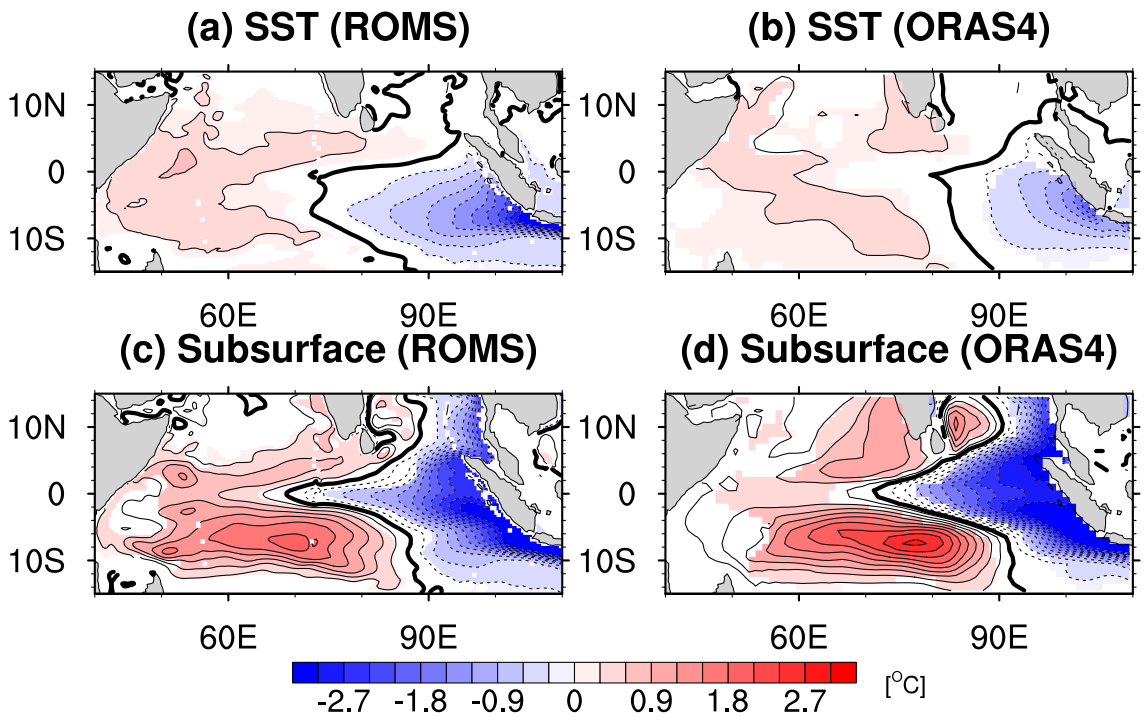

Figure 2.7: Composite of sea surface temperature (SST) (top) and subsurface (bottom: averaged over 50 [m]-100 [m] depth) temperature anomalies during September-November (SON) of positive Indian Ocean Dipole (pIOD) years (in [°C]) from the ROMS MR (left) and ORAS4 (right). The contour intervals are 0.3 [°C], and anomalies significant at the 90% confidence level by a two-tailed t test are shaded.

Since the main focus of this study is salinity anomalies associated with the pIOD, their proper representation in the model is prerequisite for further investigation. To confirm this, the ROMS simulated and the ORAS4 reanalyzed surface and subsurface salinity anomalies during pIOD

events are presented in Fig. 2.8. For SSS in the ORAS4 (Fig. 2.8b), strong freshening in the central-eastern equatorial IO and saltening in the SEIO are detected, as already documented by many previous literatures (J. Li et al., 2016; Y. Zhang et al., 2013). On the other hand, significant saltening (freshening) are seen in the EEIO (SEIO) for subsurface anomalies (Fig. 2.8d). These features are consistent with analysis of observational datasets presented in the previous section. Similar to temperature anomalies, the modeled salinity anomalies (Figs. 2.8a, c) agree well with the ORAS4, despite some minor discrepancies in their spatial pattern and magnitude. In fact, the pattern correlation of salinity anomalies between the ROMS and ORAS4 is 0.82 and 0.79 for surface and subsurface anomalies, respectively, and these are statistically significant at the 90% confidence level, based on a bootstrap method.

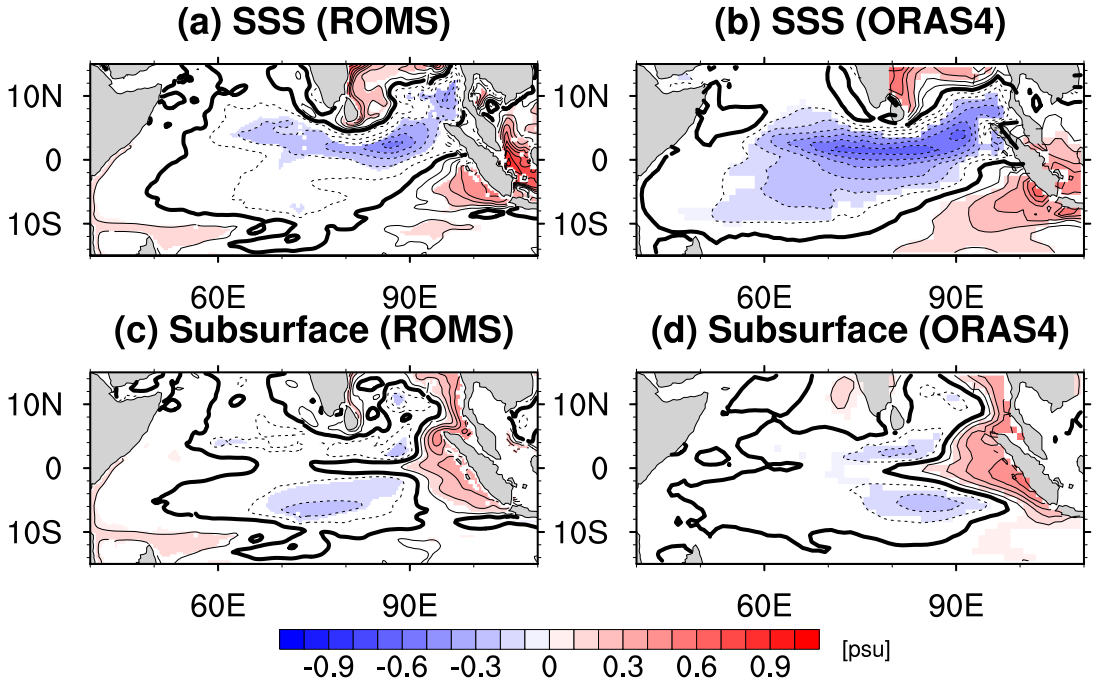

Figure 2.8: Composite of surface (top: a and b) and subsurface (bottom: c and d: averaged over 50 [m]-100 [m] depth) salinity anomalies during SON of pIOD years (in [psu]) from the ROMS MR (left) and ORAS4 (right). The contour intervals are 0.1 [psu]. Anomalies significant at the 90% confidence level by a two-tailed t test are shaded.

As changes in ocean circulation (e.g. strengthening/weakening of upwelling) play a crucial role in the generation of salinity anomalies, it is also instructive to compare modeled and reanalyzed current anomalies. Figure 2.9 shows composites of velocity anomalies during pIOD events in a depth-longitude section along the equator. During pIOD events, easterly wind anomalies decelerate the climatological eastward surface jet (i.e. Wyrtki Jet) and lead to westward current anomalies near the equator (Fig. 2.9b) (Nagura & McPhaden, 2010; Nyadjro & McPhaden, 2014). On the other hand, changes in zonal pressure gradient near the pycnocline lead to unusual acceleration of the Equatorial Undercurrent (EUC) (Fig. 2.9b) (Chen et al., 2015; Swapna & Krishnan, 2008) and strengthening (weakening) of upwelling in the eastern (western) equatorial IO (Fig. 2.9f) (Chen, Han, Li, et al., 2016). Southward (northward) current anomalies near the surface (pycnocline), which are likely driven by anomalous wind stress curl and associated Ekman drift (Miyama et al., 2003), are also detected in the ORAS4 product (Fig. 2.9d). The qualitative features of the current anomalies seen in the ORAS4 are reasonably captured by the ROMS (Figs. 2.9a, c, e), though the model tends to overestimate their amplitude.

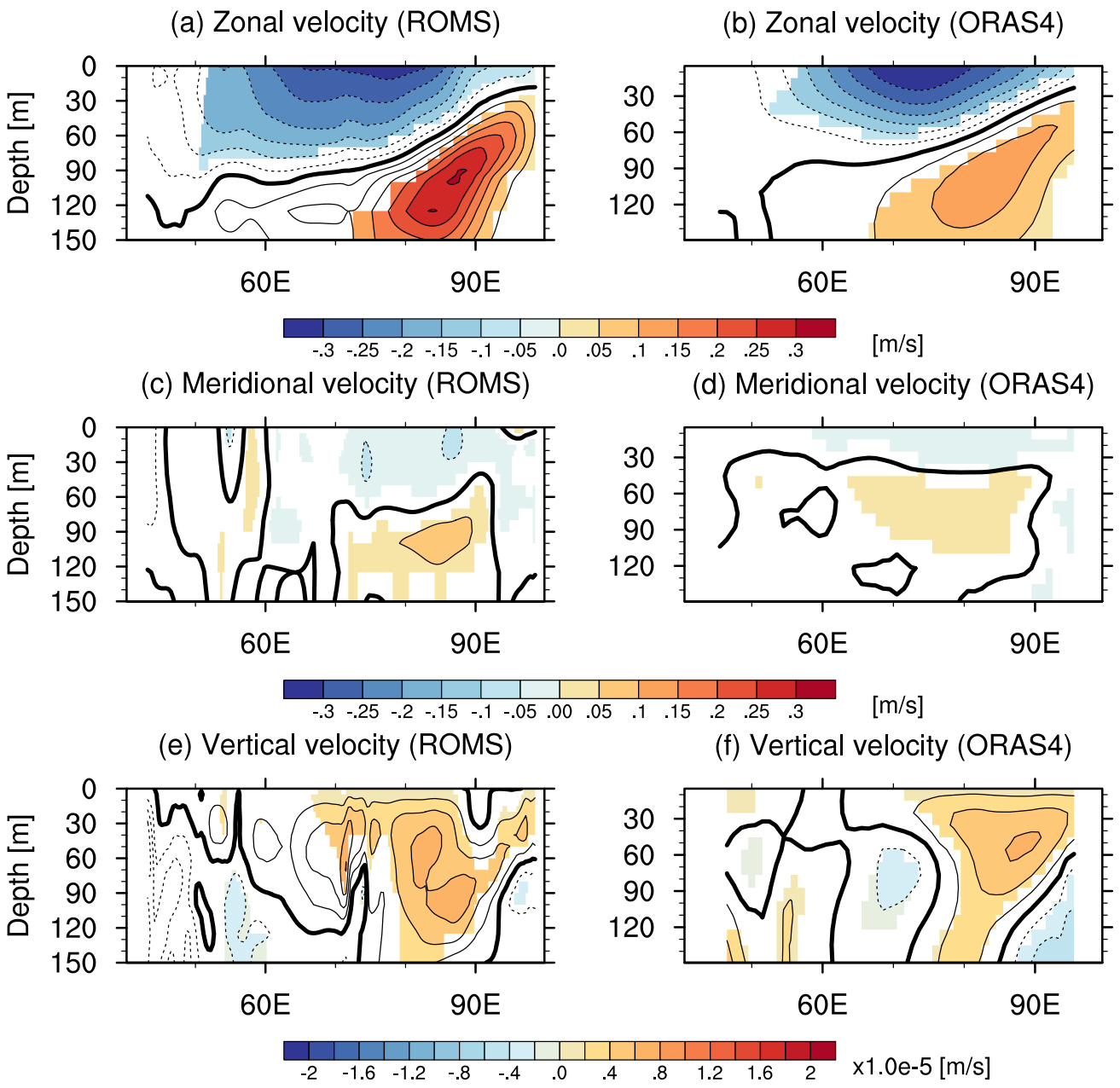

Figure 2.9: Depth-longitude section of composited (a), (b) zonal, (c), (d) meridional, and (e), (f) vertical velocity along the equator (in [m/s]) (averaged over 1.5°S-1.5°N) during SON of pIOD years from the ROMS MR (left) and ORAS4 (right). Anomalies significant at the 90% confidence level by a two-tailed t test are shaded. The contour intervals in (a)-(d) are 0.05 [m/s], whereas those in (e)-(f) are 2.0×10^{-6} [m/s].

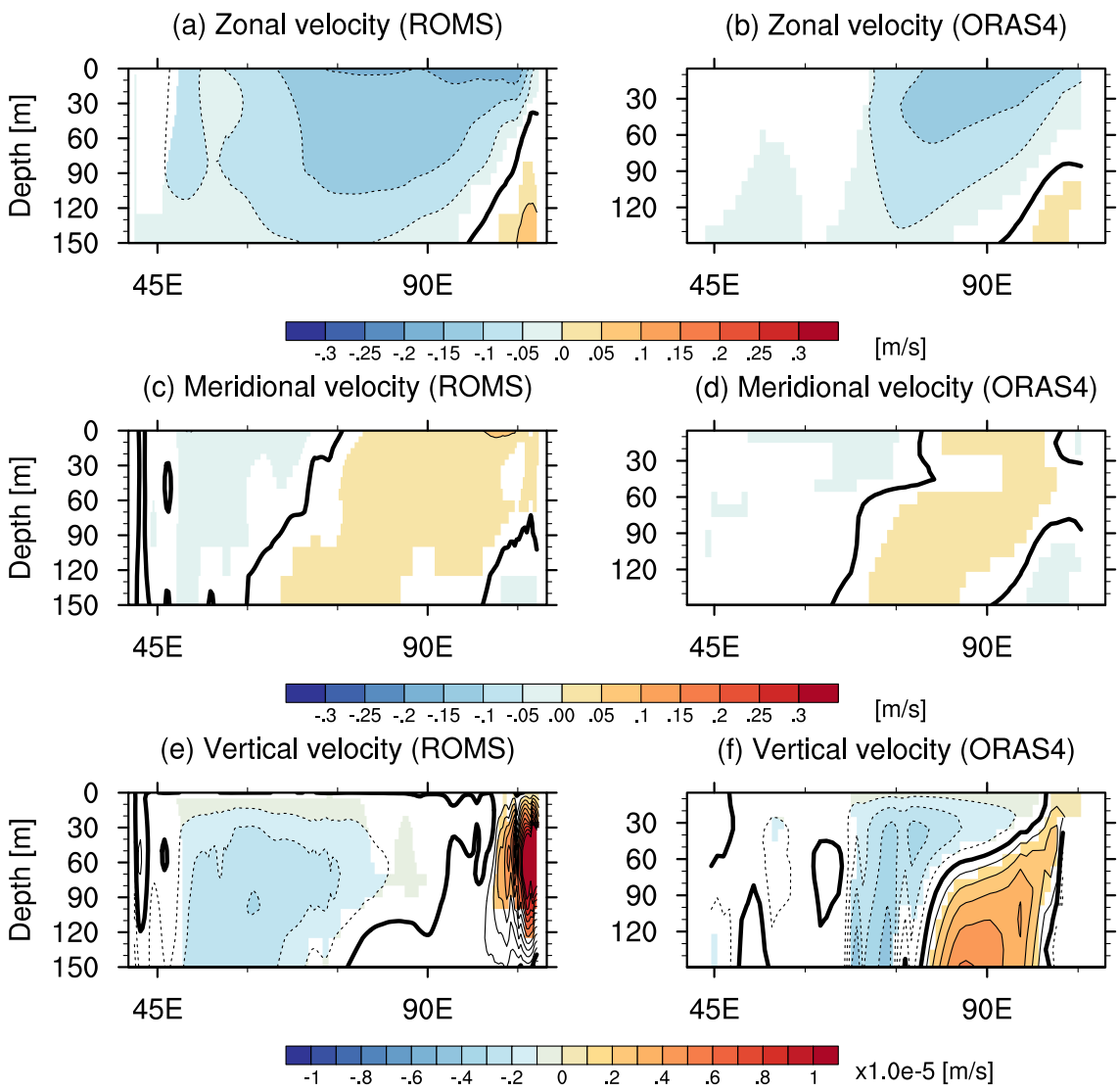

Figure 2.10: As in Fig. 2.9, but for the off-equatorial band (8.5°S-4.5°S). The contour intervals in (e)-(f) are 1.0×10^{-6} [m/s].

For the off-equatorial region (Fig. 2.10), there are significant near-surface westward current anomalies over the eastern-central part. For zonal velocity, westward current anomalies extend over the central-western part of the basin, where downwelling anomalies are seen (Figs. 2.10b, f), suggesting the westward and downward propagation of energy associated with equatorial Rossby waves (RWs). Indeed, the first meridional mode equatorial RW-like structures are clearly seen in the subsurface temperature (Figs. 2.7c, d) and salinity (Figs. 2.8c, d) anomalies. More discussions on the

link between the RWs and subsurface salinity will be presented in section 2.4.1. On the other hand, upwelling anomalies are present in the eastern basin (Fig. 2.10f), which seem to be related to upwelling RWs reflected from the eastern boundary (see Fig. 2.7d). Again, the model does a good job in reproducing the gross features in the ORAS4 (Figs. 2.10a, c, e), despite some differences. Somewhat larger discrepancies in the vertical velocity may partly be due to their indirect estimation in the ORAS4. Indeed, the vertical velocity anomalies in other ocean reanalysis products, which provide it as direct outputs (e.g. the ORAS3), show a better agreement with those in the model. The overall good agreement between the model and ORAS4 gives us confidence in further use of the model for a more detailed investigation. Also, the time series of area-averaged modeled temperature, salinity, and current anomalies from the model correspond well with those from the ORAS3 and ORAS4 (Figure not shown), suggesting that our model has succeeded in reproducing the observed oceanic variability in the tropical IO.

2.4. Mechanisms of salinity anomalies

2.4.1 Process contributing to salinity anomalies

To assess the relative contribution of various atmospheric forcing, we analyze outputs of sensitivity experiments described in section 2.2.3. As shown in Fig. 2.11, the total IOD-related effect on SSS, which is measured by the difference between MR and NoIOD experiment, bears a striking resemblance to the observed SSS anomalies during the pIOD (compare Fig. 2.11 with Fig. 2.8). By comparing individual contribution from each effect, we can infer their relative importance in the generation of total SSS anomalies. As shown in Fig. 2.11d, surface freshening near the equator are mainly dominated by the wind-stress effect, which is measured by the MR minus NoSTRESS solution. This result suggests that wind-driven dynamical processes, rather than anomalous precipitation/evaporation and associated changes in freshwater fluxes, are crucial for the generation of these anomalies. On the other hand, surface saltening in the SEIO are explained by the sum of the precipitation effect (measured by the MR minus NoPRCP solution) and the wind speed effect (measured by the NoSTRESS minus NoWIND solution) (Figs. 2.11e, f). These results can be explained by the reduction of precipitation and increase of evaporation due to acceleration of southeasterly wind (see green contours in Figs. 2.11e, f). Shortwave radiation anomalies, which may potentially affect SSS by changing evaporation and mixed layer depth, have negligible contribution to SSS anomalies (Fig. 2.11g). Similarly, the impact of lateral boundary forcing is also very small except for the eastern part of the Java Sea (Fig. 2.11h). The sum of all effects, which is shown in Fig. 2.11b, almost entirely explains the total anomalies (Fig. 2.11a). Here, we note that experiments with different approaches (e.g. integrate the model with the NoIOD forcing for all fields except for a specific variable, and subtract them from the results of NoIOD experiments…etc) have been also conducted for some specific years to check the validity and robustness of framework. Their results are qualitatively very similar to what we have presented above (figure not shown), suggesting that

the total SSS anomalies can be approximated by a linear combination of each process for most regions. Small positive residuals extending over the SEIO may be due to nonlinearity arising from vigorous eddy activity over there (Fig. 2.11c).

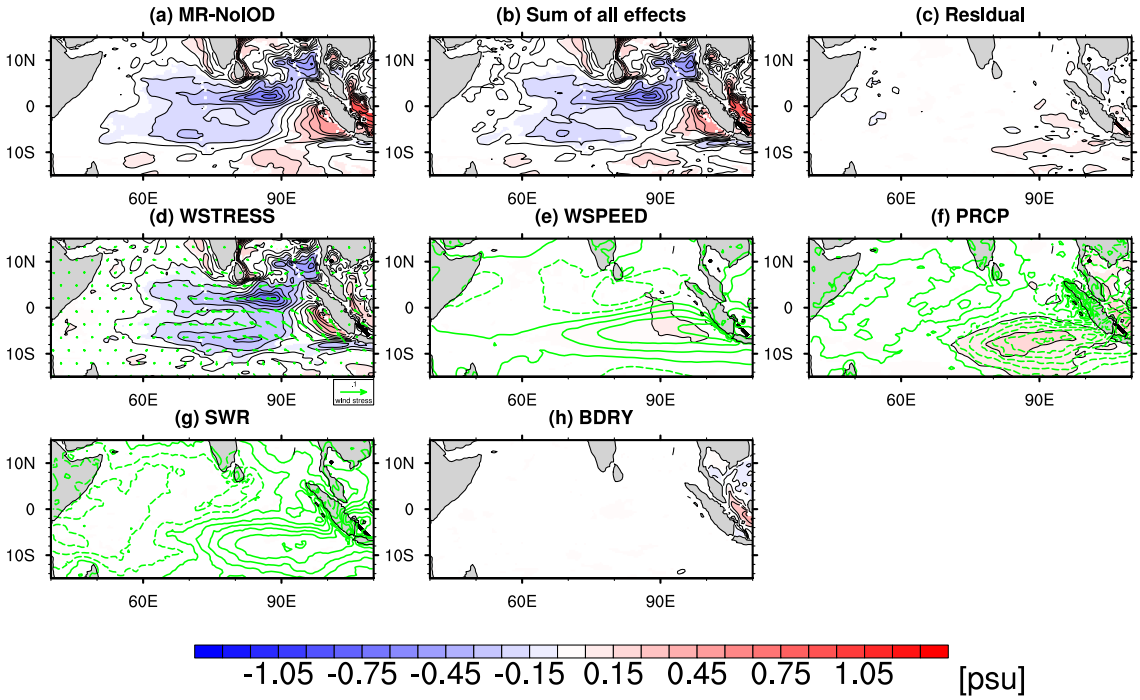

Figure 2.11: (a) Composite of SSS (vertically averaged over the upper 30 [m]) difference between the MR and NoIOD run during SON of pIOD events (in [psu]). (d)-(h): As in (a), but for the wind stress effect (d: measured by the MR-NoSTRESS solution), the wind speed effect (e: NoSTRESS-NoWIND), the precipitation effect (f: MR-NoPRCP), the shortwave radiation effect (g: MR-NoSWR), and the boundary forcing effect (h: MR-NoBDRY). The sum of (d)-(h) is shown in (b), and the difference between (a) and (b) is shown in (c). The contour intervals are 0.1 [psu], and anomalies significant at the 90% confidence level by a two-tailed t test are shaded. Green vectors in (d) represent wind stress anomalies (in [N/m^2]), while green contours in (e), (f), (g) are wind speed (CI: 1 [m/s]), precipitation (CI: 1.0×10^{-7} [m/s]), and net shortwave radiation (CI: 5

[W/m^2]) anomalies, respectively.

Similar to SSS, the impact of total IOD-related effects on subsurface salinity is well captured by the MR-NoIOD solution (Figs. 2.8d, 2.12a). Both negative anomalies in the off-equatorial bands and positive anomalies in the EEIO are mainly caused by the wind-stress effect (Fig. 2.12d). The precipitation effect plays only a minor role over the entire domain, except for the SEIO (Fig. 2.12f). Contributions from wind-speed, shortwave radiation, and lateral boundary forcing are much weaker (Figs. 2.12e, g, h). Therefore, it is wind stress anomalies that play the dominant role for the generation of subsurface salinity anomalies over the IO.

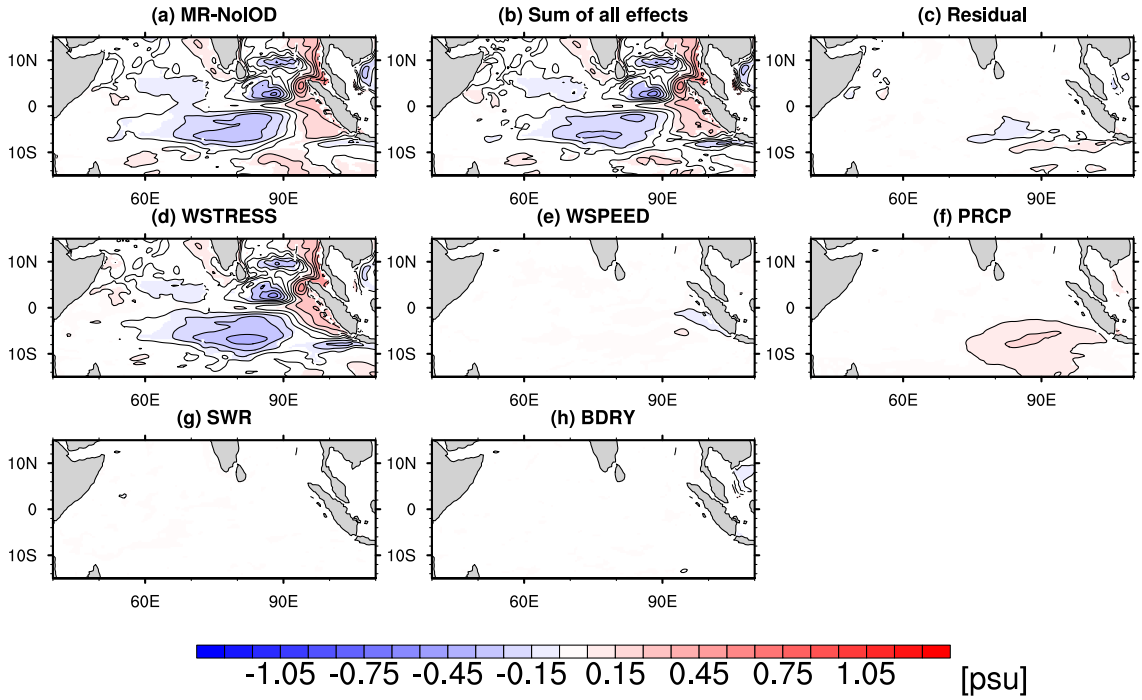

Figure 2.12: As in Fig. 2.11, but for subsurface salinity anomalies (vertically averaged from 50 [m] to 100 [m] depth).

The dominance of the wind stress effect in the generation of the subsurface salinity anomalies implies that wind-induced wave adjustments and associated current anomalies play crucial

roles. To highlight this point, time-longitude sections of zonal wind stress, Ekman pumping velocity, sea level, and subsurface salinity anomalies for equatorial and off-equatorial band are shown in Fig. 2.13. During the pIOD, anomalous easterly winds along the equator (Fig. 2.13a) cause equatorial surface Ekman divergence, induce upwelling and lift the halocline especially in the EEIO (Fig. 2.13b) due to the fast eastward propagation of equatorial Kelvin waves, contributing to the subsurface saltening there. On the other hand, the equatorial easterlies also cause off-equatorial Ekman convergence, increase sea level and deepen the halocline, resulting in the off-equatorial maxima of sea level anomalies near 4.5°S-8.5°S and 4.5°N-8.5°N (Figs. 2.13e, h). This anomalous sea level pattern is the typical structure of the first meridional mode equatorial RW. Meanwhile, the negative Ekman pumping velocities over the off-equatorial regions (Figs. 2.13d, g) associated with anomalous anticyclonic wind stress curls (Eq. (2.13) below) enhance the downwelling and halocline deepening induced by the equatorial easterlies, causing the low salinity anomalies in the subsurface ocean (Figs. 2.13f, i). Here, the Ekman pumping velocity, W_e, is calculated as follows:

$$W_e = \frac{1}{\rho_0}\left[\frac{\partial}{\partial x}\left(\frac{\tau^y}{f}\right) - \frac{\partial}{\partial y}\left(\frac{\tau^x}{f}\right)\right]. \quad (2.13)$$

Here, ρ_0 is the reference density (=1024 [kg/m^3]) and f is the Coriolis parameter. These downwelling RWs propagate westward (Figs. 2.13e, h) and push the fresher surface water downward, giving rise to the negative subsurface salinity anomalies across the interior basin (Figs. 2.11a, 2.12a). Though the overall structure of anomalies in both hemispheres looks quite similar, anomalies in the Southern Hemisphere (Figs. 2.13e, f) have larger magnitude compared to those in the Northern Hemisphere (Figs. 2.13h, i). This north-south difference in the strength of the oceanic signals may be partly due to cross-equatorial asymmetry in the wind anomalies (Figs. 2.13d, g). Though many observational and modeling studies have discussed the propagation of RWs based on the sea level, thermocline depth (Chowdary et al., 2009; Masumoto & Meyers, 1998; Xie et al., 2002) and SSS

anomalies (Du & Zhang, 2015), our results demonstrate that subsurface salinity can be also used to monitor the RWs. More comprehensive and quantitative discussions regarding the mechanisms of salinity anomalies will be provided in the following subsections.

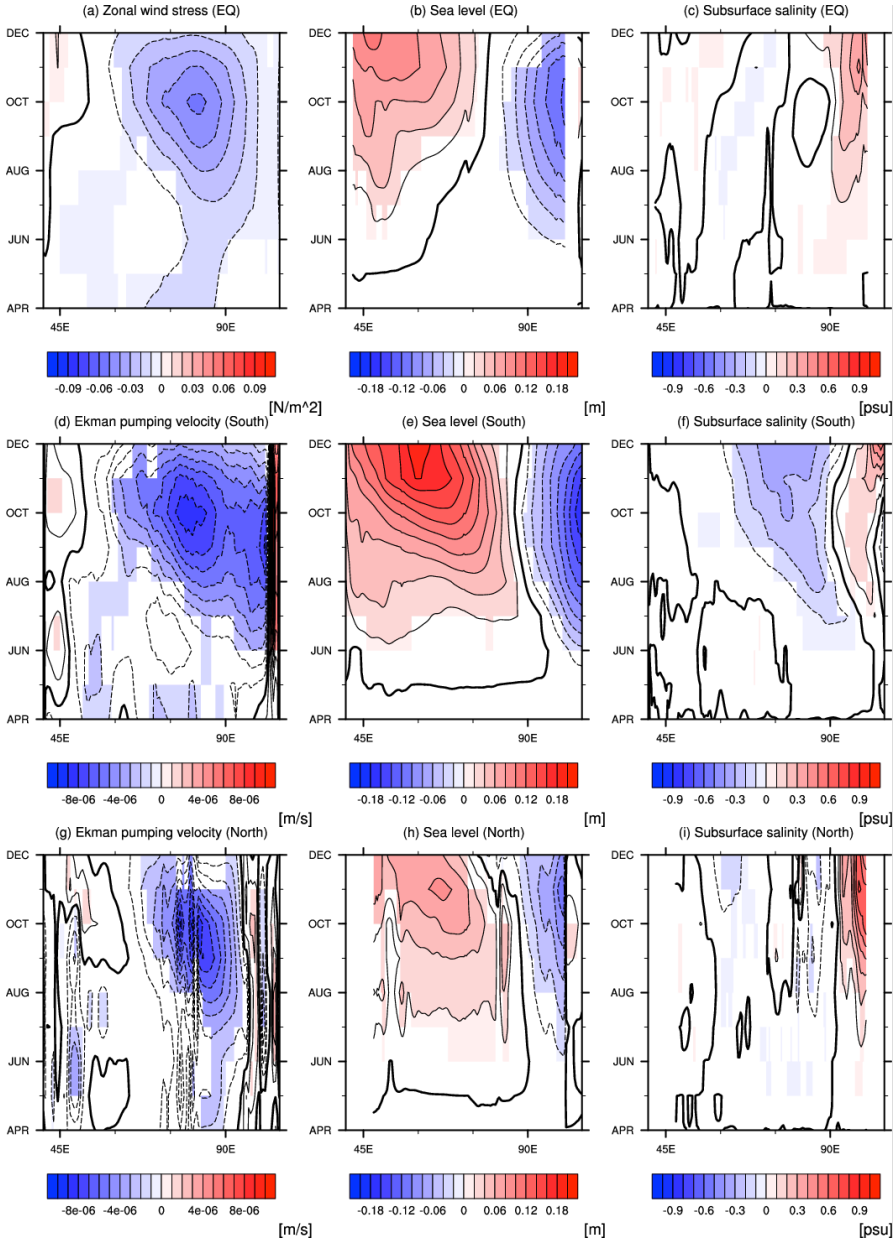

Figure 2.13: Longitude-time section of composited (a) zonal wind stress anomalies (in [N/m^2]: CI=0.01 [N/m^2]), (b) sea level (in [m]: CI=0.02 [m]), and (c) subsurface salinity (in [psu]: CI=0.1 [psu]: vertically averaged from 50 [m] to 100 [m] depth) difference between MR and NoIOD run along the equator (meridionally averaged over 1.5°S-1.5°N)

during the pIOD. (d) As in (a), but for the Ekman pumping velocity (in [m/s]: CI=1.0×10^{-6} [m/s]) over the southern tropical Indian Ocean (meridionally averaged over 8.5°S-4.5°S). (e), (f): As in (b) and (c), but for the southern tropical Indian Ocean (the latitudinal range is the same with (d)). (g)-(i) As in (d)-(f), but for the northern tropical Indian Ocean (meridionally averaged over 4.5°N-8.5°N). Anomalies significant at the 90% confidence level by a two-tailed t test are shaded.

2.4.2 Salinity budget analysis

By analyzing the results from sensitivity experiments, we have succeeded in isolating various complex processes that simultaneously affect the generation of salinity anomalies. However, it is difficult to fully understand the physical processes that contribute to the observed anomalies only from these sensitivity experiments. For example, the wind stress effect contains all kinds of "wind-driven dynamical effects", such as horizontal/vertical advection and vertical mixing. To further elucidate the mechanisms of salinity anomalies, we have performed an online salinity budget analysis using the ROMS.

The time evolution of salinity can be written as follows:

$$\underbrace{\frac{\partial S}{\partial t}}_{ST} = \underbrace{-u\frac{\partial S}{\partial x}}_{ZADV}\underbrace{-v\frac{\partial S}{\partial y}}_{MADV}\underbrace{-w\frac{\partial S}{\partial z}}_{VADV}\underbrace{+\frac{\partial}{\partial x}\left(\kappa_H\frac{\partial S}{\partial x}\right)+\frac{\partial}{\partial y}\left(\kappa_H\frac{\partial S}{\partial y}\right)}_{HDIFF}\underbrace{+\frac{\partial}{\partial z}\left(\kappa_v\frac{\partial S}{\partial z}\right)}_{VDIFF}, \tag{2.14}$$

where S is salinity, u, v, w denote zonal, meridional and vertical velocity, respectively, and κ_H and κ_v are horizontal and vertical diffusion coefficients, respectively. Note that the effect of freshwater flux is implicitly incorporated as the boundary condition of vertical salinity diffusion (i.e. $\kappa_v\frac{\partial S}{\partial z} = S(E-P)$ at the surface, where E and P represent evaporation and precipitation, respectively). During the integration, each term on the right hand side of Eq. (2.14) is calculated at

every time step and stored as 3-day averaged value. The results presented below are the composite differences of each term of Eq. (2.14) between MR and NoIOD run, which delineate essential generation mechanisms of salinity anomalies common to pIOD events.

Figure 2.14 shows composites of anomalies in salinity tendency terms along the equator. Consistent with simulated salinity anomalies (Fig. 2.8), significant negative tendency anomalies (i.e. freshening) extend from the central to the eastern IO near the surface, whereas positive anomalies are evident around 30-100 [m] depth in the eastern IO. Since we have conducted an online salinity budget analysis, the sum of all terms on the right hand side of Eq. (2.14) is *exactly the* same with the left hand side (Fig. 2.14b). By comparing the relative contribution of each process, we can see that the near surface freshening is mainly due to zonal salinity advection anomalies (Fig. 2.14c). These results are consistent with previous studies, which have pointed out that the reversal of zonal current and associated weakening of salt transport from the western IO are primary causes of these anomalies (J. Li et al., 2016; Y. Zhang et al., 2013). On the other hand, subsurface saltening in the east is mainly explained by vertical salinity advection anomalies (Fig. 2.14e), while meridional advection anomalies also play an important role in determining its vertical structure (Fig. 2.14d). Vertical salinity diffusion anomalies mainly act to damp the salinity anomalies (Fig. 2.14e). The overall control of total anomalies by advective processes is in accord with the results from sensitivity experiments that point out the dominance of the wind-stress effects.

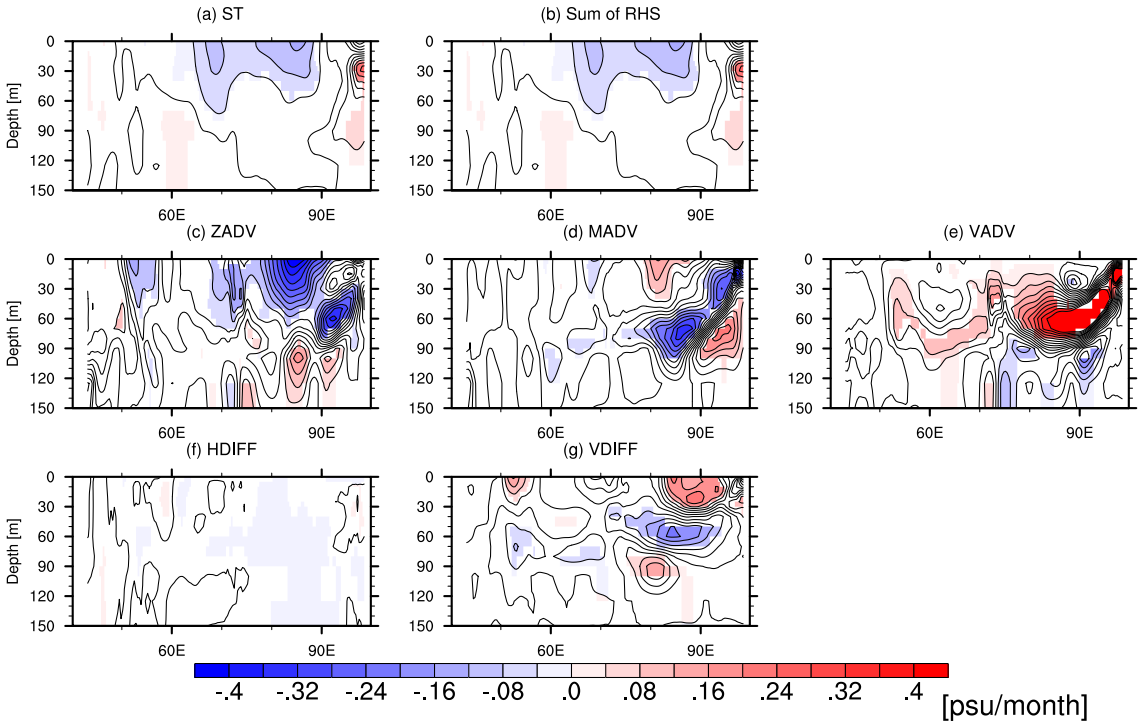

Figure 2.14: Composite of the difference of equation (2.14) between MR and NoIOD during August-October (ASO) of pIOD events along the equator (meridionally averaged over 1.5°S-1.5°N) (in [psu/month]). The contour intervals are 0.04 [psu/month], and anomalies significant at the 90% confidence level by a two-tailed t test are shaded.

For off-equatorial salinity anomalies, significant positive tendency anomalies are found near the surface in the east (Fig. 2.15a), consistent with saltening there. These positive anomalies are mainly explained by vertical diffusion anomalies (Fig. 2.15g), while zonal advection anomalies act to damp them (Fig. 2.15c). These vertical diffusion anomalies are linked with positive freshwater flux anomalies (i.e. reduction of precipitation and increase of evaporation) and associated increase of SSS there (Figs. 2.11e, f).

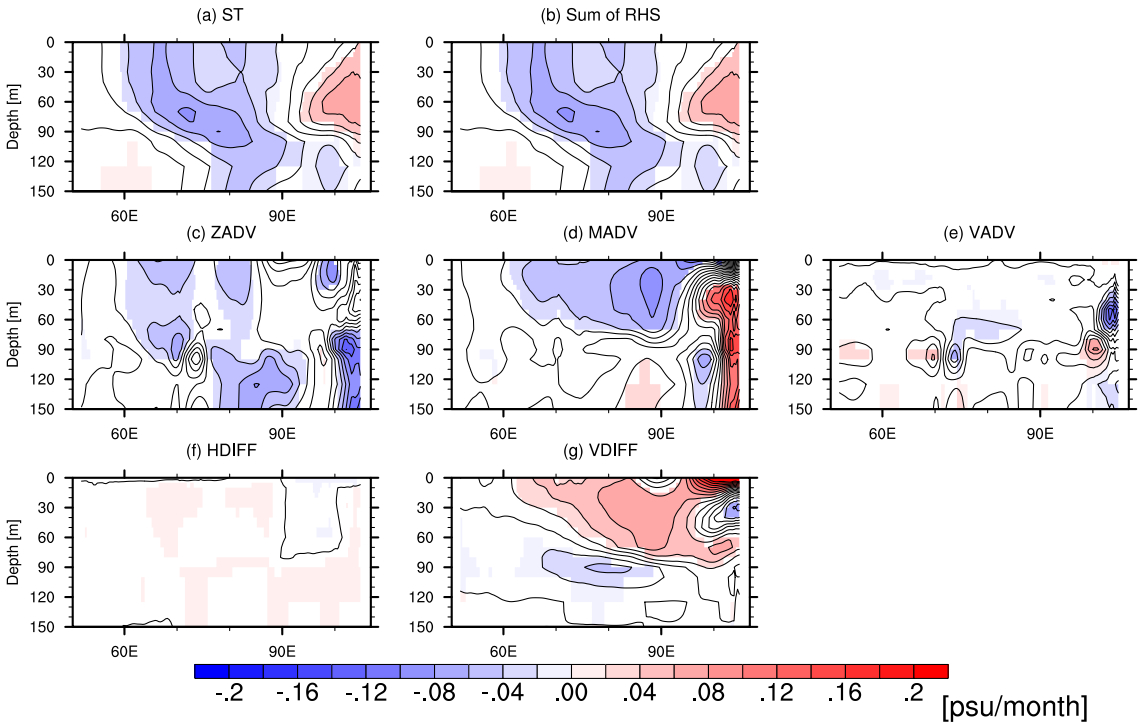

Figure 2.15: *As* in Fig. 2.14, but for the off-equatorial region (averaged over 8.5°S-4.5°S).

On the other hand, negative tendency anomalies are seen around 60-90 [m] depth in the central-western part (Fig. 2.15a). These are due to the combination of zonal advection, vertical advection, and vertical diffusion anomalies (Figs. 2.15c, e, g). Composite of the vertical salinity diffusion coefficients shows positive anomalies around this depth (Fig. 2.16a), implying strengthening of vertical mixing there. A comparison of contributions from various factors reveals that they are mainly due to the wind stress effect (Fig. 2.16d), while the wind speed and precipitation effects also play a secondary role. Recall that all dynamical effects of the wind anomalies (both through advection and mixing) are mediated only by wind stress, and wind speed is solely used for the calculation of turbulent heat/freshwater fluxes in our experimental setting. Therefore, if the enhanced mixing is caused by the decrease of buoyancy flux (i.e. decrease of net heat and freshwater flux), these should be reflected in the wind speed and precipitation effects. However, contributions

from these effects are weaker than those from the wind stress effect, particularly the regions west of 90°E (Figs. 2.16e, f, g). These results indicate that anomalously strong mixing there is mainly caused by increase of upper ocean shear associated with enhanced surface wind, rather than by themodynamical effects. Such enhanced vertical mixing leads to an anomalous increase in downward intrusion of surface low-salinity water to the lower layer and gives rise to anomalous freshening (saltening) below (above) the pycnocline.

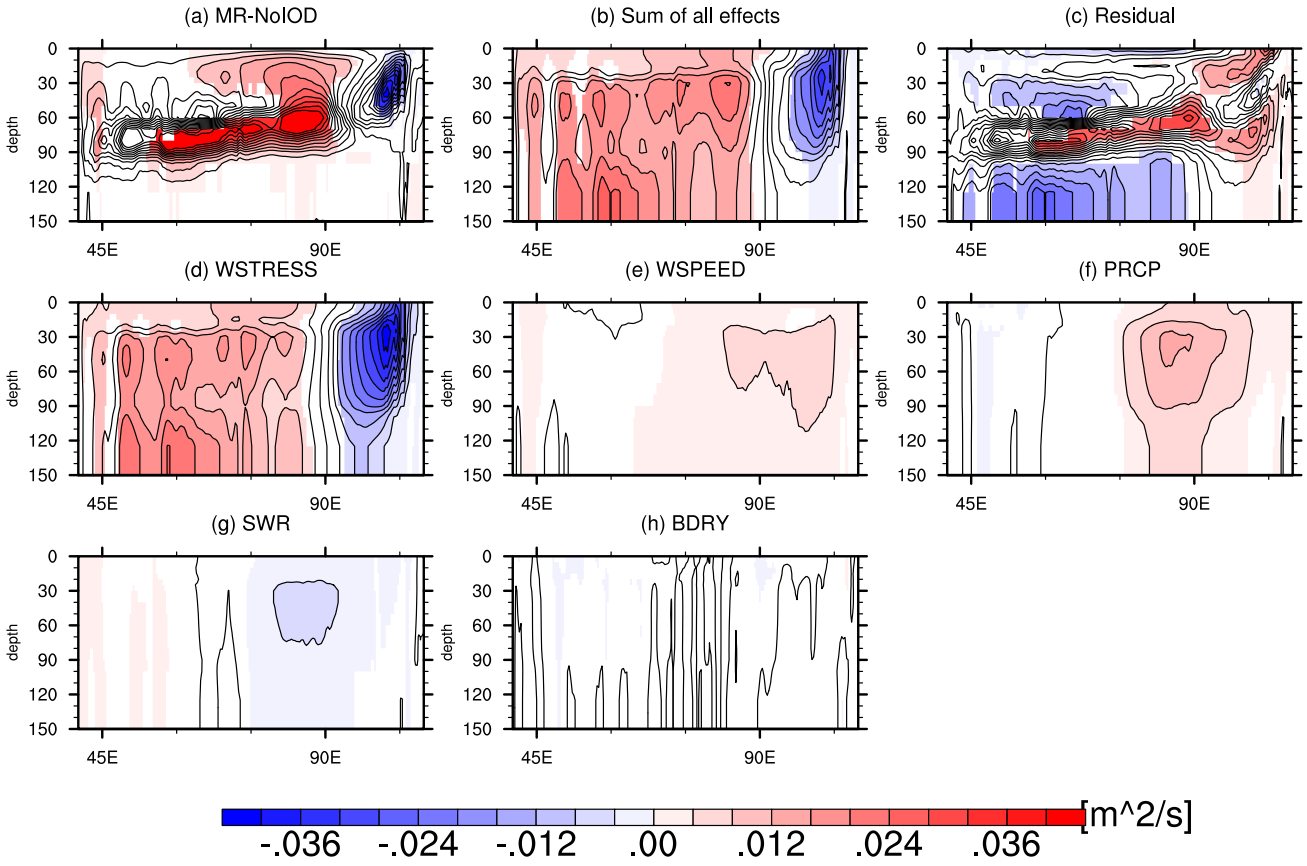

Figure 2.16: (a) Composite of vertical diffusion coefficient difference between the MR and NoIOD run during ASO of pIOD events (in [m^2/s]) for the off-equatorial region (averaged over 8.5°S-4.5°S). (d)-(h): As in (a), but for the wind stress effect (d: measured by the MR-NoSTRESS solution), the wind speed effect (e: NoSTRESS-NoWIND), the precipitation effect (f: MR-NoPRCP), the shortwave

radiation effect (g: MR-NoSWR), and the boundary forcing effect (h: MR–NoBDRY). The sum of (d)-(h) is shown in (b), and the difference between (a) and (b) is shown in (c). The contour intervals are 4.0×10^{-3} [m^2/s], and anomalies significant at the 90% confidence level by a two-tailed t test are shaded.

2.4.3 Decomposition of advective anomalies

To further understand the origin of advective anomalies, we have decomposed the advective terms. As a first step, we have estimated the advective terms using 3-day averaged outputs of current and salinity through an offline analysis. For example, the zonal salinity advection term can be approximated by

$$(-u\frac{\partial S}{\partial x})_{online} = (-u\frac{\partial S}{\partial x})_{offline} + (Res.) = -u_{3days}\frac{\partial S_{3days}}{\partial x} + (Res.), \tag{2.15}$$

where u_{3days} and S_{3days} are 3-day averaged zonal velocity and salinity, respectively, and the residual term contains errors due to the use of a different spatial discretization and contribution of high-frequency terms that cannot be estimated by an offline calculation. Since both u_{3days} and S_{3days} contain variability with various timescale, they are decomposed into seasonal, intraseasonal, and interannual components:

$$u = \bar{u} + u' + u'' \tag{2.16}$$
$$S = \bar{S} + S' + S'',$$

where $\bar{X}$ is the long-term climatology (including the seasonal cycle), and X' (X'') is low-passed (high-passed) anomalies, which are obtained by applying the Lanczos low-pass (high-pass) filter with a cutoff period of 105 days to the anomalies (i.e. $X - \bar{X}$). Note that subscripts "3days" are omitted for conciseness.

By substituting Eq. (2.16) into Eq. (2.15), the advective term can be written as follows:

$$\begin{aligned}(-u\frac{\partial S}{\partial x})_{online} = (-u\frac{\partial S}{\partial x})_{offline} + (Res.) &= -(\bar{u} + u' + u'')\frac{\partial}{\partial x}(\bar{S} + S' + S'') + (Res.) \\ &= \underbrace{-\bar{u}\frac{\partial \bar{S}}{\partial x}}_{Term\ 1} + \underbrace{(-\bar{u}\frac{\partial S'}{\partial x})}_{Term\ 2} + \underbrace{(-u'\frac{\partial \bar{S}}{\partial x})}_{Term\ 3} + \underbrace{(-u'\frac{\partial S'}{\partial x})}_{Term\ 4} + \underbrace{(-\bar{u}\frac{\partial S''}{\partial x})}_{Term\ 5} + \underbrace{(-u''\frac{\partial \bar{S}}{\partial x})}_{Term\ 6} \\ &+ \underbrace{(-u''\frac{\partial S''}{\partial x})}_{Term\ 7} + \underbrace{(-u''\frac{\partial S'}{\partial x})}_{Term\ 8} + \underbrace{(-u'\frac{\partial S''}{\partial x})}_{Term\ 9} + (Res.).\end{aligned} \tag{2.17}$$

The first term on the right hand side of Eq. (2.17) is the advection of the climatological salinity field

by the climatological current. Similarly, the second (third) term represents the advection of the interannual (climatological) salinity gradient by the climatological (interannual) current. The fourth term is a nonlinear term due to covariance between interannual current and salinity gradient anomalies. Terms 5-7 are similar to Terms 2-4 but replacing interannual anomalies with intraseasonal anomalies. Terms 8 and 9 are higher-order terms, arising from correlation between interannual and intraseasonal anomalies. Using a similar approach, meridional and vertical advection terms can also be decomposed. All the terms presented above are calculated using outputs from the MR and the NoIOD run, and we will examine their differences to identify important processes at work. Since many previous studies have used monthly-mean data for salinity budget analysis (e.g. Y. Zhang et al., 2013), they have mainly focused on Terms 2-4 to explain the cause of advective anomalies. However, we will show that Term 7, which represents interannual modulation in nonlinear rectification of intraseasonal variability, also plays a pivotal role in the evolution of salinity anomalies.

Figure 2.17 shows each term on the right hand side of Eq. (2.17) as a depth-longitude section along the equator. Since Terms 5, 6, 8, and 9 are considerably smaller than others, only their sum is shown. For zonal advection anomalies, negative anomalies near the surface in the central part and subsurface positive anomalies in the east are mainly explained by Term 3, and Terms 2 and 4 tend to offset the total anomalies. The pattern of Term 3 reflects the deceleration of surface eastward jet and acceleration of the EUC, which contributes to freshening and saltening, respectively, supporting arguments presented by many previous studies (Fig. 2.9) (J. Li et al., 2016; Y. Zhang et al., 2013). Contributions from other terms and residual are generally small. Similarly, decomposition of vertical advection anomalies reveals that positive subsurface anomalies in the east are mostly due to interannual anomalies (Terms 2-4). These results clearly demonstrate that enhanced upwelling and

associated increase of upward transport of salty water are crucial for positive salinity anomalies in the EEIO.

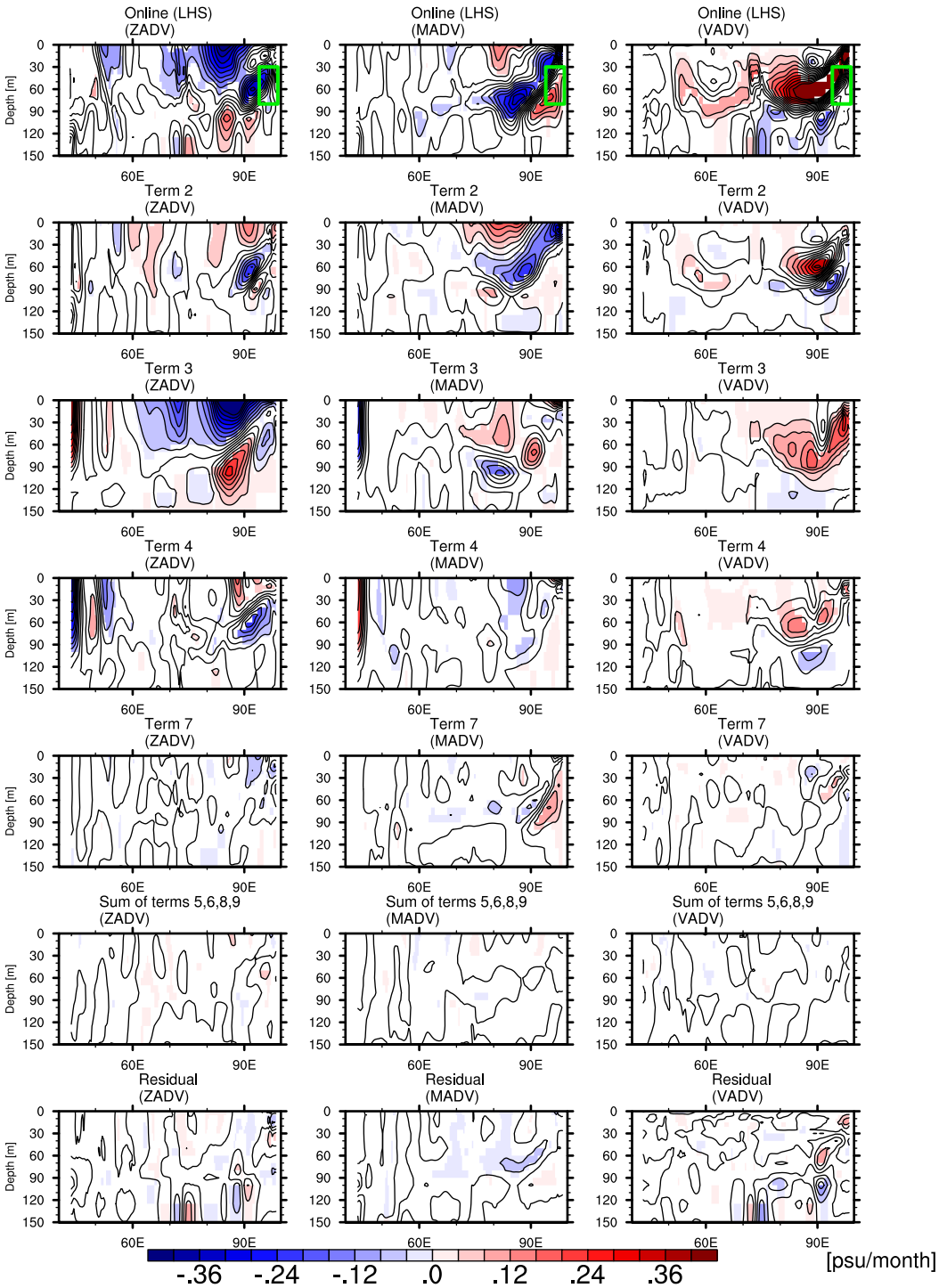

Figure 2.17: Composite of zonal (left), meridional (middle), and vertical (right) salinity advection anomalies (left hand side, Terms 2, 3, 4, and 7, sum of Terms 5, 6, 8, and 9,

and residual of Eq. (2.17) during ASO of pIOD years along the equator (meridionally averaged over 1.5°S-1.5°N) (in [psu/month]). The contour intervals are 0.04 [psu/month], and anomalies significant at the 90% confidence level by a two-tailed t test are shaded. The green boxes in the top panels represent the region used to define the area-averaged values.

On the other hand, meridional advection anomalies cannot be totally explained by interannual components (i.e. Terms 2-4). In particular, positive anomalies in the EEIO are largely due to Term 7, which has vertical dipole structure with negative (positive) anomalies above (below) the pycnocline. Indeed, box-averaged values of each term near the pycnocline in the EEIO (averaged over 94°E-100°E, 1.5°S-1.5°N, 30-100 [m] depth) suggest that Term 7 explains almost entire fraction of the meridional advection anomalies and its value is comparable to total tendency anomalies (Fig. 2.18a). The sum of Terms 5, 6, 8, and 9 is smaller than others, but the residual term has vertical structure somewhat similar to that of Term 7. This suggests that some portion of nonlinear advection due to high-frequency variability may not be completely captured by the offline analysis presented here (recall that 3-day averaged data cannot capture variability with a period shorter than 6 days).

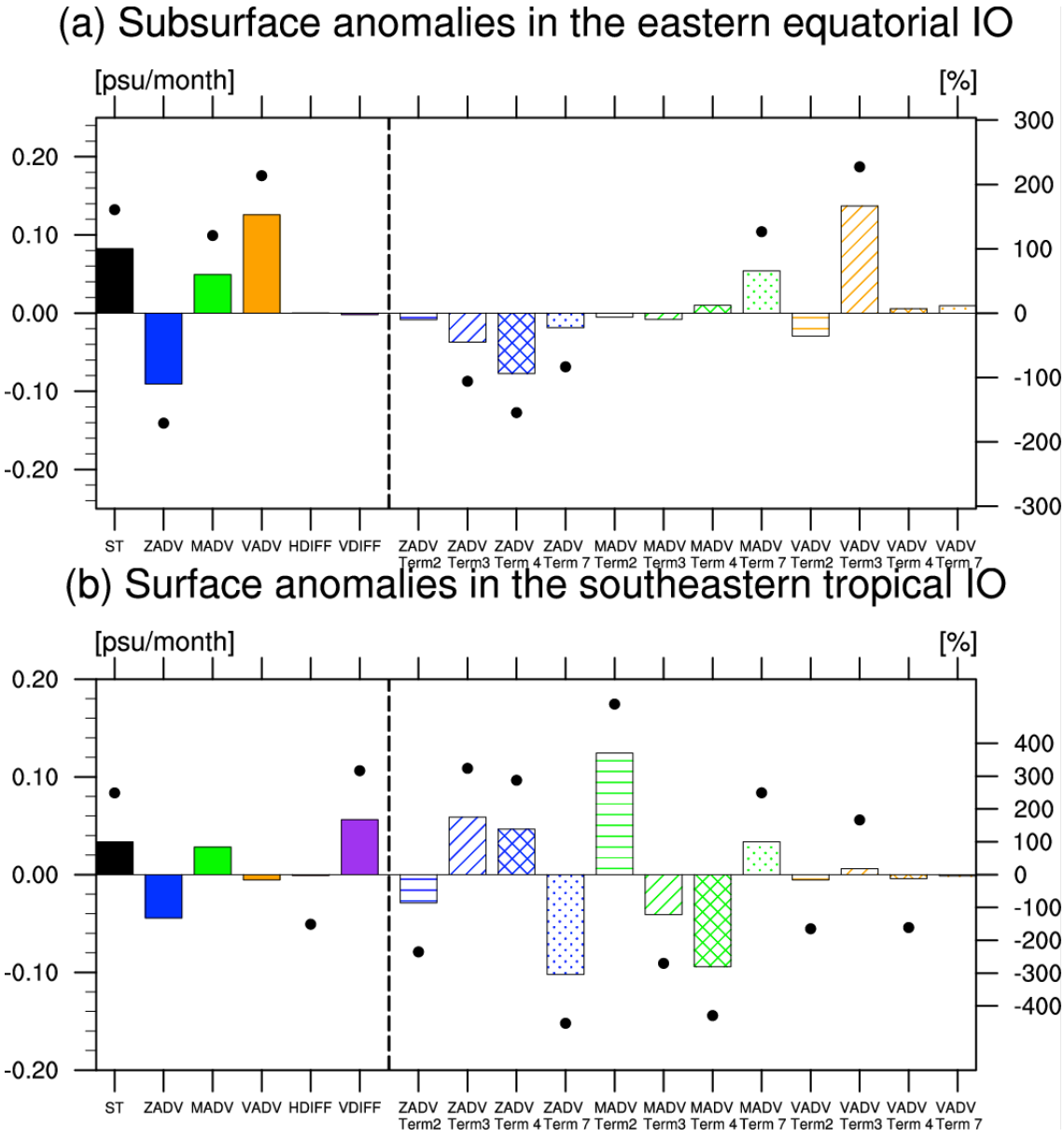

Figure 2.18: (a) Area-averaged salinity tendency and advection anomalies during ASO of pIOD years in the eastern equatorial IO (94°E-100°E, 1.5°S-1.5°N, 30-100 [m] depth) (in [psu/month]). Dots above or below each bar indicate that these anomalies are significant at the 90% confidence level by a two-tailed t test. Also, numbers shown in the right hand side of the figure represent the proportion of each term to the total tendency anomalies (in [%]). (b) As in (a), but for the southeastern tropical IO (averaged over 96°E-105°E, 8.5°S-4.5°S, 0-40 [m] depth).

How can we physically interpret the large differences in Term 7 of meridional advection, which imply modulation of nonlinear meridional salinity advection due to high-frequency anomalies? To address this question, we inspect their original values computed from the MR and the NoIOD run (Fig. 2.19). For both experiments, significant negative values are seen near the pycnocline in the east, indicating that collective effects of intraseasonal variability is *net freshening* there. Nagura et al. (2014) have pointed out that nonlinear heat advection by mixed-Rossby gravity (MRG) waves (generated by both instraseasonal wind forcing and oceanic instability near the western boundary) leads to net warming near the thermocline. They have demonstrated that superposition of multiple vertical baroclinic modes leads to positive correlation between meridional velocity anomalies (i.e., v'') and meridional gradient of density anomalies (i.e., $\frac{\partial \rho''}{\partial y}$), and gives rise to net decrease of density (i.e., $\overline{-v''\frac{\partial \rho''}{\partial y}} < 0$, where the overbar denotes the long-term mean) (Nagura et al., 2014; Smyth et al., 2015; see also analytical derivation in Ogata et al., 2017). Given that both warming and freshening are equivalent to decrease of density, net freshening near the pycnocline that appear in the EEIO can be naturally interpreted as another manifestation of these rectification effects by MRG waves. Maximum peak of the $\overline{-v''\frac{\partial S''}{\partial y}} < 0$ is found in the eastern part of the basin, and this may be due to eastward intensification of MRG energy (Miyama et al., 2006) and/or strong salinity stratification in the east (Figs. 2.19a, b). However, why these rectified freshening effects have different vertical structure between MR and NoIOD run? Given that wind forcing at intraseasonal frequency is kept the same between two runs (see section 2.3 for detailed processing of the NoIOD forcing), these results are somewhat puzzling and counterintuitive at first glance.

Our hypothesis is as follows. Easterly wind anomalies along the equator during the pIOD

strengthen upwelling in the EEIO and lift the pycnocline there (Fig. 2.19a). Since the maximum nonlinear advection corresponds to the maximum density gradient (i.e. pycnocline) (Nagura et al., 2014; Smyth et al., 2015), the location of net freshening also shifts upward (compare Fig. 2.19a with Fig. 2.19b). In other words, the changes in the background condition lead to different vertical structures of rectified effects and explain the negative (positive) anomalies above the pycnocline (Fig. 2.19c). Additional sensitivity experiments using a linear continuously stratified model further supports this idea, and will be discussed in the next subsection.

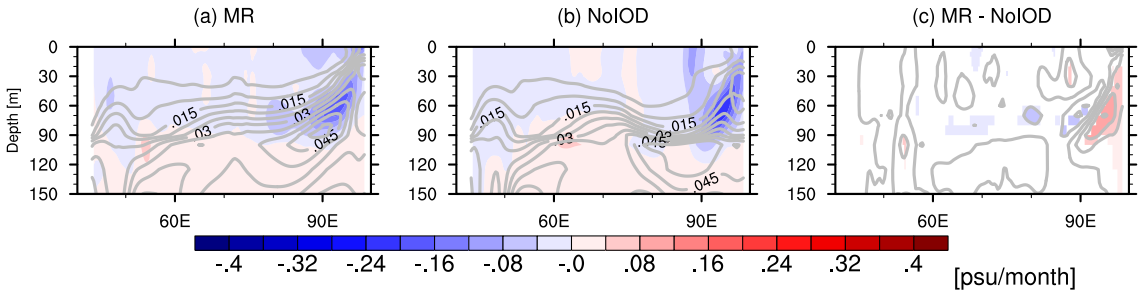

Figure 2.19: Depth-longitude section of Term 7 of meridional advection on the right hand side of Eq. (2.17) during ASO of pIOD years along the equator (meridionally averaged over 1.5°S-1.5°N) from (a) the MR, (b) the NoIOD run, and (c) the difference between MR and NoIOD run. Contours in (a) and (b) represent density gradient, and their intervals are 0.005 [kg/m^4]. The contour intervals in (c) are 0.04 [psu/month], and differences significant at the 90% confidence level with a two-tailed t test are shaded.

Similar to the equatorial band, we have also decomposed advection anomalies for the off-equatorial region (Fig. 2.20). Again, total anomalies are mainly dominated by interannual components, and contributions from high-order terms (Terms 5, 6, 8, and 9) and residuals are small. In particular, negative subsurface anomalies in the central part are mostly explained by Term 3 of zonal and vertical salinity advection, which correspond to westward and downwelling current

anomalies, respectively, and associated increase of freshwater transport (Fig. 2.10). As in the equatorial region, Terms 2 and 4 counteract the total anomalies. Therefore, the emerging picture portrayed by precise salinity budget analysis generally supports previous studies. Nevertheless, Term 7 of zonal and meridional advection, which depicts low-frequency modulation of nonlinear horizontal advection due to high-frequency variability, has non-negligible, or even dominant contribution in the SEIO, as clearly illustrated by Fig. 2.18b.

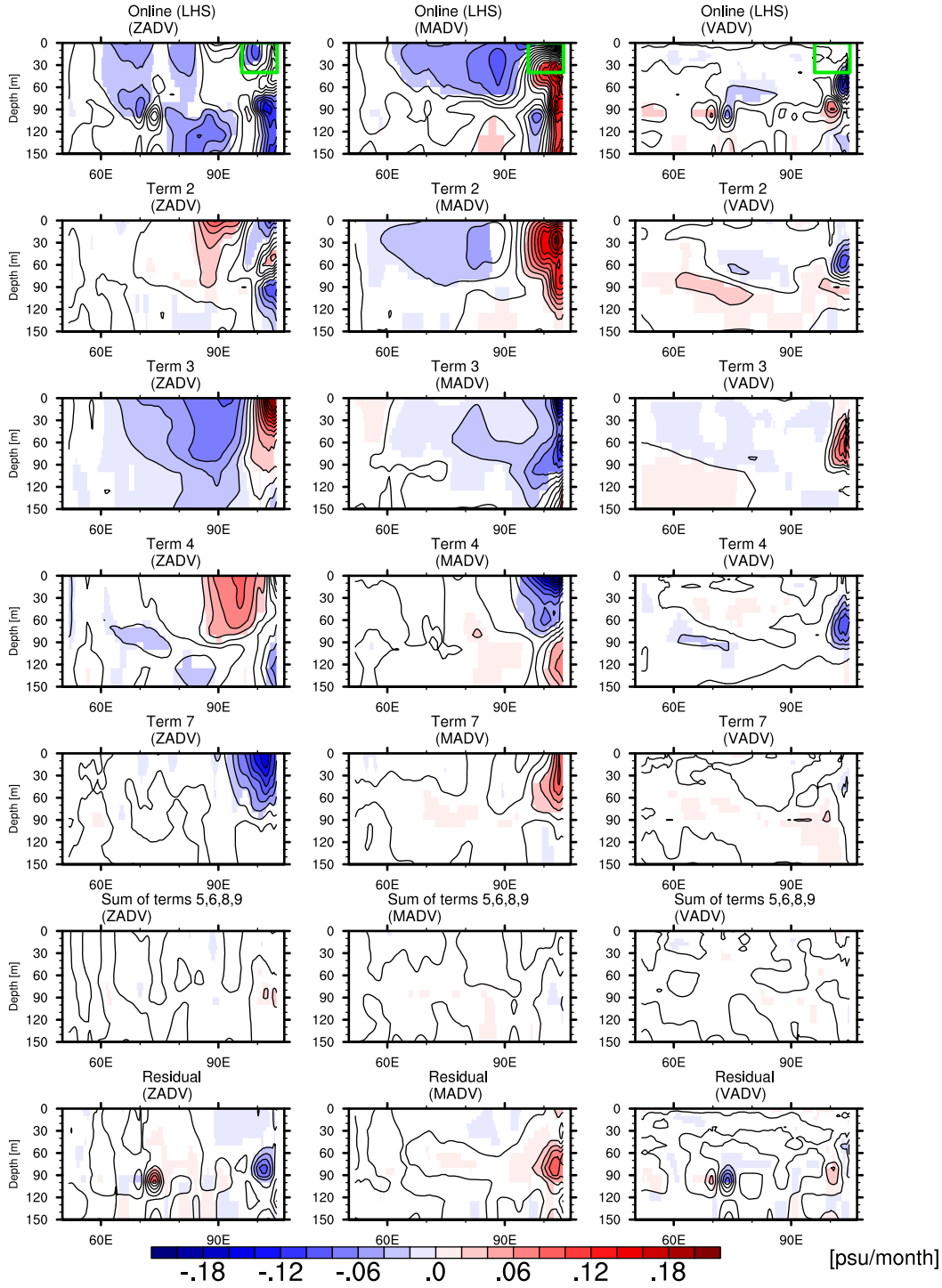

Figure 2.20: As in Fig. 2.17, but for off-equatorial region (meridionally averaged over 8.5°S-4.5°S). The contour intervals are 0.02 [psu/month].

The SEIO is known as a region with vigorous mesoscale eddy activity (Feng & Wijffels, 2002; Z. Yu & Potemra, 2006). Ogata and Masumoto (2010) demonstrated that enhanced baroclinicity during pIOD events in the SEIO leads to stronger eddy activity, and associated increase

of eddy-heat transport in turn affects the evolution of temperature anomalies there. The importance of this IOD-related low-frequency modulation of mesoscale eddy activity is further confirmed by a high-resolution modeling study of Delman et al. (2018). Though our model used in this study is an "eddy-permitting" resolution (with 1/3°×1/3°) and does not completely resolve mesoscale eddies, eddy kinetic energy (EKE) is actually higher in the MR than the NoIOD run, suggesting that eddy activity is stronger during the pIOD (Figs. 2.20a-c). Here, the EKE is calculated as follows:

$$EKE = \frac{1}{2}(u''^2 + v''^2). \tag{2.18}$$

To see the importance of eddy-induced horizontal salinity advection, we present the spatial pattern of Term 9 computed from the MR and the NoIOD run in Fig. 2.21. Over the SEIO, the eddy-induced zonal (meridional) salinity advection contributes to freshening (saltening) near the surface in both MR and NoIOD run (Figs. 2.21d, e, g, h). Since eddy activity is more vigorous in the MR than the NoIOD run, associated eddy-induced horizontal salt advection is also stronger in the MR (Figs. 2.21d-l), and explains negative (positive) zonal (meridional) advection anomalies in the SEIO. Though the low-frequency modulation of eddy activity associated with the IOD and related feedback onto temperature have been discussed by several recent studies (Delman et al., 2018; Ogata & Masumoto, 2010), our results imply for the first time that salinity is also significantly affected by the IOD-related interannual variability of eddy activity.

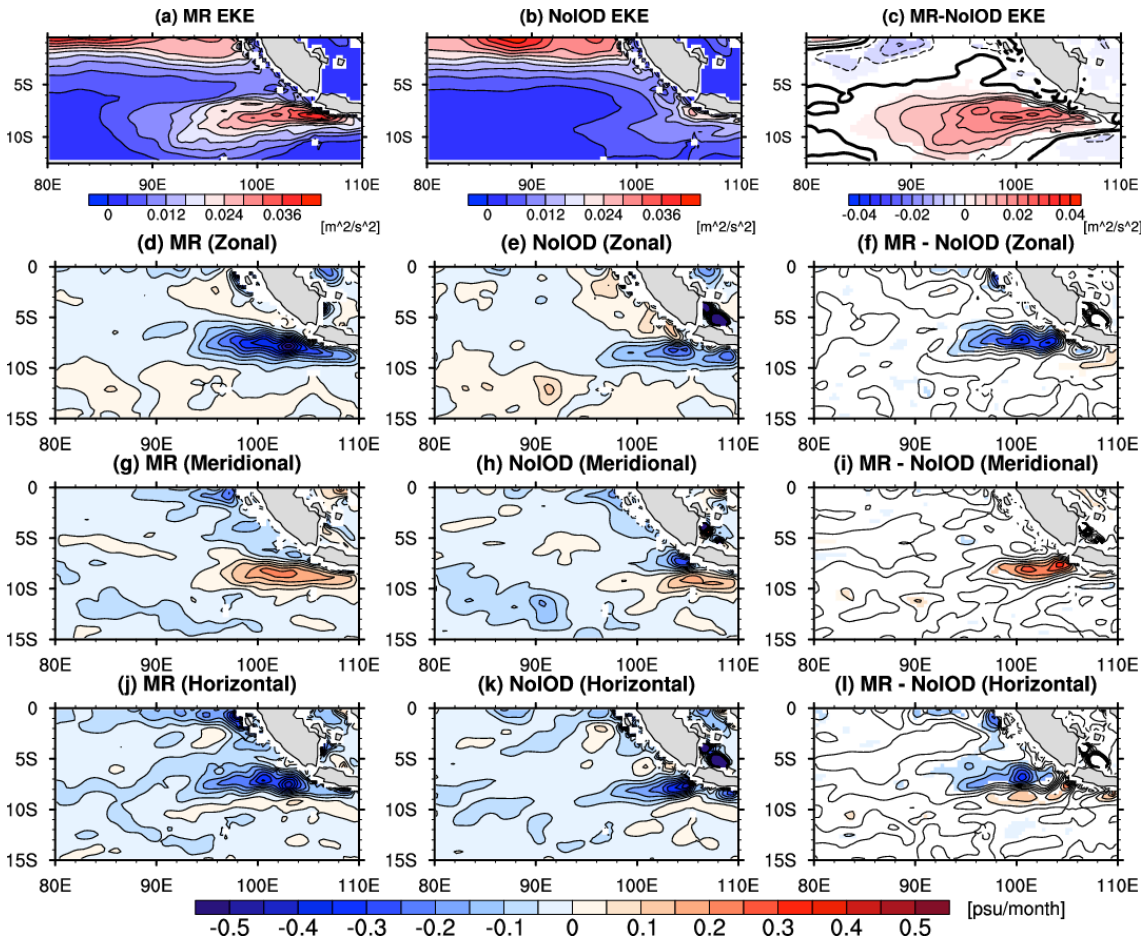

Figure 2.21: (a)-(c): Spatial pattern of the eddy kinetic energy (EKE) (see Eq. (2.18) for definition) during ASO of pIOD events for the (a) MR, (b) NoIOD run, and (c) difference between the MR and NoIOD run (MR-NoIOD) (in [m^2/s^2]). Contour intervals are 0.004 [m^2/s^2]. (d)-(f): As in (a)-(c), but for Term 7 of zonal advection on the right hand side of Eq. (2.18). The contour intervals are 0.05 [psu/month]. (g)-(i): As in (d)-(f), but for meridional advection. (j)-(l): As in (d)-(f), but for horizontal advection (the sum of zonal and meridional advection). Differences significant at the 90% confidence level by a two-tailed t test are shaded in (c), (f), (i), and (l).

2.4.4 Contributions from intraseasonal variability to low-frequency salinity anomalies

In the previous subsection, we have demonstrated that the interaction between intraseasonal variability and low-frequency variability plays an important role in generating positive subsurface salinity anomalies in the EEIO. It was conjectured that the vertical heaving of the pycnocline and associated upward shift of nonlinear meridional salinity advection mediated by intraseasonal MRG waves seem to be the major mechanism behind this phenomena. To substantiate this intriguing hypothesis, we here conduct a set of numerical experiments using the LCSM, which encapsulates the essential physical processes under a simplified framework.

There are two possible pathways that the pIOD modulates the oceanic responses to high-frequency atmospheric variability. The first argument is that the changes in the background oceanic conditions due to the pIOD alter the ocean's sensitivity to the imposed atmospheric anomalies. The other possibility is that the pIOD-related large-scale atmospheric conditions modulate the strength of atmospheric intraseasonal variation, which may directly alter the oceanic responses. Here, we note that such low-frequency modulation in the strength of subseasonal atmospheric variations are *not* explicitly removed in our NoIOD forcings (see section 2.2.3 for details). This is because the low-frequency modulation (with frequency of f_l) in the amplitude of the high-frequency variation (with frequency of f_h) appears at the frequency of $f_h \pm f_l$ (note that $\cos(2\pi f_l t)\cos(2\pi f_h t) = \frac{1}{2}\{\cos(2\pi[f_l + f_h]t) + \cos(2\pi[f_l - f_h]t)\}$) (Stuecker et al., 2013), and it cannot be adequately captured by a simple low-pass filter we have adopted in this study. To discuss the contributions from both effects, we will conduct a set of LCSM experiments and demonstrate that the oceanic change is more essential for the changes in meridional salinity advection anomalies, as hypothesized in the previous subsection.

As mentioned in Section 2.2.4, the inputs of LCSM are wind stress forcing and wind

projection coefficients, which can be derived from the background density stratification. To assess impacts of the background density stratification, we have prepared two sets of wind projection coefficients. First, we have obtained density field using composited temperature and salinity profiles of the MR during SON of pIOD events, and calculated the corresponding wind projection coefficients (denoted as PROJ_MR). The other set of wind projection coefficients, PROJ_NoIOD, are computed from similar composited temperature and salinity profiles taken from NoIOD runs. Since the pIOD-related variations are substantially removed in the NoIOD runs, the differences between the PROJ_MR and PROJ_NoIOD measures the effects of anomalous stratification due to the pIOD. For the wind stress, we have applied the a 10-30 day Lanczos bandpass filter to the original forcing of the JRA55-do, since the spectrum peak of wind fluctuation that preferentially excites MRG waves is found around the biweekly band (Miyama et al., 2006; Sengupta et al., 2004).

To assess the impacts of changes in the background stratification, we have conducted two LCSM experiments using different sets of wind projection coefficients, namely, the PROJ_MR and PROJ_NoIOD, with the bandpass-filtered wind forcing of each pIOD year (i.e. in total, 18 experiments=2 cases × 9 pIOD events are conducted). Each set of LCSM experiment is labeled as LCSM_WSMR_WPMR and LCSM_WSMR_WPNoIOD, respectively. Both sets of experiments start from May 1st of each pIOD year with no motions and are continued until December 31st. We have obtained a 3-day averaged current fields, pressure and density during the integration. Then, using these outputs, the nonlinear density advection (NDA) terms are diagnostically computed as follows:

$$NDA = \underbrace{-u\frac{\partial \rho}{\partial x}}_{Zonal} \underbrace{-v\frac{\partial \rho}{\partial y}}_{Meridonal} \underbrace{-w\frac{\partial \rho}{\partial z}}_{Vertical}. \tag{2.19}$$

Note that the effect of NDA is *not* felt by the LCSM, as the NDA does not appear in the governing

equation of the LCSM (see Eq. (2.5d)). Therefore, the response of NDA to the background stratification can be diagnostically estimated through the LCSM experiments.

Figure 2.22 presents composites of time-averaged (from August to October) NDA and contributions from each component as the depth-longitude sections along the equator. Consistent with previous studies (Nagura et al., 2014; Ogata et al., 2017; Smyth et al., 2015), the cumulative effect of the meridional component of NDA associated with intraseasonal MRG waves is *reduction* of density near the pycnocline (i.e. net heating and freshening) (Figs. 2.22d, e), while its vertical component acts to offset it (Figs. 2.22g, h). A comparison of the two experiments shows that the total NDA of LCSM_WSMR_WPMR in the eastern part of the basin is located closer to the surface than that of LCSM_WSMR_WPNoIOD (Figs. 2.22j, k), corresponding to the upward shift of pycnocline in the former. Consequently, the differences between the two, presented in the right column, exhibit a dipole structure with negative (positive) NDA anomalies above (below) the pycnocline (Figs. 2.22f, i, l), as seen in meridional salinity advection anomalies of the ROMS experiments (Section 2.4.3). Since the only differences between the two experiments are in the background stratification, we can conclude that the pIOD-related changes in density stratification play a critical role in modulating the maximum depth of the NDA associated with MRG waves. The remarkable agreement between the results from ROMS and LCSM experiments provides a compelling evidence that supports the validity of our physical interpretation.

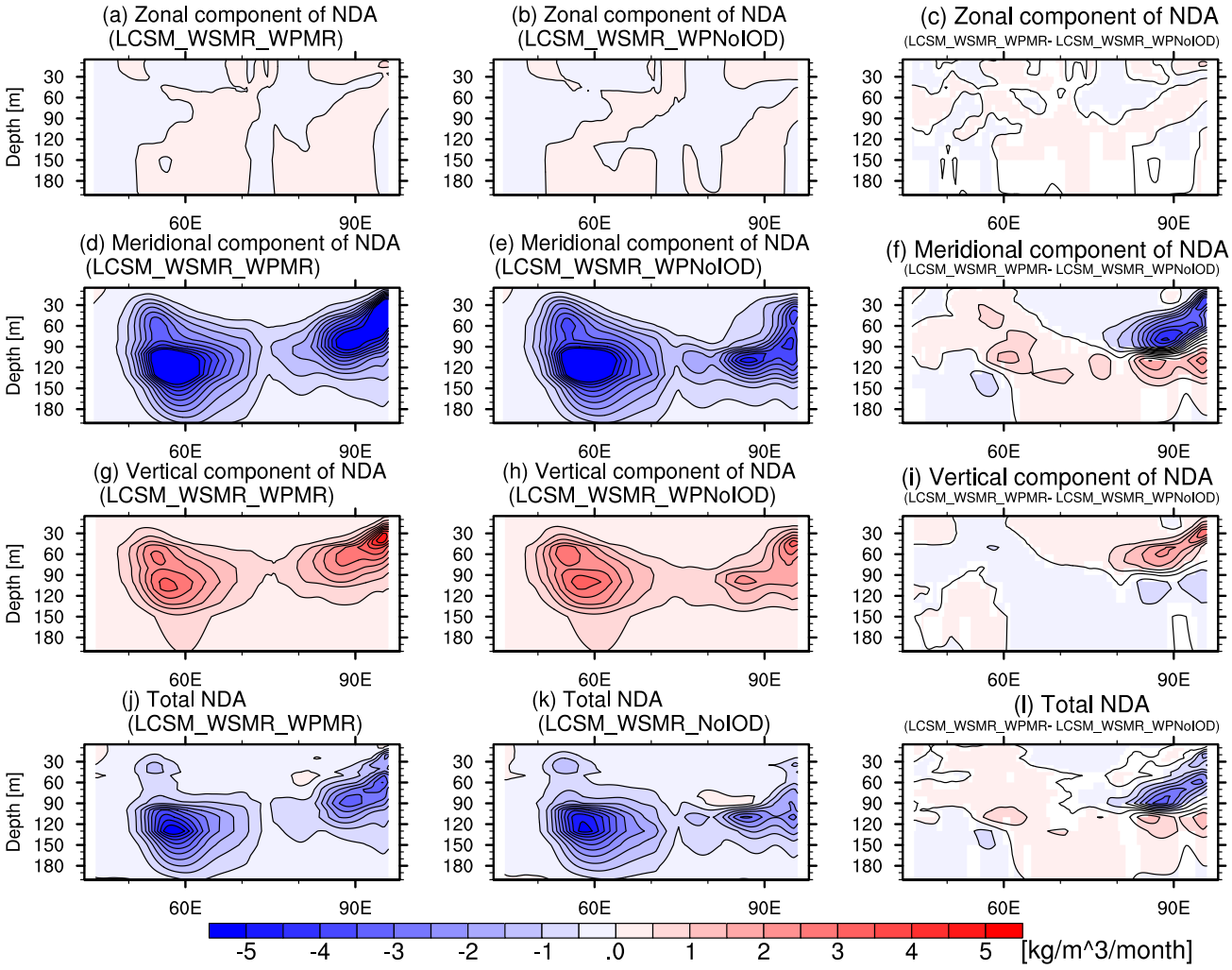

Figure 2.22: Depth-longitude section of the nonlinear density advection (NDA) (j-l) and contribution from zonal (a-c), meridional (d-f), and vertical (g-i) components (see Eq. (2.19)) during ASO of pIOD years along the equator (meridionally averaged over 1.5°S-1.5°N), derived from the linear continuously stratified model (LCSM) experiments (in [kg/m^3/month]). The left (middle) column is from LCSM_WSMR_WPMR (LCSM_WSMR_WPNoIOD), while difference between the two experiments (i.e. LCSM_WSMR_WPMR minus LCSM_WSMR_WPNoIOD) is presented in the right column. The contour intervals are 0.5 [kg/m^3/month], and differences significant at the 90% confidence level with a two-tailed t test are shaded in the right column.

We next assess the second argument, which involves the low-frequency modulation of intraseasonal atmospheric variation. In this regard, Shinoda and Han (2005) have noted that the atmospheric subseasonal variability in the EEIO is significantly weakened during the peak phase of the pIOD. Indeed, we can identify substantial decrease in the strength of intraseasonal wind variability in the EEIO during the pIOD (Fig. 2.23; compare the red and black lines). To assess the impact of these changes in the magnitude of intraseasonal wind fluctuations, we have randomly picked up 9 years excluding pIOD (1964, 1975, 1976, 1985, 1986, 1995, 1999, 2003, 2009) to prepare wind forcing used in another set of LCSM experiments. The standard deviation of meridional wind stress anomalies average over these non-pIOD years (the blue lines of Fig. 2.23) is very similar to that of whole years (the black lines of Fig. 2.23), implying that these years adequately represent situations in the normal years. Based on the above situation, the additional set of experiments, called LCSM_WSNoIOD_WPNoIOD, is integrated in the same manner as other sets of LCSM experiments, with the bandpassed wind stress of these non-pIOD years and wind projection coefficients of PROJ_NoIOD. By taking the differences between the LCSM_WSMR_WPNoIOD and LCSM_WSNoIOD_WPNoIOD, we can isolate impacts of the modulation in the amplitude of wind forcing on the subsurface NDA. Here, we note that our results presented below are not sensitive to the specific choice of these non-pIOD years in a qualitative sense.

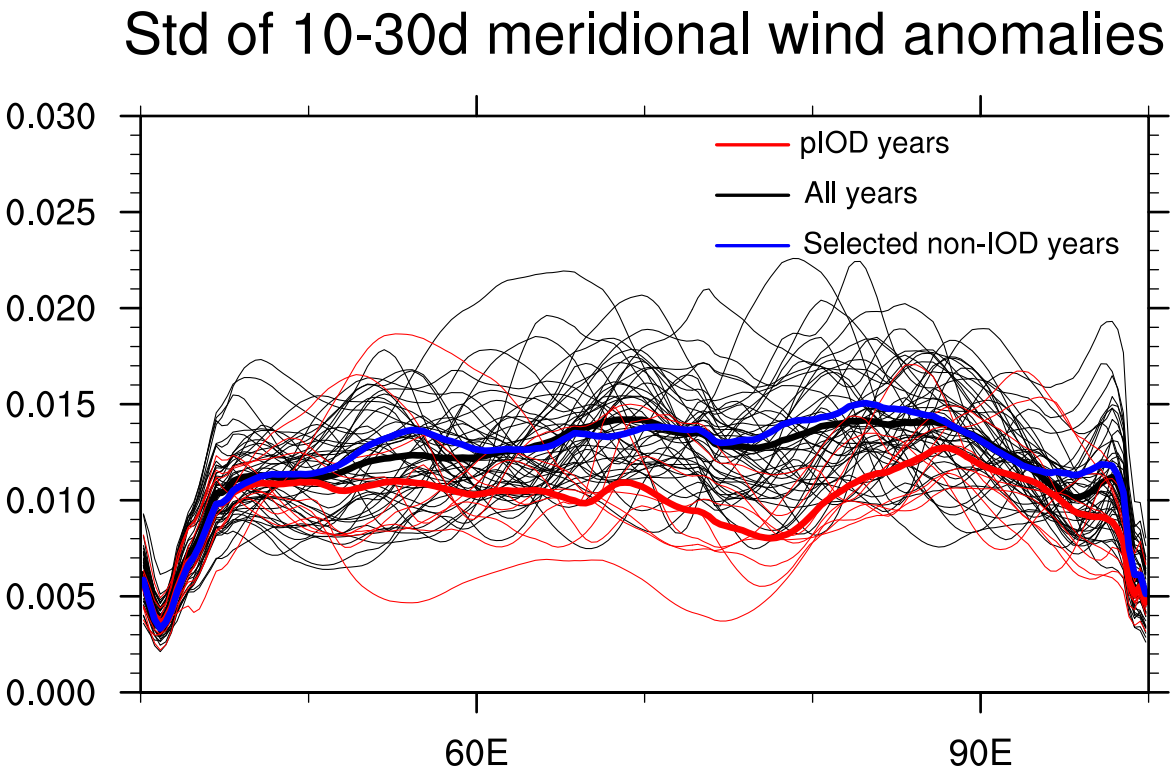

Figure 2.23: Standard deviation of bandpassed (with a 10-30day Lanczos filter) meridional wind stress anomalies (in [N/m^2]) during SON of each year along the equator (meridionally averaged over 1.5°S-1.5°N) derived from the JRA55-do. The thin black (red) lines represent values of non-pIOD (pIOD) years, and thick black (red) line indicates their average. The thick blue line denotes the average of selected non-pIOD years (1964, 1975, 1976, 1985, 1986, 1995, 1999, 2003, and 2009; see the main text) used in the additional LCSM experiments (LCSM_WSNoIOD_WPNoIOD).

The vertical structures of subsurface NDA along the equator from the additional set of experiments are presented in Fig. 2.24. As expected, the magnitude of NDA is weaker in the LCSM_WSMR_WPNoIOD than LCSM_WSNoIOD_WPNoIOD (Figs. 2.24d, e, g, h, j, k), consistent with the fact that the amplitude of corresponding wind forcing is also weaker in the LCSM_WSMR_WPNoIOD (Fig. 2.23). However, there are no notable changes in the vertical

structures of the NDA between the two experiments (Figs. 2.24f, i, l), in stark contrast with the significant differences detected in Fig. 2.22 (right column). These results suggest that the changes in the amplitude of subseasonal wind variations due to the pIOD seem not to be the dominant factor explaining the upward shift of the NDA, and the positive salinity anomalies below the pycnocline, though they partly affect the amplitude of NDA.

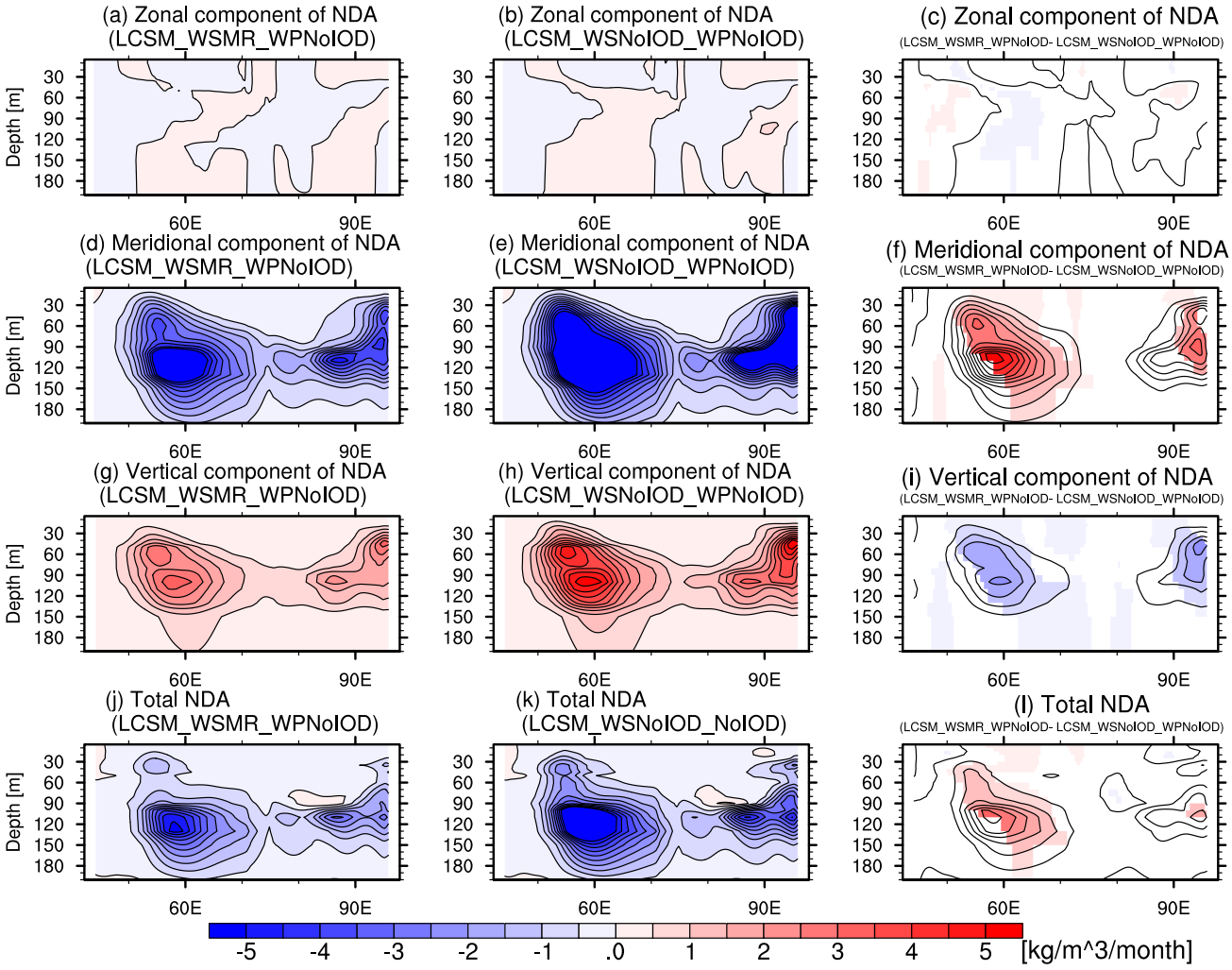

Figure 2.24: As in Fig. 2.22, but for LCSM_WSMR_WPNoIOD (left column) and LCSM_WSNoIOD_WPNoIOD (middle column).

2.5 Summary and discussions

In this chapter, we have investigated surface and subsurface salinity anomalies during the pIOD through analysis of observational datasets and numerical experiments using a regional ocean model, and their results are summarized in Fig. 2.25.

First, we have examined the features of the upper ocean salinity variations associated with the pIOD by analyzing the observational datasets and ocean reanalysis. During the pIOD, significant surface freshening is observed in the central-eastern equatorial IO, while southeastern tropical IO experiences anomalous saltening near the surface, as already reported by several previous studies. In addition to the SSS, prominent anomalies are also found in the subsurface salinity, with anomalous saltening (freshening) in the eastern equatorial IO (southern tropical IO). We also examined the links of those salinity variations with large-scale climate modes, and found that the IOD, rather than the ENSO, is the dominant driver.

The hindcast simulation forced by realistic 3-hourly atmospheric reanalysis data, daily river runoff, and monthly boundary forcing successfully captures many pronounced signatures associated with the pIOD, including temperature, salinity, and velocity anomalies in the upper ocean. Thus, it is possible to carry out in-depth investigation of their origin.

To isolate the processes responsible for the generation of salinity anomalies, we have performed a series of sensitivity experiments by separately imposing anomalous atmospheric and lateral boundary forcing to the model. For SSS, anomalous freshening in the central-eastern equatorial IO is mainly controlled by the wind-stress effect, while significant saltening over the SEIO is caused by the wind-speed and precipitation effects. On the other hand, the subsurface salinity anomalies are almost entirely dominated by the wind-stress effect, suggesting that wind-driven dynamical processes are instrumental to the generation of these subsurface anomalies.

In addition to sensitivity experiments mentioned above, we have conducted an online salinity budget analysis and decomposed advective anomalies for more detailed analyses. Our results have shown that changes in the upper ocean currents (both horizontal and vertical) induced by pIOD-related wind stress anomalies through linear wave adjustments and resulting modulation of salinity advection are the primary driver of observed surface and subsurface salinity anomalies. Therefore, mechanisms that have already been proposed by previous literatures based on offline analyses (Y. Zhang et al. 2013; J. Li et al. 2016) are qualitatively consistent with our results, to a first approximation. Yet, some processes that have been overlooked are also found to be important in the present study, thanks to the use of an online salinity budget analysis that closes exactly. These processes are related to the interaction between high-frequency intraseasonal variation and low-frequency modulation of background state, and are particularly substantial in the EEIO near the pycnocline and the SEIO near the surface. In the EEIO, uplifting of pycnocline associated with the pIOD causes upward shift of "net freshening region" due to nonlinear meridional salinity advection, which is mediated by mixed-Rossby gravity waves. This leads to the anomalous freshening (saltening) above (below) the pycnocline and partly alters the vertical structures of positive subsurface salinity anomalies there. The validity of the above idea has been further confirmed by an additional set of sensitivity experiments using the LCSM. On the other hand, intensification of mesoscale eddy activity in the SEIO gives rise to the increase of salinity advection by mesoscale eddies, and eventually modulates the SSS anomalies there.

An interesting but challenging question that should be addressed at the next step is how salinity anomalies affect the upper ocean structure and SST. Recent studies have demonstrated that changes in stratification and density fields associated with salinity anomalies significantly affect upper ocean temperature and circulation (J. Li et al., 2018; Masson et al., 2004; Y. Zhang et al.,

2016). However, these studies are not designed to isolate the collective role played by the pIOD-related salinity anomalies, and more comprehensive assessments are required to clarify this issue. Since the present model has succeeded in capturing the observed salinity anomalies associated with the IOD, it can serve as a powerful tool for investigating these issues. Detailed analyses of carefully designed sensitivity experiments using this model will be presented in the next chapter.

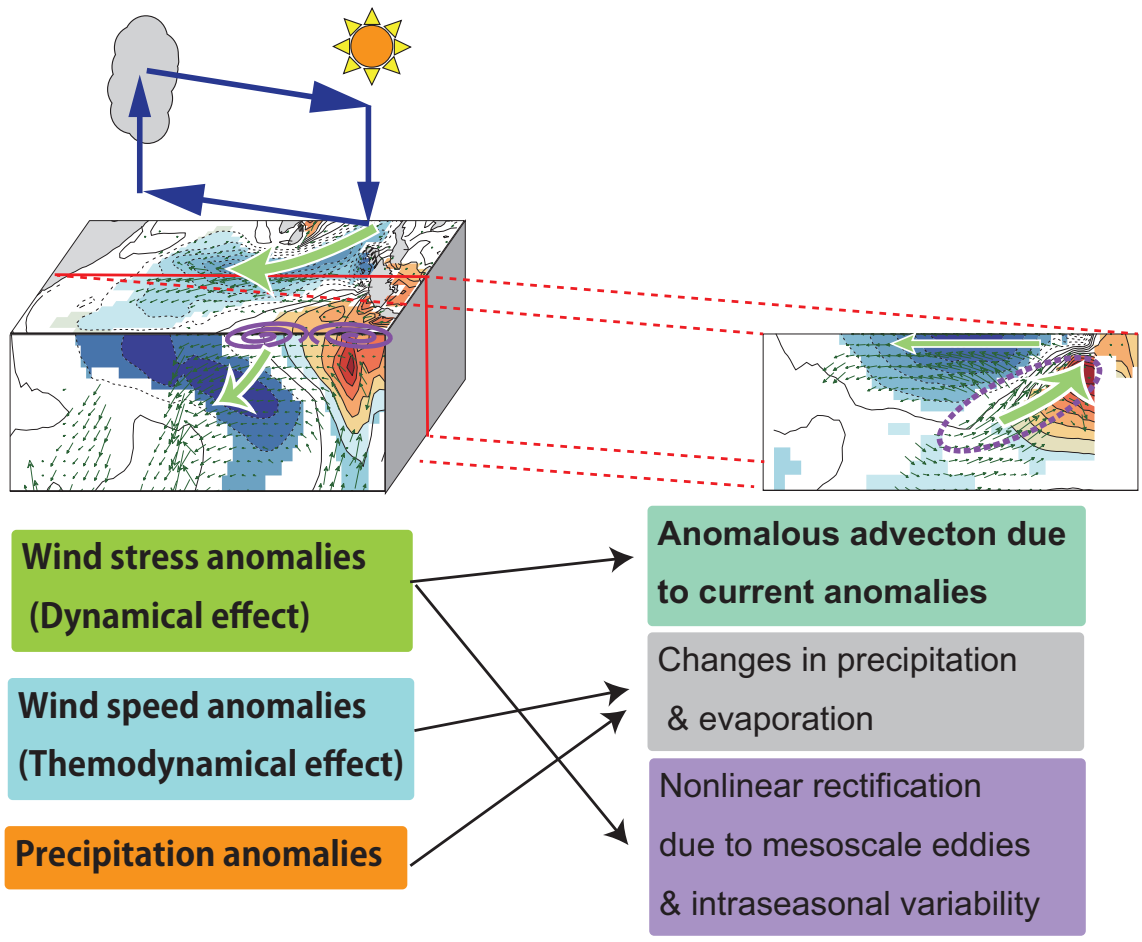

Figure 3.18: Schematic diagram illustrating how atmospheric anomalies generates the upper ocean salinity anomalies during the pIOD. See the main text for details.

Chapter 3

Impacts of salinity anomalies associated with the positive IOD on the upper ocean temperature and circulation

This chapter has been published as:

1. Kido, S., & Tozuka, T. (2017). "Salinity variability associated with the positive Indian Ocean Dipole and its impact on the upper ocean temperature", *Journal of Climate*, 30, 7885-7907, doi: https://doi.org/10.1175/JCLI-D-17-0133.1

2. Kido, S., Tozuka, T., & Han, W. (2019). Experimental assessments on impacts of salinity anomalies on the positive Indian Ocean Dipole. Journal of Geophysical Research: Oceans, 124, doi: https://doi.org/10.1029/2019JC015479

3.1 Introduction

In the previous chapter, we have quantitatively discussed the feature and generation mechanisms of surface and subsurface salinity anomalies found in the tropical Indian Ocean (IO) during positive Indian Ocean Dipole (pIOD) events, through analysis of observational datasets and various experiments using a regional ocean model and a linear continuously stratified model (LCSM). It was shown that anomalous currents in response to large-scale wind stress anomalies are the dominant drivers of these surface and subsurface salinity anomalies associated with the pIOD, though the modulation of nonlinear salinity advection due to high-frequency variability also plays an important role in some regions.

Several previous studies have tried to estimate how salinity affects the evolution of the IOD. First, Masson et al. (2004) have compared hindcast simulations of the 1997 pIOD event with and without dependence of the vertical mixing coefficient on salinity stratification in their ocean general circulation model (OGCM), and found that salinity stratification and associated barrier layer act to enhance the sea surface temperature (SST) cooling in the eastern equatorial Indian Ocean (EEIO). However, as in many previous works on the role of barrier layer, “the effects of salinity” they called, include contributions from mean salinity stratification and those from its variability. Also, as their study only focused on a specific pIOD event, it is not clear whether the features they have detected are common to all pIOD events. Given that three-dimensional processes, such as horizontal and vertical advection of temperature, play a crucial role in the evolution of SST anomalies associated with the pIOD (Halkides & Lee, 2009; T. Li et al., 2002; Raghu Murtugudde et al., 2000), it is important to consider the specific impacts of salinity anomalies on these processes. In this regard, J. Li et al. (2018) have shown that the pIOD-related salinity anomalies and associated zonal density gradient accelerate the Equatorial Undercurrent (EUC) through sensitivity experiments

using a regional ocean model. However, as both temperature and salinity are nudged to prescribed values in their experiments, it was difficult to discuss their impacts on SST.

The above situation leads us to expand their work using a regional ocean model that has complete governing equations and can well simulate the observed pIOD events. The goal of this chapter is to quantify impacts of the pIOD-related salinity anomalies on the upper ocean circulation and temperature, and to understand the processes behind them. To this end, we have carried out sensitivity experiments with a novel strategy that can isolate the effects of pIOD-associated salinity anomalies. The focus here is again on pIOD events, because the pIOD is generally stronger than the negative IOD, whose salinity anomalies are close to a mirror image of those during pIOD, with slightly smaller amplitude. The rest of this chapter is organized as follows. Section 3.2 describes the methods of our data analysis and the design of sensitivity experiments. A brief summary of the regional ocean model used in this study is also presented. Section 3.3 discusses several direct and indirect observational evidences showing the impacts of pIOD-related salinity anomalies on the upper ocean stratification and SST. Section 3.4 presents the results from the sensitivity experiments, and compares various oceanic parameters between experiments, and section 3.5 investigates the physical processes responsible for the differences between the control and sensitivity experiments through heat and zonal momentum budget analyses, together with additional experiments using the LCSM. Finally, section 3.6 provides a summary and discussion.

3.2 Analysis method and designs of model experiments

3.2.1 Decomposition of density anomalies

Although the density of the seawater (ρ) is a nonlinear function of temperature (T), salinity (S), and pressure, nonlinearity in the equation of state and the thermobaric effect (density dependence on pressure) is negligible within a typical parameter range in the tropical upper ocean.

Therefore, density anomalies can be decomposed into contribution from temperature and salinity anomalies. More specifically, we first compute the total density ($\rho(T,S)$) based on the interannual temperature and salinity profile using the UNESCO version of the equation of state. Then, we calculate the density by replacing interannual salinity with climatological salinity ($\rho(T,S_{clim})$). The difference between two density, $\Delta\rho_S$ $(=\rho(T,S)-\rho(T,S_{clim}))$, is the impact of interannual salinity anomalies on density anomaly. Contribution from temperature anomalies to density anomalies ($\Delta\rho_T$) can be estimated in a similar manner ($\Delta\rho_T=\rho(T,S)-\rho(T_{clim},S)$). Because of linearity, $\Delta\rho$ can be approximated by the sum of $\Delta\rho_S$ and $\Delta\rho_T$. In this way, we can quantify relative importance of temperature and salinity anomalies in generating density anomalies by comparing $\Delta\rho_T$ and $\Delta\rho_S$ with $\Delta\rho$. This method was proposed by Zheng and Zhang (2012), who applied it to the tropical Pacific Ocean, but it has never been applied to the tropical Indian Ocean. Here, we focus on the squared buoyancy frequency, which is a measure of the vertical stability of water column and a key parameter for describing the upper ocean dynamics and thermodynamics (F. Zheng et al., 2014; F. Zheng & Zhang, 2012, 2015). Unless otherwise specified, we call the outputs from the ORAS4 product (Balmaseda et al., 2013) as the observational dataset in the following discussions (see section 2.2.1 for more discussions).

3.2.2 Detection of salinity impacts on the SST evolution

Even though detection of impacts of salinity on the evolution of other oceanic variables is not an easy task, here we have attempted to extract their imprints onto the SST evolution using several conventional statistical methods, taking the relationship between the evolution of salinity and SST into account. First, we assume that the processes governing the evolution of SST anomalies can be separated into three components, namely,

$$\frac{\partial T'}{\partial t} = -\alpha T' + (S' - related\ processes) + (Res.), \tag{3.1}$$

where T' and S' represent temperature and salinity anomalies respectively. The first term of Eq. (3.1) is a Newtonian damping (e.g. the thermal damping due to air-sea coupling) and second (third) term represents processes influenced by (independent of) salinity anomalies. Though the validity of the above assumption is difficult to justify in a rigorous manner, its simplicity is useful for an intuitive and conceptual understanding of the roles played by salinity anomalies.

The simplest way to extract the salinity-induced signal is to calculate the regression coefficients of time derivative of SST anomalies (i.e. $\frac{\partial T\prime}{\partial t}$) against local salinity anomalies (i.e. S'). If enhanced salinity stratification causes weakening of vertical mixing and SST warming, as often postulated in many studies on the barrier layer (e.g. Cronin & McPhaden, 2002; Qiu et al., 2012), negative (positive) correlation/regression between surface (subsurface) salinity and $\frac{\partial T\prime}{\partial t}$ are expected. To verify whether these arguments hold true, we calculate the regression coefficients of surface and subsurface salinity anomalies against $\frac{\partial T\prime}{\partial t}$ at each grid point and depth level, after removing the Newtonian damping term (the first term on the right hand side of Eq. (3.1)) from $\frac{\partial T\prime}{\partial t}$ by a partial regression between $\frac{\partial T\prime}{\partial t}$ and T'. Hereafter, subsurface salinity is defined as the vertically averaged salinity from 50 to 100 [m] depth, based on the results from Chapter 2.

Since salinity anomalies can alter the three-dimensional upper ocean circulation and associated heat transport (see section 1.3 for more detailed discussions), their impacts on the SST evolution may not be local. To account for such nonlocal responses, we apply the singular value decomposition (SVD) method to investigate covariation between salinity anomalies and $\frac{\partial T\prime}{\partial t}$ (Bretherton et al., 1992; Czaja & Frankignoul, 2002). As in the regression analysis, the Newtonian

damping term has been first removed from $\frac{\partial T'}{\partial t}$ by a linear regression against T'. Then, we have prepared the data matrix of $\frac{\partial T'}{\partial t}$ and salinity anomalies (represented as $\boldsymbol{A}$ and $\boldsymbol{B}$, respectively), and applied a spatial weighting and temporal normalization so that the value at each grid point has a equal weight per area and unit variance. If we denote the number of grid point as K and the length of data as M, $\boldsymbol{A}$ is a matrix with a dimension of $M \times K$, whereas $\boldsymbol{B}$ has a dimension of $M \times 2K$, since surface and subsurface salinity anomalies are lumped together for the spatial direction. After these procedures, we have constructed the correlation matrix $\boldsymbol{C} = \boldsymbol{A^t B}$ (t denotes matrix transpose) and performed the SVD analysis. After the SVD analysis, the left singular vector $\boldsymbol{U}$, the right singular vector $\boldsymbol{V}$, and the singular value (diagonal) matrix $\boldsymbol{D}$ are obtained, and they satisfy $\boldsymbol{C} = \boldsymbol{UDV^t}$. Using these outputs, the time expansion coefficients of each field for m-th mode, $\boldsymbol{T_A^m(t)}$ and $\boldsymbol{T_B^m(t)}$ are calculated by projecting the corresponding singular vectors onto the original data matrix, as $\boldsymbol{T_A^m = AU^m}$ and $\boldsymbol{T_B^m = BV^m}$. The results from the SVD analysis are presented as the heterogeneous regression map, namely, the regression coefficients of $\boldsymbol{A}$ and $\boldsymbol{B}$ against $\boldsymbol{T_B}$ and $\boldsymbol{T_A}$, respectively.

3.2.3 ROMS setting

For self-consistency of this chapter, here we provide a brief description of the regional ocean model used for the sensitivity experiments, though its detail has already been given in section 2.2.2. The Regional Ocean Model System (ROMS) (Shchepetkin & McWilliams, 2005) is used to assess impacts of pIOD-related salinity anomalies on the upper ocean temperature and currents. The model domain is the tropical IO (30°-110°E, 46°S-32°N) with a horizontal resolution of 1/3°×1/3° and 40 sigma layers in the vertical direction. The model is forced by 3-hourly atmospheric forcing and daily river runoff from the JRA55-do (Suzuki et al., 2018; Tsujino et al., 2018), as well as lateral

boundary forcing from the Ocean Reanalysis System version 4 (ORAS4) reanalysis product (Balmaseda et al., 2013). The turbulent (latent and sensible) heat fluxes and evaporation are calculated using the Coupled Ocean-Atmosphere Response Experiment (COARE) 3.0 algorithm (Fairall et al., 2003) based on sea level pressure, surface (10 m) temperature/humidity, wind speed and the modeled SST. After 30-yr spin up under the climatological forcing, the model is integrated forward from 1958 to 2015. This run, dubbed as the main run (MR) in section 2.2.3, is renamed as the "control main run" (CTL_MR) in this chapter. All outputs from the model, including heat, salt and momentum budget terms (details will be described in section 3.4), are archived as 3-day averaged data and then converted to monthly data to facilitate analysis. As demonstrated in section 2.3.2, this model has a good skill in reproducing the observed variability of the upper ocean fields (e.g. temperature, salinity, and currents), though the amplitude of the IOD-related anomalies simulated in the model is slightly larger than the observation.

3.2.4 Design of sensitivity experiments using the ROMS

Though we have explained our approaches to isolate impacts of salinity anomalies from the observational datasets in section 3.2.2, they do not necessarily provide direct evidences demonstrating the salinity forcing of the upper ocean. For this reason, we have decided to rely on numerical experiments using the regional ocean model.

As mentioned in section 1.3, isolating impacts of salinity anomalies is not straightforward, even for OGCMs. One possible approach is to nudge the modeled salinity toward the climatology and remove the pIOD-related salinity anomalies. This approach would successfully suppress interannual variability of salinity associated with the pIOD, but it also artificially damps signals associated with mesoscale eddies and intraseasonal variability of the currents. Thus, the differences

between the MR and "salinity-nudging run" are not necessarily caused only by the pIOD-related salinity anomalies, as intraseasonal salinity anomalies can rectify onto interannual variability (section 2.4.3). Additionally, application of salinity nudging over the entire water column may lead to artificial density inversion and convection. Indeed, spurious SST cooling is observed over regions with weak stratification when we strongly restore the modeled salinity toward a prescribed value for the whole depth. These signals gradually contaminate the field and degrade the fidelity of the experiment. For this reason, we have decided to adopt a different method, which is based on careful consideration of the generation mechanisms of the pIOD-related salinity anomalies.

First, we have selected 9 pIOD years (1961, 1963, 1972, 1977, 1982, 1987, 1994, 1997, and 2006) as in Chapter 2. The outputs from the CTL_MR for individual pIOD years are used as a baseline, since the "CTL_MR" is forced with realistic atmospheric forcing during the pIOD (Section 2.1). Another experiment, referred to as the "CTL_NoIOD" experiments, is performed with atmospheric forcing excluding the pIOD-related anomalies ("NoIOD forcing"). Note that the river runoff and lateral boundary forcing are identical to those used in the CTL_MR. The "NoIOD forcing" is obtained by applying 120-day low-pass filter to the original atmospheric forcing, and the detailed procedures are described in section 2.2.3. The difference between these two runs (i.e. CTL_MR minus CTL_NoIOD), referred to as Diff_CTL, isolates the collective impact of pIOD-related atmospheric anomalies.

To assess the effect of the pIOD-related salinity anomalies, we have removed the advective terms in the model salinity equation in the above two experiments, and the two new experiments are named as "NoSADV_MR" and "NoSADV_NoIOD". This is realized by deleting the salinity advection terms (both horizontal and vertical) from the source code of the ROMS. The difference between NoSADV_MR and NoSADV_NoIOD, referred to "Diff_NoSADV", measures the impacts

of pIOD-related atmospheric anomalies *without* any influences from salinity anomalies due to advection. Since a large fraction of the pIOD-related salinity anomalies is generated by advective processes (J. Li et al., 2016; Y. Zhang et al., 2013; section 2.4.2), salinity anomalies in Diff_NoSADV are expected to be considerably smaller than those in Diff_CTL, and the validity of this speculation will be carefully assessed below. Therefore, by taking the difference between Diff_CTL and Diff_NoSADV, we can infer the impacts of pIOD-related salinity anomalies. The detailed design of sensitivity experiments described above is summarized in Table 1.

To confirm the validity of our experimental strategy, we have carried out another set of sensitivity experiments, referred to the "prescribed salinity advection (PSADV) experiment". In the PSADV experiments, the model is forced by the same atmospheric and boundary forcing as the CTL_MR, but salinity advection terms (again, both horizontal and vertical) are not explicitly calculated and values taken from other experiments (archived as 3-day averaged values; see section 2.1) are used instead. More specifically, the values of salinity advection terms obtained from CTL_MR are used in the "PSADV_MR" experiment, while those from CTL_NoIOD are adopted in the "PSADV_NoIOD" experiment. Since the only difference between PSADV_MR and PSADV_NoIOD is in the prescribed values of salinity advection term, we can estimate the impact of pIOD-related salinity advection anomalies by taking the differences between them (i.e. PSADV_MR minus PSAV_NoIOD), analogously to those between Diff_CTL and Diff_NoSADV. Compared to the NoSADV experiments, the PSADV experiments make less drastic modifications on salinity equation, but the use of 3-day averaged values in those experiments may artificially smooth out high-frequency variations, which play an important role in the generation of low-frequency salinity anomalies through nonlinear rectification (section 2.4.3). Given that both NoSADV and PSADV experiments have their advantage and drawback, comparison of results from both experiments will

be instructive to gain a more robust understanding concerning the upper ocean response to the pIOD-related salinity anomalies.

Table 1: Summary of ROMS sensitivity experiments

Experiments	Atmospheric forcing	Salinity equation	Process Description
CTL_MR	3 hourly forcing	Complete	Complete solution
CTL_NoIOD	No IOD forcing	Complete	Without the processes driven by IOD-related forcing
NoSADV_MR	3 hourly forcing	No horizontal and vertical salinity advection	Full forcing but with no salinity advection
NoSADV_NoIOD	No IOD forcing	No horizontal and vertical salinity advection	Without IOD-related forcing & no salinity advection
PSADV_MR	3 hourly forcing	Overwrite salinity advection terms using those derived from CTL_MR experiment	Close to the complete solution, but high-frequency variation in salinity advection is partly suppressed.
PSADV_NoIOD	3 hourly forcing	Overwrite salinity advection terms using those derived from CTL_NoIOD experiment	Without influences from pIOD-related variation.
Diff_CTL (=CTL_MR-CTL_NoIOD)			Isolate the effects of total pIOD forcing
Diff_NoSADV (=NoSADV_MR-NoSADV_NoIOD)			Isolate the effects of total pIOD forcing in absence of salinity anomalies due to advection

3.3 Demonstrations of salinity impacts from observational data analysis

In this section, we first discuss impacts of the pIOD-related salinity anomalies on the upper ocean stratification in section 3.3.1. Subsequently, we explore their potential influences on the SST evolution in section 3.3.2 using the statistical techniques described in section 3.2.2.

3.3.1 Assessments of impacts of salinity anomalies on the upper ocean stratification

To examine the relative importance of temperature and salinity anomalies on the density and stratification of the upper ocean, composites of these anomalies during September-November (SON) of pIOD events are constructed from the ORAS4, and depicted as longitude-depth section along the equator (Figs. 3.1a, b). As already seen in Fig. 2.7, there is strong cooling (weak warming) near the thermocline in the east (west). These temperature anomalies are manifestation of the vertical heaving of thermocline associated with the pIOD (S. A. Rao et al., 2002; S. A. Rao & Behera, 2005). For salinity, there are prominent surface freshening in the central-eastern part and subsurface saltening in the east, as depicted in Fig. 2.8. By converting these anomalies into density anomalies, their contribution to density anomalies is estimated (Figs. 3.1c-e). We can identify a dipole structure in density anomalies, with a positive (negative) peak near the pycnocline (surface) in the eastern (western) part (Fig. 3.1e). If we neglect salinity anomalies when calculating density anomalies, the positive peak in the east is underestimated and the negative peak in the central part diminishes (Fig. 3.1c). On the other hand, the density anomalies purely originating from salinity variations (Fig. 3.1d) resemble total density anomalies, but their amplitude is weaker than total density anomalies, especially in the east. These results suggest that both temperature and salinity anomalies play important roles in modulating the density structure over this region. The salinity contribution is especially large in the central-eastern equatorial Indian Ocean, where significant salinity variations are observed.

To assess the impacts of these density anomalies on the upper ocean stratification, we take their vertical derivative to convert to squared buoyancy frequency anomalies (Figs. 3.1f-h). In the eastern part, the combination of negative density anomalies near the surface and positive density anomalies near the pycnocline leads to significant increase in density gradient and vertical stability (Fig. 3.1h). Comparing the amplitude of temperature and salinity contribution, we find that salinity-related anomalies have comparable or even larger magnitude. Qualitatively similar results are obtained even if we construct analogous composites and apply the same decomposition methods using the outputs of ROMS (CTL_MR), as well as other ocean reanalysis products.

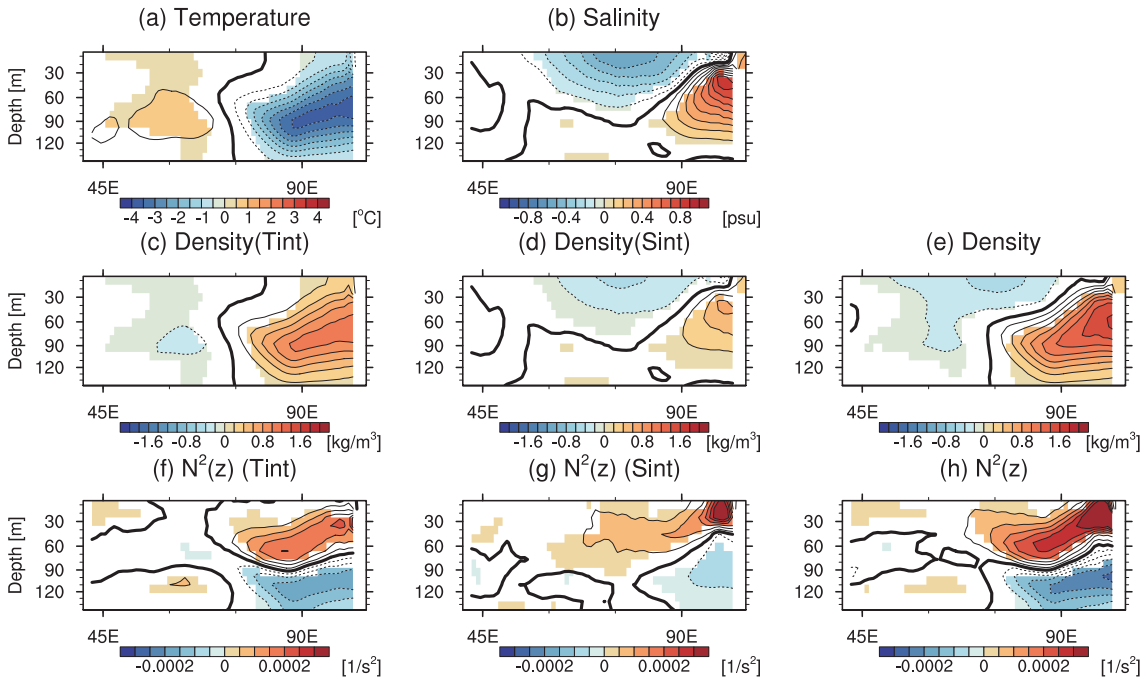

Figure 3.1: (a), (b) Depth-longitude section of composited (a) temperature (in °C: The contour intervals are 0.5 °C) and (b) salinity anomalies (in psu: The contour intervals are 0.1 psu) during SON of the pIOD along the equator (averaged over 2°S-2°N). Note that these composites are constructed from the ORAS4 data. (c)-(e) As in (a), (b), but for (e) density anomalies and contribution from (c) temperature and (d) salinity anomalies

(in kg m^{-3}: The contour intervals are 0.2 kg m^{-3}). (f)-(h) As in (c) – (e), but for the squared buoyancy frequency anomalies (in s^{-2} :The contour intervals are 5×10^{-5} s^{-2}). Anomalies significant at the 90% confidence level by a two-tailed t-test are shaded.

When similar analyses are conducted for the off-equatorial region (Fig. 3.2), a zonal dipole structure in temperature anomalies is found near the thermocline (Fig. 3.2a). Anomalous warming in the west are related to downwelling signals induced by anomalous wind stress curl, whereas significant cooling in the east may be associated with coastal upwelling and/or upwelling Rossby waves reflected from the eastern boundary (S. A. Rao et al., 2002; Shinoda et al., 2004). Surface saltening (subsurface freshening) in the east (west) are evident from the salinity composite (Fig. 3.2b), again consistent with Fig. 2.7.

Reflecting temperature and salinity anomalies, total density anomalies in the off-equatorial region (Fig. 3.2e) have a dipole structure with the opposite signs compared to those of the equatorial section. They are primarily dominated by contribution from temperature anomalies (Fig. 3.2c), but the salinity contribution has non-negligible amplitude and amplifies the signals (Fig. 3.2d).

A composite of squared buoyancy frequency anomalies (Fig. 3.2h) reveals zonally elongated negative anomalies in the central-eastern part, indicating destabilization of the upper water column. These anomalies are explained by positive density anomalies near the surface and negative anomalies below the pycnocline. Again, the contribution from temperature anomalies prevails over that of salinity anomalies (Figs. 3.2f, g). However, especially in the central-eastern region, weakening of salinity stratification plays an important role in determining the structure of total anomalies.

In summary, the salinity stratification in the central-eastern equatorial Indian Ocean is

strengthened due to the negative (positive) salinity anomalies near the surface (subsurface). On the other hand, subsurface freshening and surface saltening in the SEIO lead to a decrease in the vertical gradient of density and destabilization of the upper ocean. In both regions, the changes in salinity stratification are comparable in magnitude to those in temperature stratification in terms of contribution to density stratification. These results suggest that the IOD-related salinity anomalies have significant influences on the stability of the upper ocean and they have potential to modulate the strength of the vertical mixing and evolution of temperature and currents.

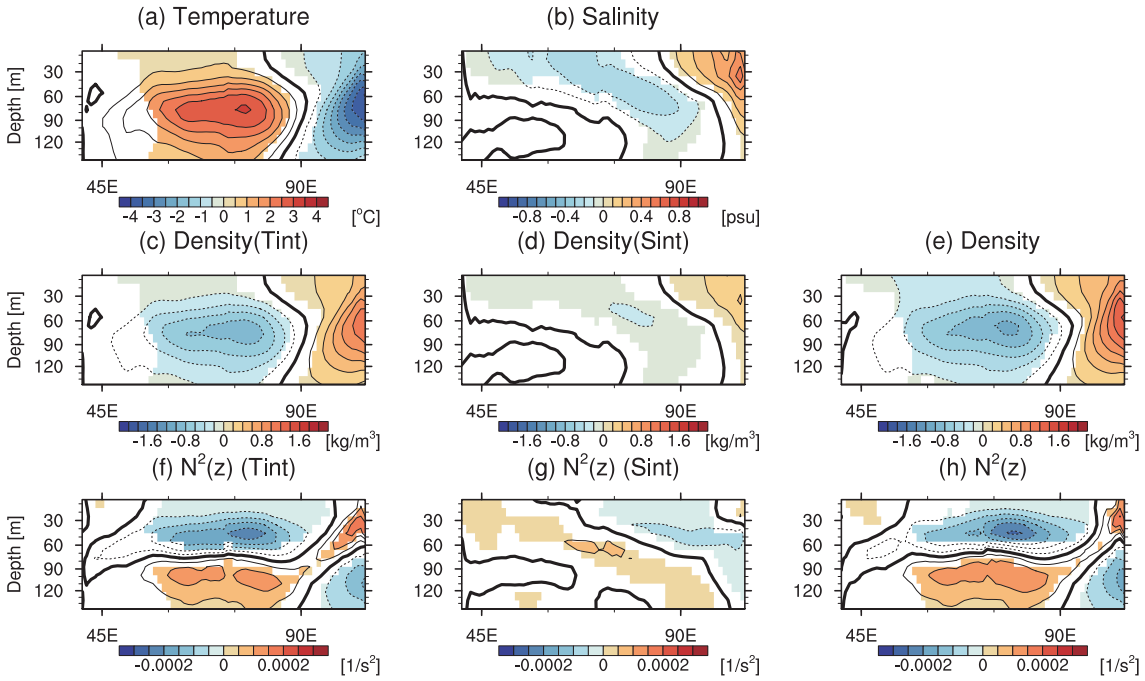

Figure 3.2: As in Fig. 3.1, but for the off-equatorial region (averaged over 8°S-4°S).

3.3.2 Statistical estimation of salinity impacts on the SST evolution

As noted in section 3.2.2, a simple way to verify the local impacts of salinity stratification on SST is to compute the regression coefficients of time derivative of SST ($\frac{\partial T}{\partial t}$) against surface and subsurface salinity anomalies at each grid point. Here, we calculated the regression coefficients of

the October-December (OND) averaged SST tendency ($\frac{\partial T}{\partial t}$) against the SON-averaged salinity anomalies, considering the seasonality of the IOD and temporal lag between $\frac{\partial T}{\partial t}$ and salinity anomalies (assuming that salinity anomalies leads $\frac{\partial T}{\partial t}$ about a month). Qualitatively similar results are obtained even if we change the season and time lag within a realistic range. Figure 3.3 reveals that significant negative (positive) regression coefficients between $\frac{\partial T}{\partial t}$ and surface (subsurface) salinity anomalies are only seen in the central-eastern tropical IO. These regions with a significant regression are roughly collocated with those with significant changes in salinity stratification during the pIOD (Fig. 3.1). These results imply that enhanced salinity stratification there is accompanied by SST warming, though the underlying physical processes are not clear only from the present approach. On the other hand, regression coefficients with the opposite signs are found over the southeastern tropical IO, where significant weakening of salinity stratification is observed during pIOD events (Fig. 3.2). Thus, the local relationship between salinity and SST tendency anomalies does not hold in these regions, at least in a statistical sense. Outside of the eastern tropical IO, regression coefficients are generally small, suggesting that salinity variations play a minor role in the evolution of SST.

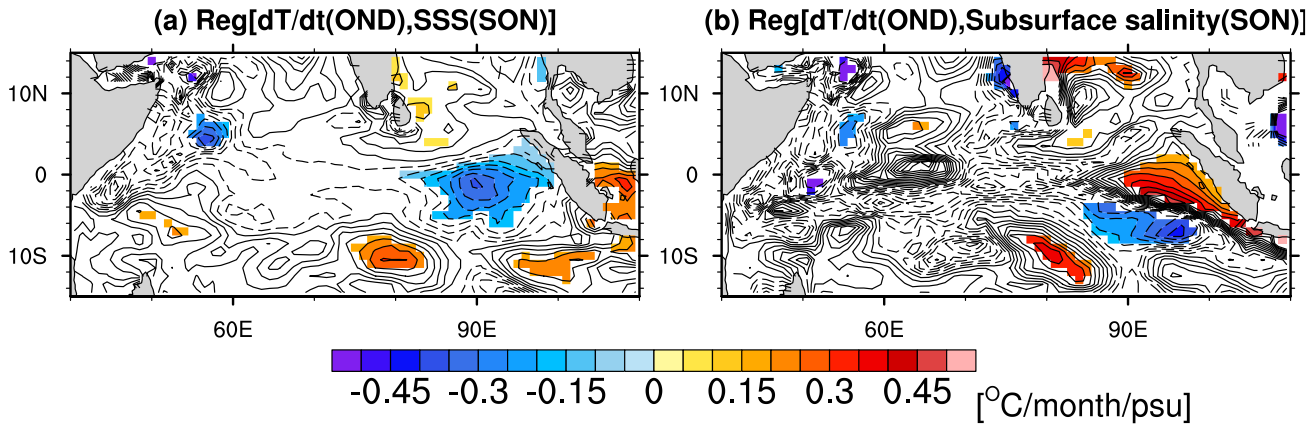

Figure 3.3: Regression coefficients of the October-December (OND) averaged SST tendency ($\frac{\partial T}{\partial t}$) against the SON-averaged (a) SSS and (b) subsurface salinity anomalies (vertically averaged over 50 [m]-100 [m] depth), having removed the influence of the OND SST anomalies (in [°C/month/psu]). The contour intervals are 0.05 [°C/month/psu]. Regression coefficients significant at the 90 % confidence level by a two-tailed t-test are shaded.

To account for the nonlocal impacts of salinity anomalies on the evolution of SST, we have applied the SVD analysis to the OND-averaged $\frac{\partial T}{\partial t}$ and the SON-averaged salinity anomalies over 65°-105°E, 15°S-15°N, following the procedures described in section 3.2.2. We note again that our results presented below are not sensitive to the selection of seasons, time lag, and spatial domain used for calculation. The regression coefficients of each variable against the corresponding time expansion coefficients of the first SVD mode are shown in Fig. 3.4 (here we present the heterogeneous regression maps; see section 3.2.2). The first SVD mode explains approximately 58% of the total squared covariance, and the correlation coefficient between the two time expansion coefficients is 0.78. The spatial patterns of associated salinity fields closely resemble those of the typical surface (Fig. 3.4b) and subsurface salinity (Fig. 3.4c) anomalies during the pIOD. The

corresponding $\frac{\partial T}{\partial t}$ field exhibits a significant warming in the EEIO (Fig. 3.4a), broadly consistent with results obtained from the regression analysis (Fig. 3.3). However, the meridional extent of regions with significant warming is somewhat broader in the SVD pattern than that of the regression analysis and more significant salinity anomalies are seen along the east coast of India.

In summary, our statistical analyses presented above imply that the pIOD-related salinity anomalies and associated changes in density stratification seem to be accompanied by SST warming in the EEIO. However, we should keep in mind that these results are based on a bold assumption (see Eq. (3.1)) and they do not necessarily reflect the actual causality in a physically consistent manner. For instance, if there is another process that simultaneously affects the evolution of $\frac{\partial T}{\partial t}$ and salinity anomalies, an apparent covariability may be detected as a statistical mode by the SVD analysis, even if there are no physical links between the two variables. To overcome these inevitable limitations in the statistical approaches, we have designed and conducted a series of numerical experiments described in section 3.2.4, and these results will be shown in the next section.

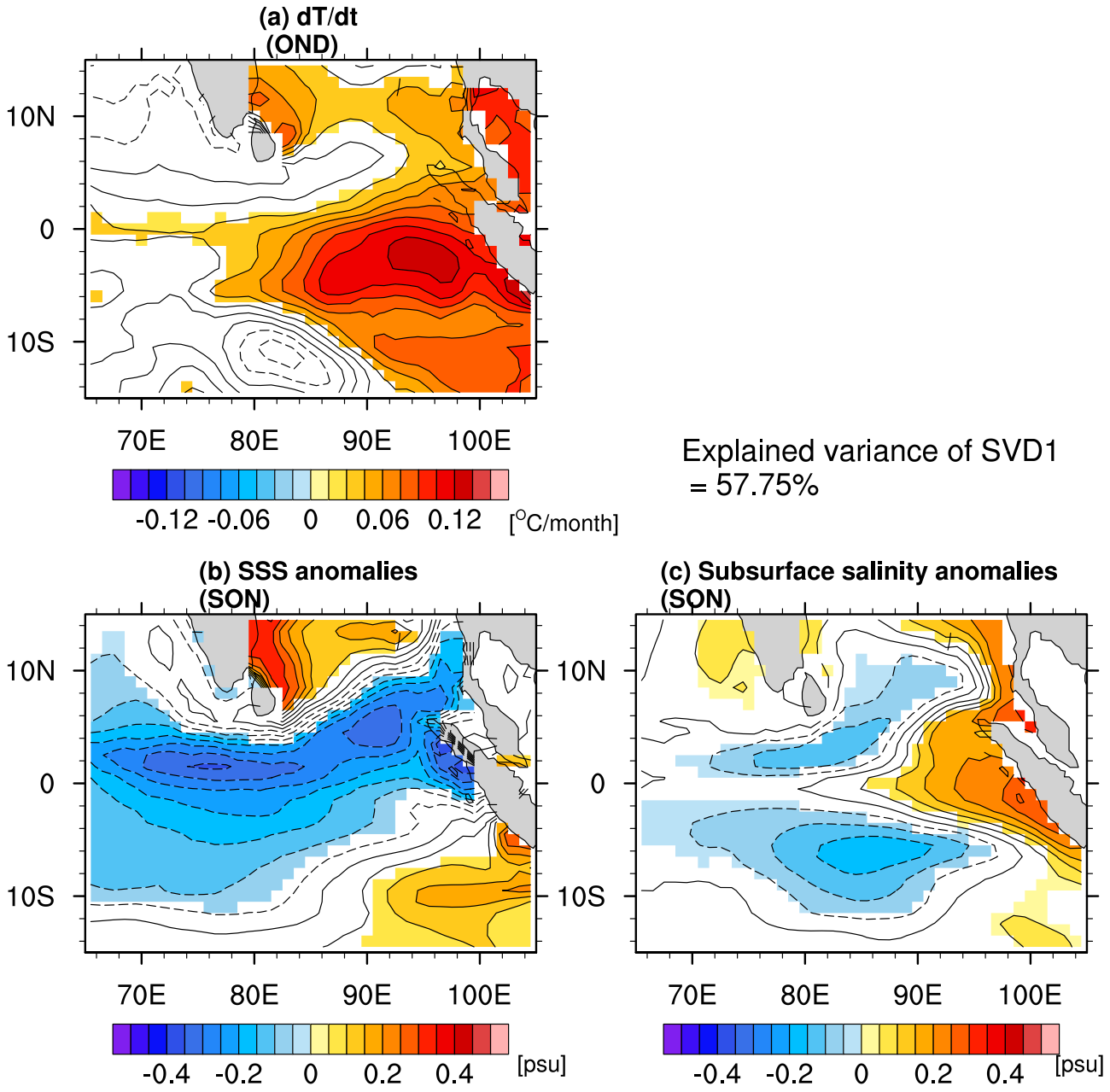

Figure 3.4: (a) Regression coefficients of the October-December (OND) averaged SST tendency ($\frac{\partial T}{\partial t}$) against the normalized time expansion coefficient of salinity of the first singular value decomposition (SVD) mode (in [°C/month]). (b,c) Regression coefficients of the September-November (SON) averaged (b) surface and (c) subsurface (vertically averaged from 50 [m] to 100 [m] depth) against the normalized time expansion coefficient of $\frac{\partial T}{\partial t}$ of the first SVD mode (in [psu]). The contour intervals in (a) are 0.02

[°C/month], whereas those in (b) and (c) are 0.05 [psu], and regression coefficients significant at the 90% confidence level by a two-tailed t-test are shaded. The percentage of squared covariance explained by the first SVD mode is shown in the lower right of (a).

3.4. Results from sensitivity experiments

To investigate the upper ocean response to the pIOD-related salinity anomalies generated by advective processes, we first present the results from the NoSADV experiments in section 3.4.1. Then, we briefly discuss the results from the PSADV experiments in section 3.4.2 to verify consistency between the two experiments.

3.4.1 NoSADV experiments

Before investigating the impacts of the pIOD-related salinity anomalies on the dynamics and thermodynamics of the upper ocean, we first check whether these salinity anomalies are adequately excluded in the NoSADV experiments. The composited salinity anomalies during the mature phase of the pIOD in Diff_CTL (i.e. CTL_MR minus CTL_NoIOD) are compared with those in Diff_NoSADV (i.e. NoSADV_MR minus NoSADV_NoIOD) (Fig. 3.5). While Diff_CTL isolates the total pIOD effect, Diff_NoSADV estimates the pIOD forcing through processes other than salinity advection. Their difference, *Diff_CTL - Diff_NoSADV*, assesses the pIOD effect via salinity advection.

In Diff_CTL, there are positive SSS anomalies in the southeastern tropical IO, and negative SSS anomalies spread over the central IO (Fig. 3.5a), as in the observation (J. Li et al., 2016; Y. Zhang et al., 2013). Significant changes in salinity are also found in the subsurface layer (around 50-100 [m] depth), such as anomalous saltening in the EEIO and freshening along the

off-equatorial bands (Fig. 3.5b). These are typical pIOD-related features of salinity anomalies, and their generation mechanisms are discussed in detail by section 2.3.1 (e.g. Figs. 2.2, 2.8). In contrast, no significant salinity anomalies are seen in the composite maps of the Diff_NoSADV except for significant surface saltening in the southeastern IO. These SSS anomalies in Diff_NoSADV are mainly induced by precipitation anomalies and associated changes in vertical diffusion of salinity (section 2.4.2), a mechanism that operates in both the CTL and NoSADV experiments. The dramatic reduction in the pIOD-related salinity anomalies in the NoSADV experiments, which can be clearly seen from Fig. 3.5c and Fig. 3.5f, implies that the pIOD-related salinity anomalies are reasonably removed in the NoSADV experiments, because advection is the major mechanism for the pIOD-related salinity variations. Therefore, as alluded in section 3.2.4, their impacts on the upper ocean state can be estimated by inspecting the differences between Diff_CTL and Diff_NoSADV.

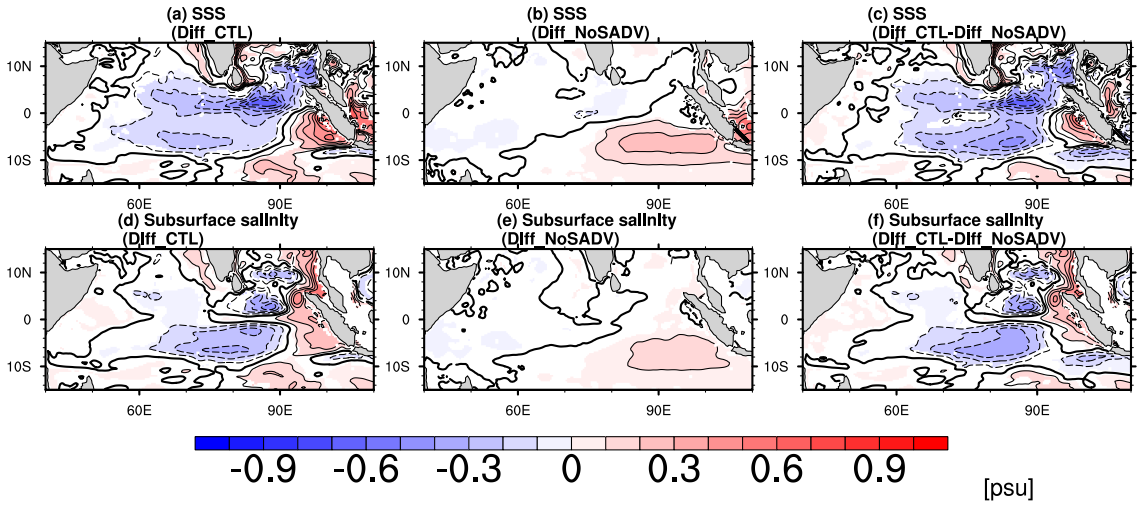

Figure 3.5: Composite of sea surface salinity (SSS) anomalies during September-November (SON) of positive Indian Ocean Dipole (pIOD) events for (a) Diff_CTL and (b) Diff_NoSADV. The difference between (a) and (b) (i.e. (a) minus (b)) are shown in (c). (d)-(f): As in (a)-(c), but for subsurface salinity anomalies (vertically

averaged from 50 [m] to 100 [m] depth). The contour intervals are 0.1 [psu], and anomalies significant at the 90% confidence level by a two-tailed t test are shaded.

The most important oceanic parameter for air-sea interaction is the SST, as it is the only oceanic parameter that can directly communicate with the atmosphere. To see how the pIOD-related salinity anomalies affect the SST, we compare SST anomalies between Diff_CTL and Diff_NoSADV (Fig. 3.6). In both sets of experiments, anomalous cooling in the eastern IO and warming in the western IO are clearly seen (Figs. 3.6a, b), suggesting that SST anomalies with the zonal dipole structure still exist even in the absence of salinity anomalies. However, the cooling in the EEIO is substantially stronger in Diff_NoSADV than Diff_CTL (Fig. 3.6c). The regions with significant SST differences between the two sets of experiments are confined to the EEIO, and their maximum amplitude reaches ~1.0 °C (Fig. 3.6c). The overall pattern of these SST differences is broadly consistent with our statistical analysis presented in section 3.3.2. The magnitude of these SST differences between the two sets of experiments amount to 30-60% of the total anomalies (Fig. 3.6d). These results suggest that the pIOD-related salinity anomalies act to reduce the SST cooling in the EEIO during pIOD, but this effect did not change the signs from cooling to warming. This is in stark contrast to the conclusion of Masson et al. (2004), who demonstrated that the presence of the salinity stratification in their OGCM leads to SST *warming* during the 1997 pIOD event. The reasons for this apparent disagreement will be presented in section 3.5.3. We can also identify regions with slight warming in the western IO, but the amplitude of the difference is considerably smaller than those in the east (Figs. 3.6c, d). Outside of the equatorial region, the differences between the two sets of experiments are relatively weak and no well-organized structures are seen, implying that the impacts of salinity anomalies in these regions are not so strong.

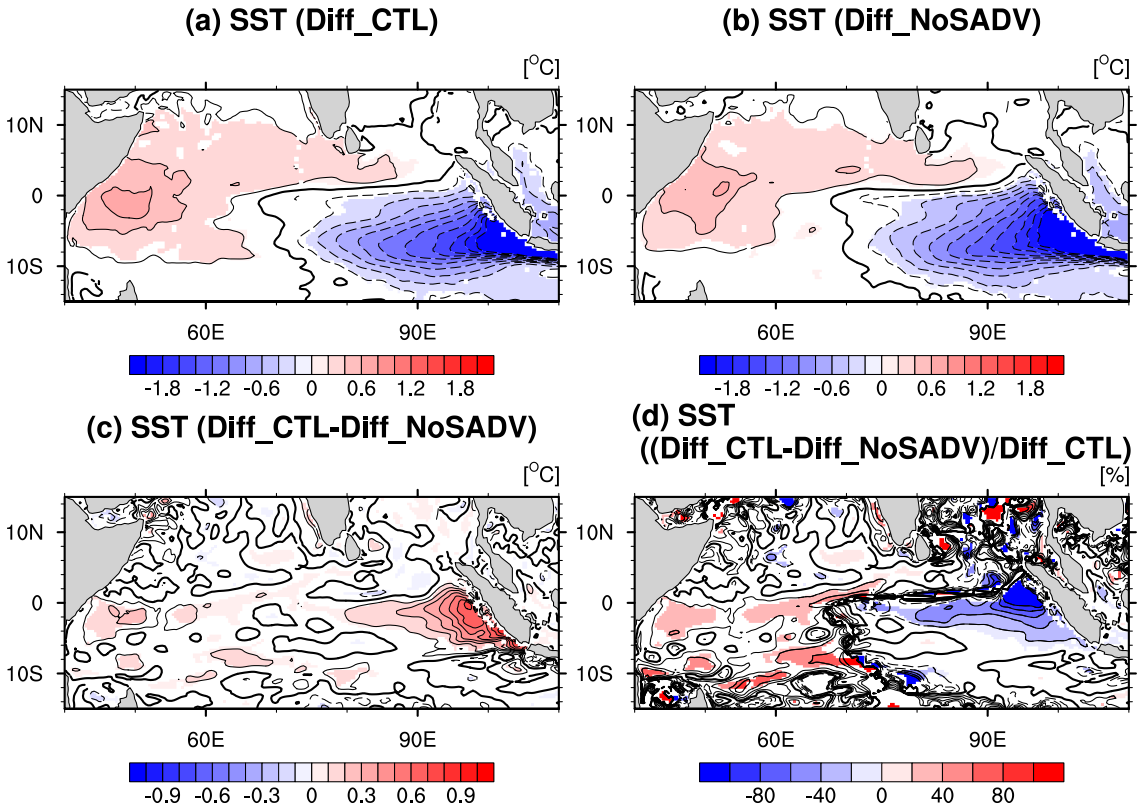

Figure 3.6: Composite of sea surface temperature (SST) anomalies during SON of pIOD events for (a) Diff_CTL and (b) Diff_NoSADV. The difference between (a) and (b) (i.e. (a) minus (b)) are shown in (c). (d) Ratio (in percentage) of the difference (i.e. Diff_CTL-Diff_NoSADV) against the total anomalies (i.e. Diff_CTL). The contour intervals are 0.2 [°C] in (a) and (b), whereas they are 0.1 [°C] in (c) and 20 [%] in (d). Anomalies significant at the 90% confidence level by a two-tailed t test are shaded.

Given that significant changes in SST are found between the two sets of experiments, we expect that other oceanic variables, such as currents, may also be strongly affected by the pIOD-related salinity anomalies. Here, we delineate the changes in sea surface height (SSH), thermocline depth, and horizontal and vertical current anomalies, as they are closely linked to SST variations through ocean dynamical processes.

In both experiments, SSH anomalies exhibit a zonal dipole structure, with positive

(negative) values appearing in the western (eastern) tropical IO (Figs. 3.7a, b). The differences between the two experiments, shown in Fig. 3.7c, demonstrate that the off-equatorial positive anomalies over the central equatorial IO in Diff_CTL is somewhat larger than those in Diff_NoSADV. This is due to the surface and subsurface freshening in this region which results in increased halosteric sea level (Figs. 3.5c, f). However, the amplitude of these differences is considerably smaller than those of total anomalies (Figs. 3.7a-c).

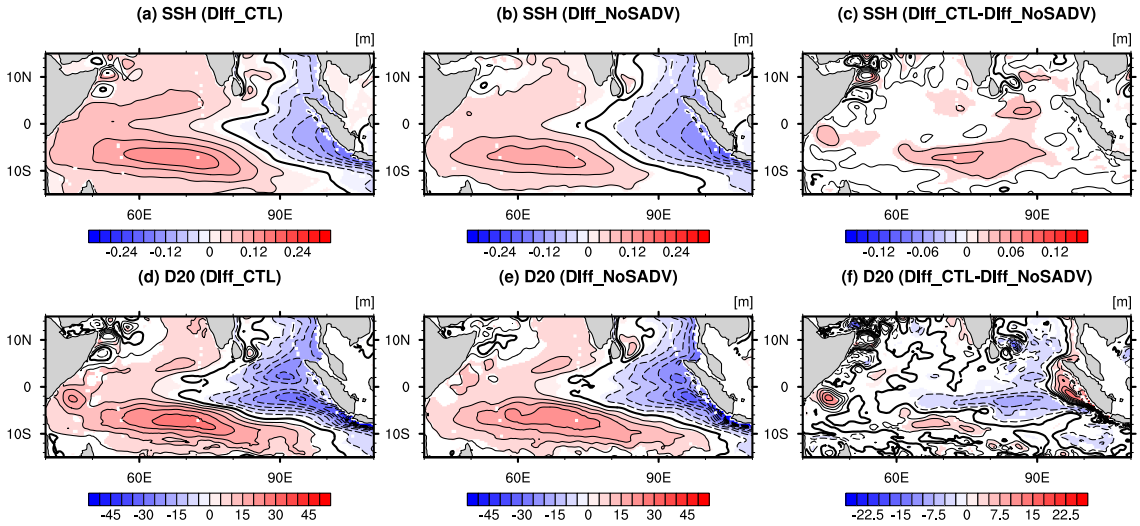

Figure 3.7: (a)-(c): As in Fig. 3.6, but for sea surface height (SSH) anomalies. The contour intervals in (a) and (b) are 0.03 [m], whereas they are 0.015 [m] in (c). (d)-(f): As in (a)-(c), but for the 20°C isothermal depth (D20) anomalies. The contour intervals in (d) and (e) are 5 [m], whereas they are 2.5 [m] in (f). Anomalies significant at the 90% confidence level by a two-tailed t test are shaded.

Anomalies with a similar zonal dipole structure are also found in the thermocline depth, which is represented as the depth of 20°C isotherm (referred to D20) (Figs. 3.7d, e). However, the differences of D20 anomalies between Diff_CTL and Diff_NoSADV are positive in the EEIO,

flanked by negative values in the off-equatorial region to the west. Note that deepened D20 signals in the eastern equatorial basin are not seen in SSH anomalies, and the increased SSH anomalies in the basin interior correspond to shallowed, rather than deepened, D20 anomalies (Fig. 3.7c). These results are different from the mirrored relationship between SSH and D20 anomalies, due to baroclinic response of tropical ocean to surface wind forcing (e.g. Fukumori et al., 1998). The D20 anomaly pattern, however, resembles that of the salinity anomalies, with deepened (shallowed) thermocline corresponding to saltening (freshening) above the thermocline (compare Figs. 3.5c, f with Fig. 3.7f). This suggests that the changes in stratification induced by salinity anomalies are the cause of the D20 anomalies. Therefore, changes in temperature, partly offset the density anomalies generated by salinity anomalies, contributing to the weak magnitude of SSH anomalies. Similar density compensation between imposed salinity anomalies and associated changes in temperature has been also reported by Cooper (1988) and Murtugudde and Busalacchi (1998), who have conducted OGCM sensitivity experiments to assess impacts of salinity effects in the tropical oceans.

As pointed out in the Introduction, salinity anomalies can alter the upper ocean circulation by modulating density stratification and pressure gradient force. To see how the pIOD-related salinity anomalies affect the current anomalies, composites of surface and subsurface current anomalies are shown in Fig. 3.8. The surface westward current anomalies in the central-eastern equatorial IO during the pIOD, which correspond to the weakening of the climatological Wyrtki Jet (Nagura & McPhaden, 2010; Nyadjro & McPhaden, 2014), are evident in both sets of experiments (Figs. 3.8a, b). However, those of Diff_CTL are somewhat stronger than those of Diff_NoSADV (Fig. 3.8c). Similarly, subsurface eastward current anomalies near the equator, which reflect anomalous intensification of the EUC during pIOD (Chen et al., 2015; Chen, Han, Shu, et al., 2016), are also stronger in Diff_CTL than Diff_NoSADV (Figs. 3.8d, e, f). The horizontal current

differences between the two sets of experiments near the equator are predominantly zonal (Fig. 3.8c), and differences in the meridional currents are relatively weak. Outside of the equatorial region, no systematic differences in current anomalies can be identified, again suggesting that the impacts of the pIOD-related salinity anomalies are mainly confined to the equatorial regions.

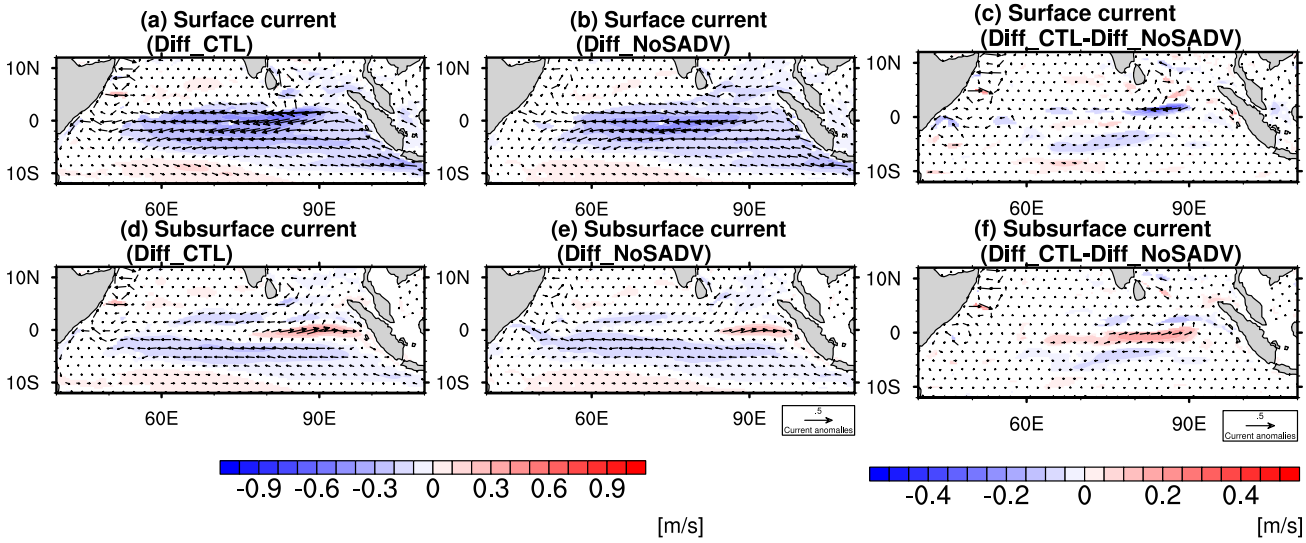

Figure 3.8: Composite of horizontal current anomalies during SON of pIOD events for (a) Diff_CTL and (b) Diff_NoSADV. The difference between (a) and (b) (i.e. (a) minus (b)) are shown in (c). (d)-(f): As in (a)-(c), but for subsurface horizontal current anomalies (vertically averaged from 50 [m] to 100 [m] depth). Color shading represents composited zonal current anomalies significant at the 90% confidence level by a two-tailed t test.

To illustrate the vertical structure of the current anomalies near the equator, the depth-longitude sections of the composited zonal and vertical velocity anomalies are presented in Fig. 3.9. The zonal current anomalies in Diff_CTL, with westward anomalies near the surface and eastward anomalies below (Fig. 3.9a), are located in shallower depth than those in Diff_NoSADV

(Fig. 3.9b). As a result, the differences between the two sets of experiments display a tripole structure, with positive values (i.e. eastward currents are stronger in Diff_CTL than those in Diff_NoSADV) around 85°E and at 50-90 [m] depth, sandwiched by regions with negative values (Fig. 3.9c).

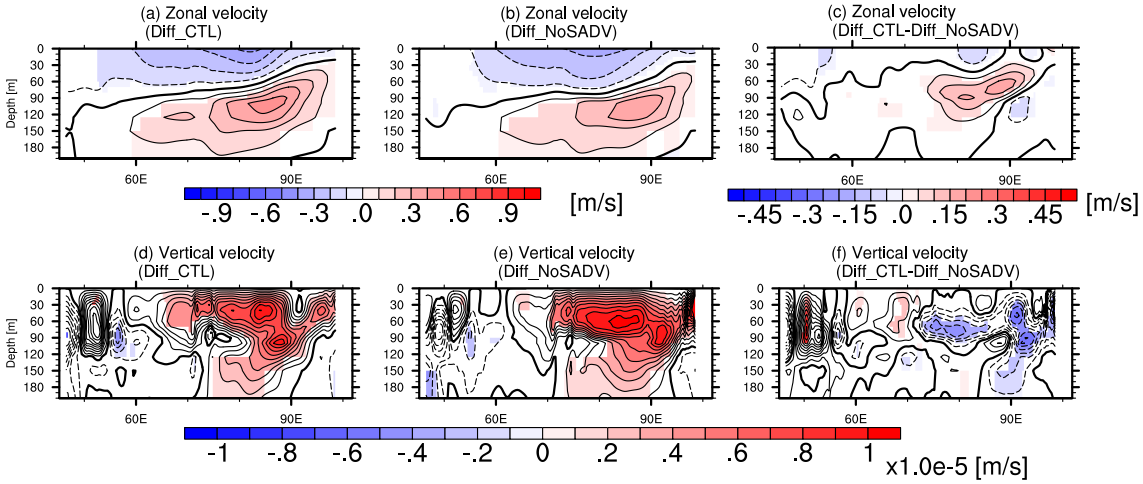

Figure 3.9: Composite of zonal velocity anomalies along the equator (meridionally averaged over 1.5°S-1.5°N) during SON of pIOD events for (a) Diff_CTL and (b) Diff_NoSADV. The difference between (a) and (b) (i.e. (a) minus (b)) is shown in (c). The contour intervals are 0.1 [m/s] in (a) and (b), whereas those in (c) are 0.05 [m/s]. (d)-(f): As in (a)-(c), but for vertical velocity anomalies. The contour intervals are 1.0×10^{-6} [m/s]. Anomalies significant at the 90% confidence level by a two-tailed t test are shaded.

For vertical velocity, there are significant positive anomalies (i.e. enhanced upward motion) over the central-eastern equatorial IO in both sets of experiments (Figs. 3.9d, e). These are primarily induced by easterly wind anomalies along the equator associated with the pIOD (Chen, Han, Li, et al., 2016). The magnitude of these anomalies, however, is substantially weaker in Diff_CTL than that in Diff_NoSADV, particularly in the EEIO (Fig. 3.9f). Therefore, we can

conclude that the pIOD-related salinity anomalies act to weaken the equatorial upwelling in the central-eastern part of the IO.

Of particular interest is that even though the pIOD-related salinity anomalies act to reduce the upwelling and weaken surface cooling in the EEIO, the positive SSS and subsurface anomalies there are stronger in Diff_CTL than Diff_NoSADV (Figs. 3.5c, f). This is because the enhanced EUC associated with the pIOD-related salinity anomalies (Fig. 3.9c) leads to increased zonal advection of the salty Arabian Sea water to the EEIO, where it is upwelled to the surface and therefore increases the SSS (Chen, Han, Shu, et al., 2016), offsetting the effect of reduced upwelling. Since both horizontal and vertical salinity advection are totally removed in Diff_NoSADV, stronger upwelling in Diff_NoSADV does not cause an increased vertical salinity advection and positive salinity anomalies.

3.4.2 PSADV experiments

To test the robustness of the results derived from the NoSADV experiments, we have conducted another set of experiments, the PSADV experiments, as described in section 3.2.4. Figure 3.10 displays the differences in various oceanic parameters between PSADV_MR and PSADV_NoIOD, which measure the impacts of pIOD-related salinity anomalies generated by the advective processes, as for those between Diff_CTL and Diff_NoSADV.

As expected from its experimental design, salinity anomalies in the PSADV_NoIOD are substantially weaker than that of the PSADV_MR, and the salinity differences between them (i.e., PSADV_MR minus PSADV_NoIOD) (Figs. 3.10a, b) bear a strong resemblance to those between Diff_CTL and Diff_NoSADV (Figs. 3.5c, f). These results suggest that salinity advection is the dominant driver of the pIOD-related salinity anomalies, and the PSADV experiments can

successfully isolate their effects. The spatial pattern of SST differences between the two experiments, with a significant warming in the EEIO (Fig. 3.10c), is also consistent with that of the NoSADV experiments (Fig. 3.6c), though the maximum amplitude (~0.6°C) in the PSADV experiments is somewhat smaller than that in the NoSADV experiments. Differences in SSHA (Fig. 3.10d) and D20 (Fig. 3.10e) also show a good agreement with those in the NoSADV experiments (Figs. 3.7c, f). Furthermore, differences in current anomalies in the PSADV experiments also exhibit qualitatively similar features as those seen in the NoSADV experiments (figures not shown). These notable agreements between the results from the PSADV and NoSADV experiments further provide evidences that the upper ocean responses to the pIOD-related salinity anomalies are adequately captured in our sensitivity experiments.

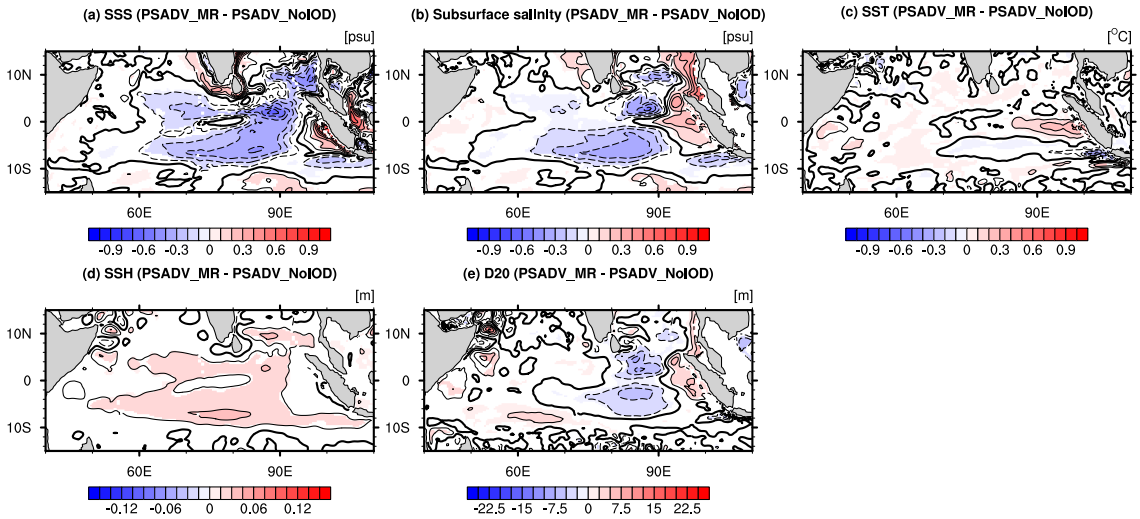

Figure 3.10: Composite of the differences in various oceanic parameters between PSADV_MR and PSADV_NoIOD during SON of pIOD events. (a) SSS, (b) subsurface salinity anomalies (vertically averaged from 50 [m] to 100 [m] depth), (c) SST, (d) SSH, and (e) D20. The contour intervals are 0.1 [psu] in (a) and (b), 0.1 [°C] in (c), 0.015 [m] in (d), and 2.5 [m] in (e). Anomalies significant at the 90% confidence level by a two-tailed t test are shaded.

To summarize, results in this section suggest that salinity anomalies associated with the pIOD do alter the upper ocean temperature and circulation near the equator, though physical processes responsible for them are unclear at this stage. In the following section, we will explore the causes for the significant differences between the two sets of experiments through quantitative analysis based on diagnostics of our regional ocean model. Since the results from PSADV and NoSADV experiments have qualitatively similar features, we will only present those obtained from the NoSADV experiments hereafter.

3.5 Dynamical diagnosis on the impacts of salinity anomalies

To understand the physical processes responsible for the differences revealed in the previous section, we first examine the results from temperature budget analysis in section 3.5.1, and show that the change in ocean circulation, especially, the strength of equatorial upwelling, is the key factor explaining the SST difference. Next, in section 3.5.2, we investigate the origins of these changes in current field by performing an on-line zonal momentum budget analysis. Finally, in section 3.5.3, we conduct additional sensitivity experiments using the LCSM to demonstrate the plausibility of the mechanisms proposed in section 3.5.2. The origins of the apparent discrepancies between our results and those of Masson et al. (2004) are also explored.

3.5.1 Temperature budget analysis

To identify the causes of the temperature difference between the two sets of experiments, we conduct an on-line temperature budget analysis. The governing equation of the temperature (denoted as T) in the ROMS can be written as follows:

$$\underbrace{\frac{\partial T}{\partial t}}_{LHS} = \underbrace{-u\frac{\partial T}{\partial x}}_{ZADV} \underbrace{-v\frac{\partial T}{\partial y}}_{MADV} \underbrace{-w\frac{\partial T}{\partial z}}_{VADV} \underbrace{+\frac{\partial}{\partial z}\left(\kappa_v \frac{\partial T}{\partial z}\right)}_{VDIFF} + \frac{\partial}{\partial x}\left(\kappa_H \frac{\partial T}{\partial x}\right) + \frac{\partial}{\partial y}\left(\kappa_H \frac{\partial T}{\partial y}\right) + \frac{1}{\rho_0 C_p}\frac{\partial I}{\partial z}. \quad (3.2)$$

In the above, κ_H and κ_v are horizontal and vertical diffusion coefficients, respectively, C_p is the specific heat of the seawater, and $I(z)$ represents the penetrative shortwave radiation (with an exponentially decaying function with depth). Each term on the right hand side of Eq. (3.2) is computed at every time step during the integration and archived as 3-day averaged value. Therefore, a closure of the heat budget is guaranteed (i.e. the value of the left hand side of Eq. (3.2) is exactly equal to the sum of all terms on the right hand side), and we have no residual terms that may

potentially hinder the identification of essential mechanisms at work.

Figure 3.11 shows the difference of temperature tendency in the longitude-depth section along the equator. Note that the differences in horizontal diffusion are not shown because they are negligible compared to others. Also, the difference in penetrative radiation is zero by definition, as the shortwave radiation forcing used in these experiments are exactly the same and our focus here is the heat budget at each vertical level. For both sets of experiments, significant cooling in the EEIO and warming in the western IO are clearly seen. The difference (Diff_CTL minus Diff_NoSADV), shown in the right column of Fig. 3.11, indicates that cooling in the EEIO, particularly near the thermocline, is stronger in Diff_NoSADV than in Diff_CTL, again suggesting that the pIOD-related salinity anomalies and related changes in currents act to warm the SST in the EEIO. A comparison of each term in the temperature tendency equation reveals that the vertical advection term is the dominant factor in explaining the differences seen in total tendency. Differences in the zonal and meridional advection, on the other hand, have negative values in this region and counteract with the changes in the vertical advection. Contributions from the vertical diffusion exhibit positive values near the surface and negative values in the subsurface. These vertical dipole structures may reflect the weakening of vertical mixing associated with enhanced salinity stratification (section 3.3.1). However, the amplitude of their contribution is considerably smaller than that of other effects. Therefore, we can conclude that the change in the strength of vertical temperature advection is the primary cause of the weaker cooling in Diff_CTL than Diff_NoSADV in the EEIO.

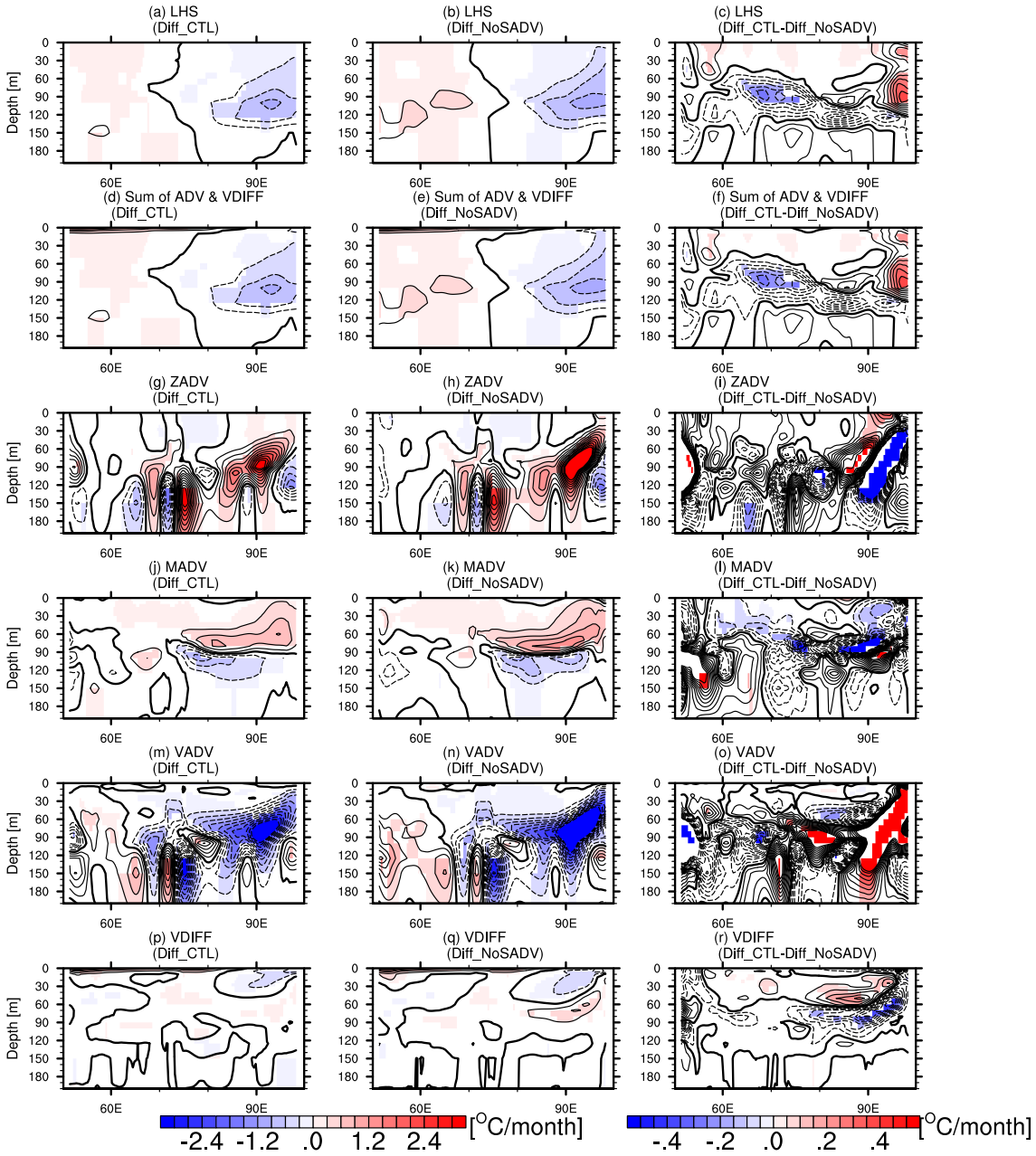

Figure 3.11: Depth-longitude section of the composited anomalies of the temperature budget terms (see Eq. (3.2) for details) during August-October (ASO) of pIOD events along the equator (meridionally averaged from 1.5°S-1.5°N) for Diff_CTL (left column), Diff_NoSADV (middle column), and the difference between the two (Diff_CTL minus Diff_NoSADV: right column). The contour intervals in the left and middle columns are 0.3 [C°/month], whereas those in the right column are 0.05 [°C/month]. Anomalies significant at the 90% confidence level are shaded.

To further elucidate the causes of the changes in the vertical advection term, we have decomposed the vertical advection term in an offline calculation as follows:

$$
\begin{aligned}
(-w\frac{\partial T}{\partial z})_{online} &= (-w\frac{\partial T}{\partial x})_{offline} + (Res.) \\
&= -w_{3days}\frac{\partial T_{3days}}{\partial z} + (Res.) \\
&= -(\overline{w} + w')\frac{\partial}{\partial z}(\overline{T} + T') + (Res.) \\
&= \underbrace{-\overline{w}\frac{\partial \overline{T}}{\partial z}}_{Term\ 1} + \underbrace{(-w'\frac{\partial \overline{T}}{\partial z})}_{Term\ 2} + \underbrace{(-\overline{w}\frac{\partial T'}{\partial z})}_{Term\ 3} + \underbrace{(-w'\frac{\partial T'}{\partial z})}_{Term\ 4} \\
&+ (Res.),
\end{aligned}
\tag{3.3}
$$

where w_{3days} and T_{3days} are 3-day averaged vertical velocity and temperature, respectively, $\overline{X}$ denotes the long-term climatology (the 3-day climatology including the seasonal cycle), and X' is deviation from the climatology (i.e. $X' = X - \overline{X}$). Here, the climatological values are obtained from the CTL_MR (i.e. a 3-day climatology of 1959-2015), and deviations from the climatology are computed for each pIOD event and experiment. The difference between the online and offline calculations (i.e. the residual term on the right hand side of Eq. (3.3)) arises from errors due to the use of a different spatial discretization and contribution of high-frequency terms that cannot be estimated by 3-day averaged values.

The physical interpretations of each term of Eq. (3.3) are as follows. The first term on the right hand side represents the advection of the climatological temperature field by the climatological vertical velocity. Analogously, the second (third) term is the advection of the climatological (anomalous) vertical temperature gradient by the anomalous (climatological) vertical velocity. The fourth term is the nonlinear dynamical heating due to correlation between vertical velocity and temperature gradient anomalies. Since Term 1 has the same value for all experiments, only Terms

2-4 are discussed.

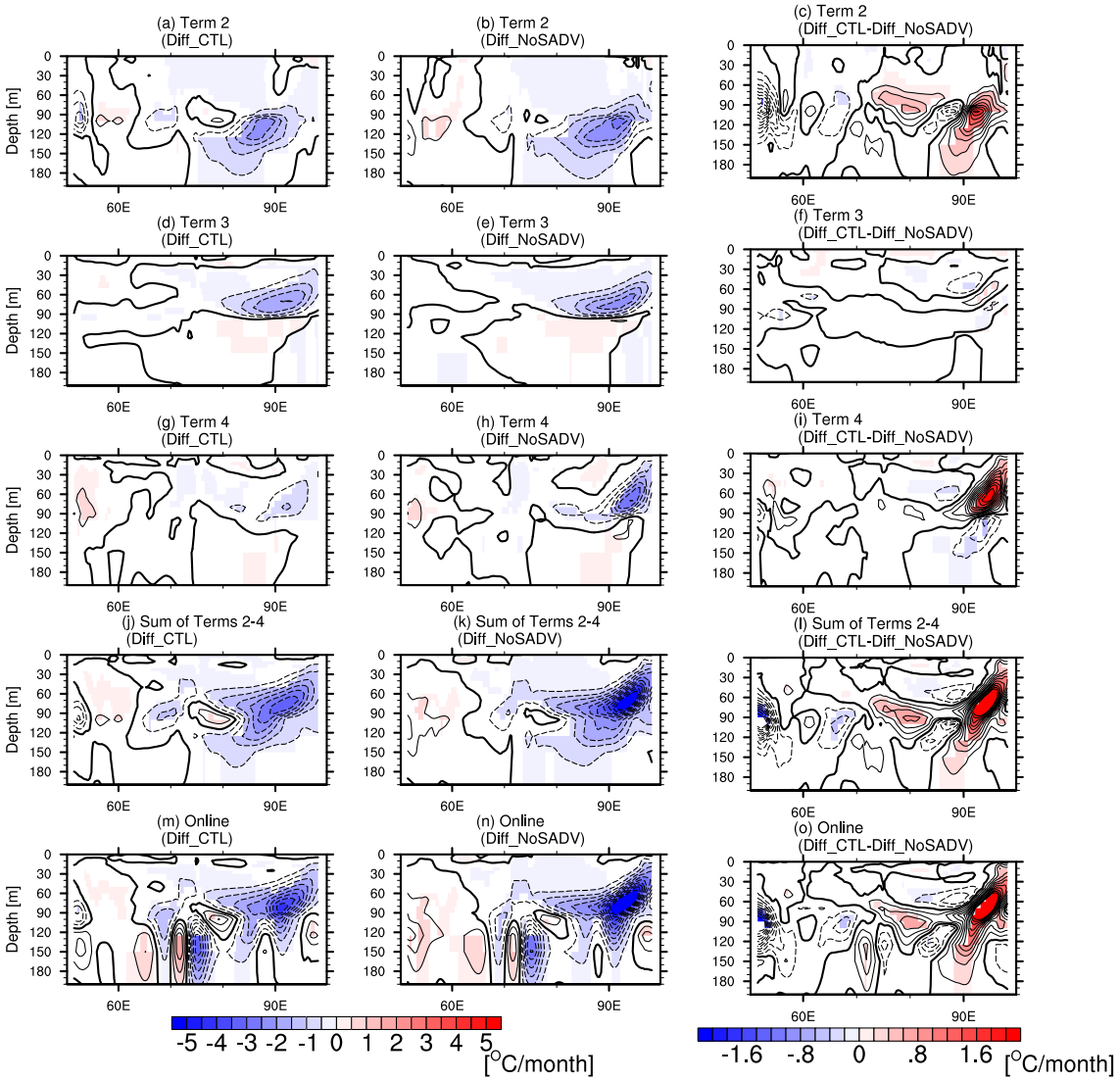

Figure 3.12: As in Fig. 3.11, but for each term in Eq. (3.3). The contour intervals in the left and middle columns are 0.5 [K/month], while those in the right column are 0.2 [K/month]. Anomalies significant at the 90% confidence level by a two-tailed t test are shaded.

Figure 3.12 displays depth-longitude sections of composited anomalies of Terms 2-4 in Eq. (3.3) and their sum along the equator. The pattern of the sum of the three terms estimated from the

offline calculation (Figs. 3.12j-l) closely resembles that of the online calculation (Figs. 3.12m-o), justifying the use of this decomposition method. For both sets of experiments, all terms contribute to cooling in the EEIO, but the regions with the minimum value are deeper for Term 2 (Figs. 3.12a, b) than for Terms 3 and 4 (Figs. 3.12d, e, g, h). Physically, this can be explained as follows. As Term 2 represents anomalous transport of climatological cold water below the thermocline, it has a minimum value where the climatological vertical temperature gradient is the largest. On the other hand, Terms 3 and 4 reflect upward spreading of anomalous cooling generated by Term 2. This anomalous cooling in the EEIO is stronger in Diff_CTL than Diff_NoSADV (Figs. 3.12l, o), and it is predominantly caused by Terms 2 and 4 (Figs. 3.12c, i), which involve vertical velocity anomalies. In contrast, differences in Term 3 have negligible influences on the total anomalies (Fig. 3.12f). These results explain the reason why the maximum differences in vertical advection anomalies between the two sets of experiments are found near the thermocline (Fig. 3.12o), and demonstrate that the change in the strength of upwelling, rather than that in temperature gradient anomalies is the key factor. Weaker upwelling in the EEIO in Diff_CTL compared to Diff_NoSADV is also consistent with these results (Fig. 3.9).

Then, through which processes the pIOD-related salinity anomalies affect the strength of the equatorial upwelling? Since the ROMS adopts the hydrostatic approximation, the vertical velocity is calculated from the horizontal current fields based on the conservation of mass. To explore the link between changes in the strength of upwelling and those in the horizontal currents, here we resort to a diagnostic approach, based on the continuity equation. The vertical velocity at a specific level ($w(z)$) can be diagnostically estimated by vertically integrating the continuity equation

$$\frac{\partial w}{\partial z} = -\left(\frac{\partial u}{\partial x} + \frac{\partial v}{\partial y}\right) \tag{3.4}$$

from the sea surface to z,

$$w(z) = w(z=0) + \int_z^0 \left(\frac{\partial u}{\partial x} + \frac{\partial v}{\partial y}\right) dz = \frac{dh}{dt} + \int_z^0 \left(\frac{\partial u}{\partial x}\right) dz + \int_z^0 \left(\frac{\partial v}{\partial y}\right) dz, \quad (3.5)$$

where h represents the SSH. Here, we used the fact that the vertical velocity at the sea surface is equal to the time derivative of SSH (i.e. $w(z=0) = \frac{dh}{dt}$). If we neglect the first term on the ride hand side of Eq. (3.5) for simplicity, we can obtain

$$w(z) = \underbrace{\int_z^0 \left(\frac{\partial u}{\partial x}\right) dz}_{ZCONV} + \underbrace{\int_z^0 \left(\frac{\partial v}{\partial y}\right) dz.}_{MCONV} \quad (3.6)$$

Thus, the vertical velocity anomalies can be decomposed into contributions from the vertically integrated convergence of zonal velocity (ZCONV) and meridional velocity (MCONV).

Figure 3.13 shows composites of vertical velocity anomalies from the ROMS outputs, those estimated from Eq. (3.6), and individual contribution from zonal and meridional components along the equator. The overall good agreement between Figs. 3.13a-c and Figs. 3.13d-f suggests that the diagnostic approach used here is reasonable at least to a first approximation. Enhanced upwelling during pIOD events in the central equatorial IO (around 60-80°E), which is evident in both sets of experiments, is mainly concomitant with meridional divergence effects (Figs. 3.13j, k). On the other hand, intensification of upward motion east of 80°E are primarily associated with the zonal component of horizontal divergence (Figs. 3.13g, h). The differences between the two sets of experiments, shown in the right column, again suggest that upwelling anomalies in the EEIO are weaker in the Diff_CTL than those in Diff_NoSADV, and they are generally related to differences in the zonal divergence (Figs. 3.13f, i, l). Therefore, we will focus on the changes in the zonal velocity and investigate how the pIOD-related salinity anomalies modulate the zonal current anomalies in the next section.

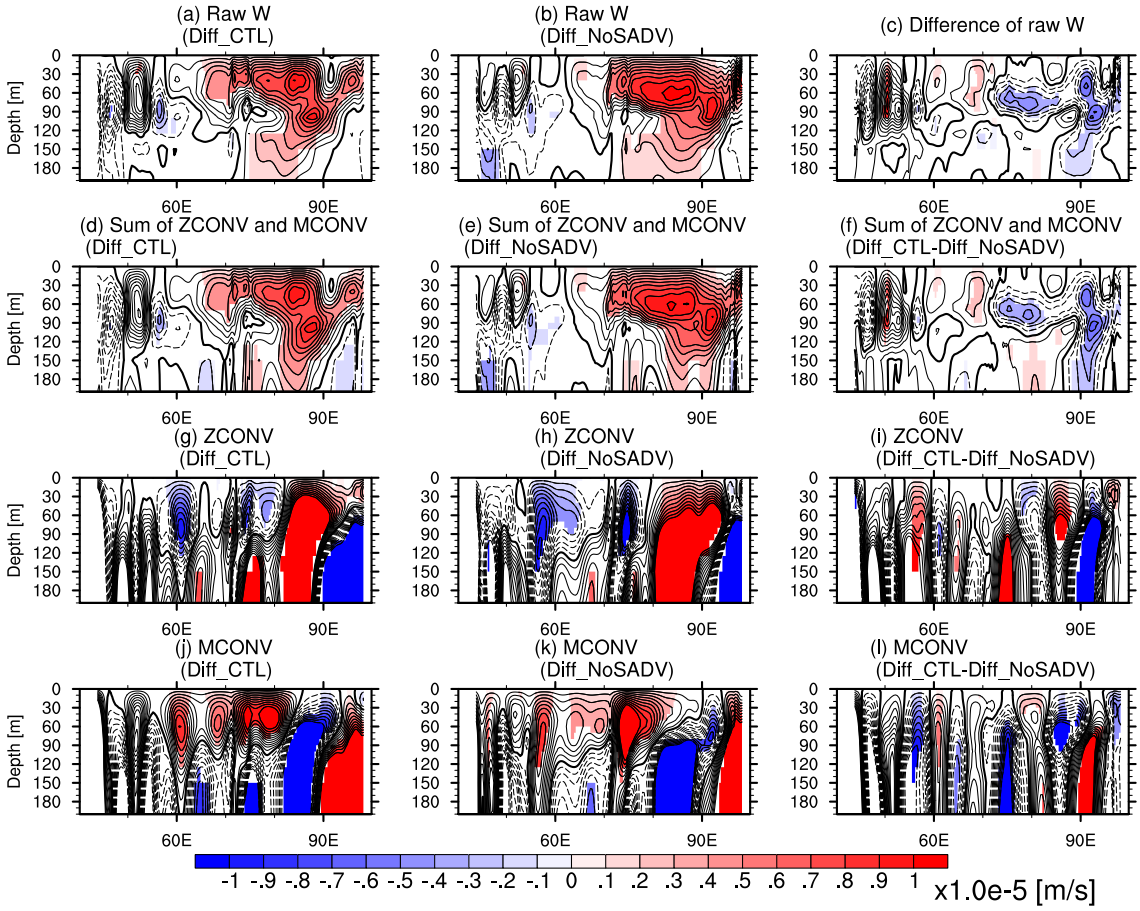

Figure 3.13: Decomposition of composited vertical velocity anomalies (see Eq. (3.6) and the main text for details) during ASO of pIOD events along the equator (meridionally averaged from 1.5°S-1.5°N) for Diff_CTL (left column), Diff_NoSADV (middle column), and the difference between the two (Diff_CTL minus Diff_NoSADV: right column). The contour intervals are 1.0×10^{-6} [m/s], and anomalies significant at the 90% confidence level are shaded.

3.5.2 Momentum budget analysis

To identify the processes by which the pIOD-related salinity anomalies alter the zonal current anomalies, we perform an online zonal momentum budget analysis. The governing equation for the zonal velocity (u) in the ROMS can be expressed as

$$\underbrace{\frac{\partial u}{\partial t}}_{LHS} = \underbrace{-u\frac{\partial u}{\partial x}}_{ZADV}\underbrace{-v\frac{\partial u}{\partial y}}_{MADV}\underbrace{-w\frac{\partial u}{\partial z}}_{VADV}\underbrace{-\frac{1}{\rho_0}\frac{\partial p}{\partial x}}_{PGF}+\underbrace{\frac{\partial}{\partial z}\left(\upsilon_v\frac{\partial u}{\partial z}\right)}_{VVISC}+fv+\upsilon_h\nabla^2 u. \qquad (3.7)$$

The effect of the surface zonal wind stress is included as the boundary condition at the sea surface, i.e. $\upsilon_v\frac{\partial u}{\partial z}(z=0)=\frac{\tau^x}{\rho_0}$ (see also Eq. (2.6a)). As in the temperature budget analysis, each term on the right hand side of Eq. (3.7) is stored at each time step during the integration to ensure the exact closure of the budget.

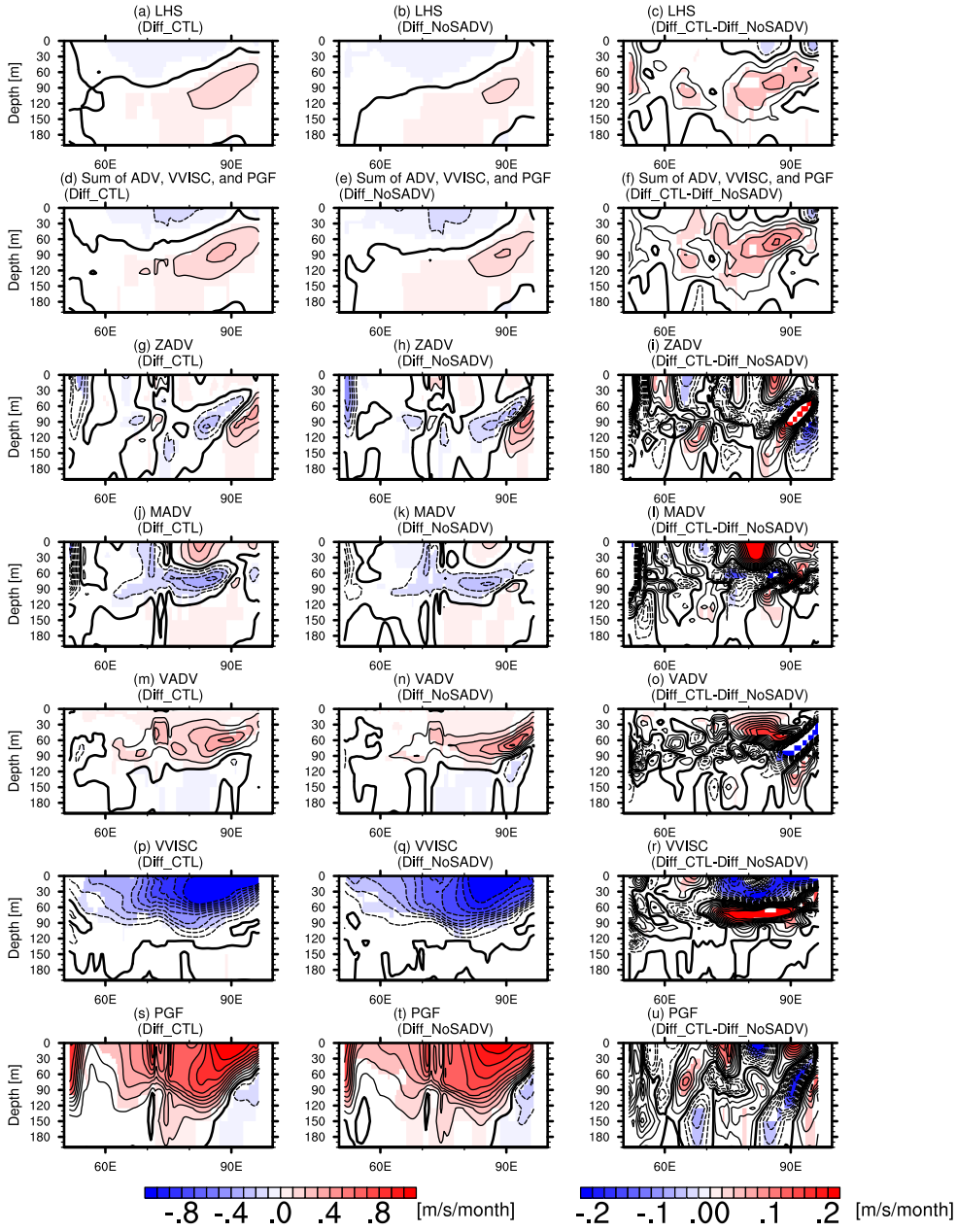

Figure 3.14: Depth-longitude section of composited anomalies of the zonal momentum budget terms (Eq. (3.7); see details for the main text) during ASO of pIOD events along the equator (meridionally averaged from 1.5°S-1.5°N) for Diff_CTL (left column), Diff_NoSADV (middle column), and the difference between the two (Diff_CTL minus Diff_NoSADV: right column). The contour intervals in the left and middle columns are 0.1 [m/s/month], while those in the right column are 0.02 [m/s/month]. Anomalies significant at the 90% confidence level by a two-tailed t test are shaded.

Figure 3.14 compares anomalies of each term on Eq. (3.7) in longitude-depth sections along the equator. The sum of momentum advective terms, pressure gradient force, and vertical viscosity term (Figs. 3.14d, e, f) matches well with the left hand side of Eq. (3.7) (Figs. 3.14a, b, c), confirming that contributions from the Coriolis and horizontal viscosity terms are relatively small compared to others along this section. Near the surface, the tendency term has westward anomalies for both Diff_CTL and Diff_NoSADV, and they are almost entirely due to the vertical viscosity term. These are consistent with previous studies (Nagura & McPhaden, 2010; D. Zhang et al., 2014) that have pointed out weakening or reversal of the surface Wyrtki Jet during pIOD events is caused by easterly wind anomalies along the equator. Below these westward anomalies, eastward anomalies with their peak around 90°E are seen (Figs. 3.14a,b). They are mainly caused by eastward pressure gradient force anomalies due to higher (lower) sea level in the western (eastern) equatorial IO (Figs. 3.7a, b). At the same time, nonlinear advection of zonal momentum also plays a role (Chen et al., 2015; J. Li et al., 2018).

The differences between Diff_CTL and Diff_NoSADV, which depict the role of the pIOD-related salinity anomalies, have westward anomalies near the surface and eastward anomalies below (Figs. 3.14c, f), consistent with zonal current anomalies (Figs. 3.8, 3.9). The pattern of these anomalies is mainly explained by that of the vertical viscosity term (Fig. 3.14r), while the pressure gradient force and momentum advection terms have anomalies with the opposite sign (Figs. 3.14i, l, o, u). Weaker changes in the pressure gradient force are in line with the smaller differences in sea level anomalies between the two sets of experiments (Fig. 3.7c). Therefore, it is the change in the vertical viscosity term that causes the upward shift of zonal velocity along the equator. That is, the enhanced stratification due to combination of the near surface freshening and subsurface saltening leads to trapping of westward momentum injection by wind anomalies, giving rise to the acceleration

of surface westward flow and the subsurface EUC.

3.5.3 LCSM experiments

In section 3.5.2, we have demonstrated that the key factors determining the response to the pIOD-related salinity anomalies are the density stratification anomalies and associated change in the vertical trapping of the momentum injected by the wind. The importance of salinity stratification in changing the vertical momentum trapping was underscored by Masson et al. (2004), even though the result of their sensitivity experiment seems different from that of ours. Since the LCSM can encapsulate the essential process mentioned above, it serves as a powerful tool to testify the validity of our findings derived from the ROMS in a concise manner. For this reason, we have conducted several sensitivity experiments using the LCSM, as explained below.

First, we have prepared two sets of spatially varying wind projection coefficients using different background density stratification fields as inputs for the LCSM. The control background stratification, STRF_CTL, is obtained from the composited temperature and salinity profiles of the CTL_MR during SON of pIOD events (Fig. 3.16g: black line). Using STRF_CTL, the first set of wind projection coefficients containing both effects of the pIOD-related temperature and salinity anomalies, is computed at each grid point. Next, the other set of the wind projection coefficients is calculated from the other background stratification, referred to STRF_SCLM, using the same composited temperature profiles as STRF_CTL, but salinity profiles from CTL_NoIOD (Fig. 3.16g: red line). Thus, the effects of changes in the stratification due to the pIOD-related salinity anomalies are only present in STRF_CTL.

To understand how the pIOD-related salinity anomalies alter wind projection coefficients, we compare the values of b_n derived from different background stratification over the EEIO in Fig.

3.15a. For the lower modes ($n = 1\sim3$), the values of b_n from STRF_CTL and STRF_SCLM are nearly the same. In contrast, for the intermediate ($n = 4\sim10$) and higher ($n > 10$) modes, STRF_CTL has larger value of b_n than STRF_SCLM, indicating that higher baroclinic modes tend to be more efficiently excited in STRF_CTL than STRF_SCLM. These results suggest that enhanced density stratification associated with the pIOD-related salinity anomalies is conducive to the excitation of the higher vertical modes. On the other hand, the phase speeds (c_n) shown in Fig. 3.15b are hardly distinguishable from each other for all values of n, implying that they are not strongly influenced by the pIOD-related salinity anomalies. Therefore, we have decided to use the same (spatially uniform) c_n values for both experiments.

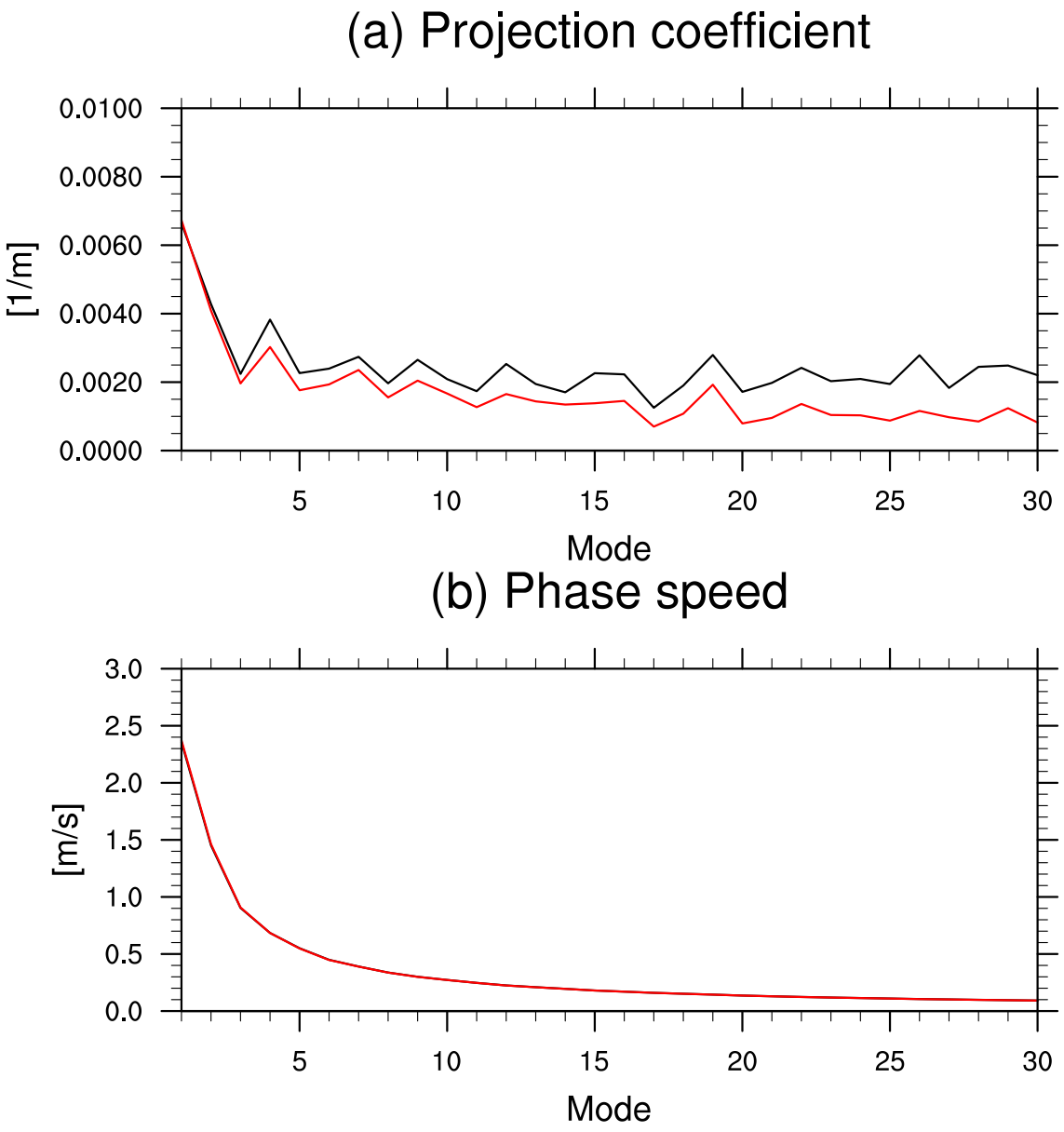

Figure 3.15: Area-averaged (a) wind projection coefficients and (b) phase speed of each baroclinic mode over the eastern equatorial Indian Ocean (90°-100°E, 5°S-5°N). The black lines indicate results computed from STRF_CTL, while the red lines are from STRF_SCLM.

Using these wind projection coefficients, we have carried out two LCSM sensitivity experiments to extract the differences in the ocean dynamical responses to the wind anomalies associated with the pIOD, under the two different sets of background stratification. For this purpose,

we have prepared the "pIOD-related wind stress forcing" spanning from May 1st to December 31st, by calculating the differences between the composited wind forcing of the ROMS CTL_MR (i.e. ensemble mean of the original JRA55-do forcing during pIOD events) and those of the ROMS CTL_NoIOD (the "NoIOD forcing" processed from JRA55-do wind forcing: see section 2.2.3 for its details). Using this wind stress forcing and wind projection coefficients from STRF_CTL, the LCSM main run (LCSM_MR) is initiated from the state of rest and integrated for 8 months from May 1st to December 31st, similar to the LCSM experiments presented in section 2.4.4. For the other experiment, referred to LCSM_SCLM, the LCSM is similarly forced as in LCSM_MR, but wind projection coefficients from STRF_SCLM are used instead of those from STRF_CTL. The only difference between LCSM_MR and LCSM_SCLM is in the wind projection coefficients imposed on the model, and therefore, we can infer the impacts of anomalous salinity stratification onto the upper ocean currents by taking the difference between the two experiments. Here, the time averaged currents field from August to October is shown to facilitate comparison between LCSM and ROMS results.

Figure 3.16 shows current anomalies along the equator during the peak phase of the pIOD. Similar to current anomalies in the ROMS sensitivity experiments (Fig. 3.9), the combination of significant westward current anomalies near the surface and eastward current anomalies below is clearly detected in both LCSM runs. In addition, enhanced upwelling over the central-eastern equatorial IO is evident (Figs. 3.16d, e, h). Due to the absence of nonlinear effects and/or crude parameterization of vertical mixing, the LCSM tends to overestimate the pIOD-related current anomalies. However, the qualitative features of the overall current anomalies are nicely reproduced. More importantly, the differences in zonal and vertical velocity anomalies between LCSM_MR and LCSM_SCLM (Figs. 3.16c, f) bear a strong resemblance to those between ROMS Diff_CTL and Diff_NoSADV (Figs. 3.9c, f), despite some discrepancies in detailed vertical structure. To highlight

the differences in the structure of vertical velocity, the area-averaged vertical velocity over the EEIO (93°E-98°E, 1.5°S-1.5°N) from both experiments are shown in Fig. 3.16h. Accompanied by stronger eastward current around 20-40 [m] depth in LCSM_MR than LCSM_SCLM, the core of vertical velocity shifts upward and upward motion above (below) that depth is strengthened (weakened) (Figs. 3.16f, h). Due to weaker vertical temperature gradient and stratification in the upper part of the mixed layer (Fig. 3.16g), (slightly) enhanced upwelling there does not significantly affect the SST. In contrast, the intensification of the downward current near the thermocline dramatically suppresses the SST cooling. Decomposition of current differences into each vertical baroclinic mode (figure not shown) reveals that higher-order modes (n>10) explain a substantial fraction of the total differences, implying the local nature of the governing dynamics.

Although only the impacts of the pIOD-related salinity anomalies on the density stratification are incorporated in the LCSM experiments, the upward shift of zonal current anomalies and associated weakening of the upward current near the thermocline in the EEIO are adequately captured, as in the ROMS experiments. These results further confirm our finding that the pIOD-related salinity anomalies alter the currents and temperature fields primarily by changing density stratification, rather than by modulating the pressure gradient force.

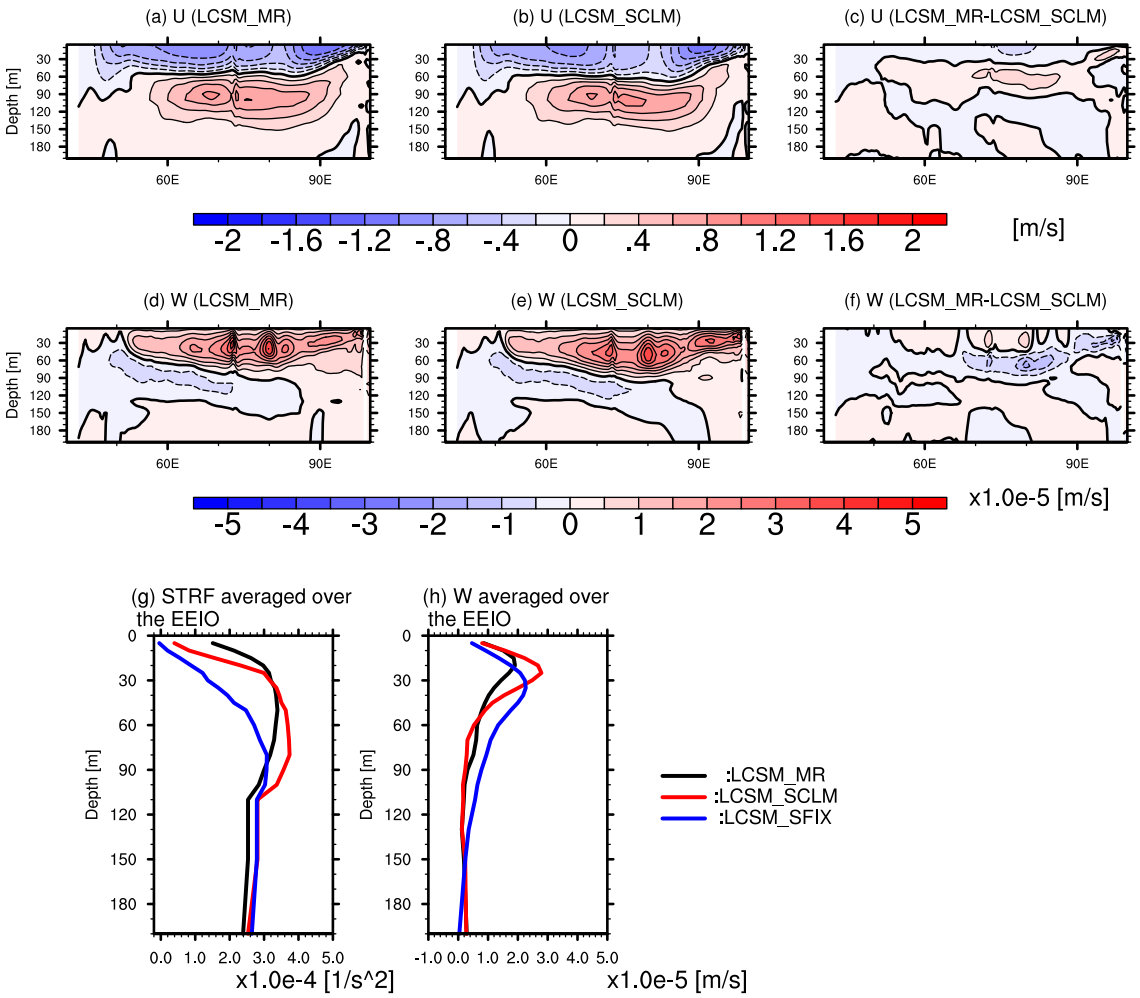

Figure 3.16: (a-c): Time-averaged (from August to October) depth-longitude section of zonal velocity from the linear continuously stratified model (LCSM) experiments ((a) for LCSM_MR and (b) for LCSM_SCLM) along the equator (meridionally averaged from 1.5°S-1.5°N). The difference between (a) and (b) is shown in (c) (i.e. (a) minus (b)). (d)-(f) As in (a)-(c), but for vertical velocity. The contour intervals in (a)-(c) are 0.2 [m/s], while those in (d)-(f) are 5.0×10^{-6} [m/s]. (g), (h): Area-averaged (g) stratification (i.e. the squared buoyancy frequency: $N^2(z)$) and (h) vertical velocity over the EEIO (93°E-98°E, 1.5°S-1.5°N) from each LCSM experiment (time averaged from August to October). The black lines represent results from LCSM_MR, while red (blue) lines are from LCSM_SCLM (LCSM_SFIX).

As reviewed in section 3.1 and section 3.4, Masson et al. (2004) have also attempted to evaluate the impacts of salinity on the IOD, focusing on the strong pIOD event in 1997. By conducting an experiment using an OGCM, they concluded that salinity stratification (both its mean and variability) acts to intensify the zonal currents anomalies and equatorial upwelling and hence, enhances the SST cooling in the EEIO associated with the pIOD. The upward shift of the zonal current anomalies due to salinity effects in their experiment is consistent with our results. However, they have reported strengthening of the equatorial upwelling and SST cooling due to salinity effect, in contrast to our conclusion. These discrepancies are not due to the selection of a specific event, as changes in the upper ocean fields due to salinity anomalies in the 1997 pIOD event in our model experiments have consistent features as the composited fields. The use of different OGCMs is also not likely to be the major cause, as we obtained qualitatively similar results to those of Masson et al. (2004) with a sensitivity experiment identical to theirs using our ROMS (figures not shown). Then, what is responsible for the contrasting results? Here, we suggest that the apparent contradiction is caused by distinctive roles played by the pIOD-related variation of salinity stratification and those by the mean component, which was not explicitly isolated by Masson et al. (2004).

To substantiate the aforementioned argument, we have carried out another LCSM experiment, referred to LCSM_SFIX, which employs the density stratification obtained from the composited temperature and constant (35 psu) salinity for the calculation of wind projection coefficients (Fig. 3.16; blue line). The wind forcing and integration period are the same as those of LCSM_MR and LCSM_SCLM. Therefore, the collective effects of salinity stratification (both its mean and anomaly), which have been assessed by Masson et al. (2004), can be measured by taking the difference between LCSM_MR and LCSM_SFIX, whereas those of the mean component are estimated by the difference between LCSM_SCLM and LCSM_SFIX.

The differences in zonal and vertical currents along the equator between each pair of experiments are presented in Fig. 3.17. Consistent with Masson et al. (2004), the presence of total salinity stratification leads to strengthening of the equatorial zonal circulation and upwelling in the central-eastern equatorial IO (Figs. 3.17a, d; see also Fig. 3.16h). However, the enhanced upwelling in the EEIO is predominantly caused by the mean component of salinity stratification (Figs. 3.17c, f), rather than by its anomaly associated with the pIOD (Figs. 3.17b, e). Since contributions from both effects are included in the sensitivity experiments of Masson et al. (2004) and the former overwhelms the latter, they have reached conclusion that the presence of salinity stratification reinforces the equatorial circulation and SST cooling in the EEIO. In contrast, our sensitivity experiments are carefully designed to extract contributions only from the latter (i.e. the pIOD-related variation of salinity stratification). Therefore, we have succeeded in capturing the suppression of the equatorial upwelling and SST cooling due to the pIOD-related salinity anomalies from these experiments. The above results from LCSM sensitivity experiments successfully reconcile the seemingly conflicting results presented by Masson et al. (2004) and ours, and underscore the importance of distinguishing the impacts of the anomalous salinity stratification and those due to its mean component.

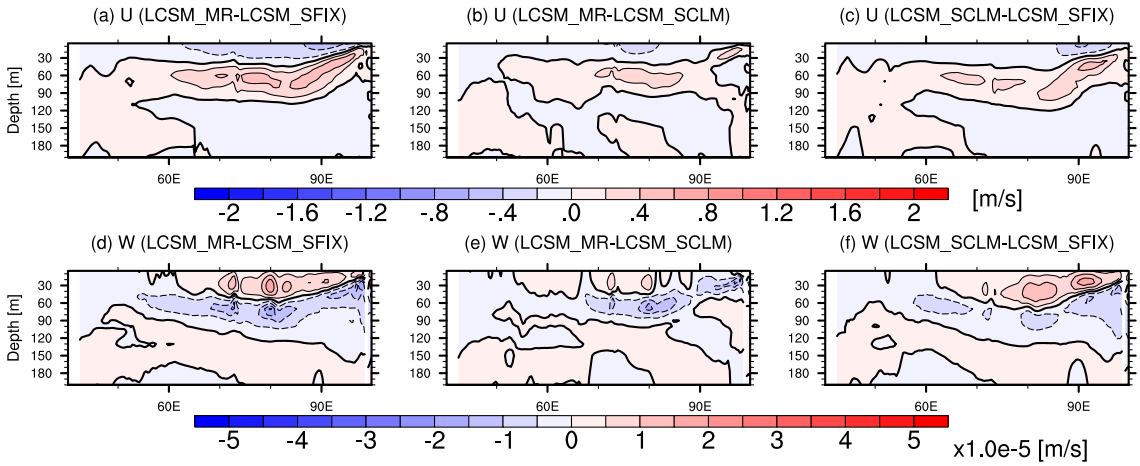

Figure 3.17: Time-averaged (from August to October) difference (former minus latter) in zonal velocity between (a) LCSM_MR and LCSM_SFIX, (b) LCSM_MR and LCSM_SCLM, and (c) LCSM_SCLM and LCSM_SFIX experiments along the equator (meridionally averaged from 1.5°S-1.5°N). (d)-(f) As in (a)-(c), but for vertical velocity. The contour intervals in (a)-(c) are 0.2 [m/s], while those in (d)-(f) are 5.0×10^{-6} [m/s].

3.6 Summary and discussions

In this chapter, we have investigated impacts of pIOD-related salinity anomalies on the upper ocean fields through data analysis and numerical experiments using a regional ocean model. First, we have assessed the relative importance of temperature and salinity anomalies in the generation of density and vertical stratification anomalies using a density decomposition method. It is found that contribution from anomalous salinity stratification to density stratification is comparable, or even larger than that from anomalous thermal stratification in the EEIO and southern tropical Indian Ocean, compared to temperature anomalies. Then, conventional statistical techniques are invoked to identify the footprints of salinity influences on the evolution of SST. The results from these analyses suggest that the pIOD-related salinity anomalies are conducive to the SST warming of the EEIO.

However, giving the limitation of the data analysis, impacts of salinity anomalies associated with the pIOD have been assessed through a series of sensitivity experiments using a regional ocean model and an LCSM. By comparing hindcast simulations of pIOD events with and without advectively generated salinity anomalies, we found that the pIOD-related salinity anomalies act to significantly suppress the SST cooling in the EEIO during the pIOD, with maximum values of about 1.0°C. The upper ocean circulation is also strongly modulated by the salinity anomalies. Specifically, the zonal current anomalies typical of pIOD events, with weakening of the surface eastward Wyrtki Jet and anomalous intensification of the EUC, are confined to the upper layer due to the pIOD-related salinity anomalies. Simultaneously, the anomalous intensification of the equatorial upwelling in the EEIO around the thermocline is significantly suppressed. It is encouraging that the results obtained from statistical analysis (section 3.3) and detailed sensitivity experiments (sections 3.4 and 3.5) are broadly consistent in a qualitative sense. Although we need to be cautious about their

interpretations, the statistical approaches introduced in this study may serve as powerful tools for finding some possible impacts of salinity variations

The causes of the above-mentioned changes in the upper ocean temperature and currents are then explored through diagnostics of heat and zonal momentum budget. The processes by which the pIOD-related salinity anomalies affect the upper ocean properties are schematically summarized in Fig. 3.18. During pIOD events, the EEIO experiences anomalous surface freshening and subsurface saltening. The emergence of these salinity anomalies with the opposite signs leads to enhanced density stratification and the inputs of momentum from the wind forcing are more strongly trapped within the surface layer. Accordingly, zonal and vertical current anomalies are confined to the upper layer, and upward transports of cold water below the thermocline to the surface are significantly reduced. Consequently, the SST cooling in the EEIO is significantly suppressed. The plausibility of this mechanism is further confirmed by additional sensitivity experiments using the LCSM. The causes of difference in the conclusion of ours and that of Masson et al. (2004) are also explained by these LCSM experiments.

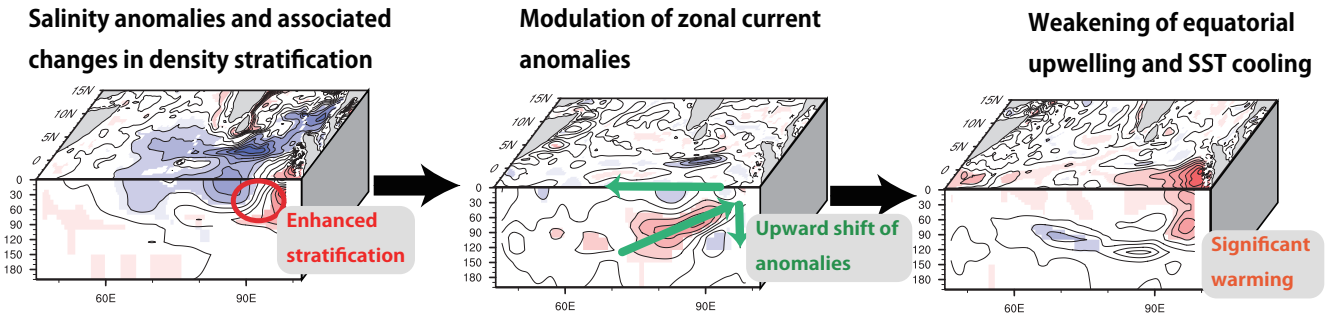

Figure 3.18: Schematic diagram illustrating how the pIOD-related salinity anomalies affect the upper ocean currents and temperature near the equator. See the main text for details.

Finally, we discuss the reasons why no prominent impacts of salinity are detected in the southeastern tropical IO, even though salinity stratification there is substantially weakened (Fig. 3.2). For this purpose, we have also checked the changes in heat budget between the two sets of experiments for the off-equatorial region (Fig. 3.19). Consistent with the weakening of density stratification, stronger vertical mixing is observed in Diff_CTL than Diff_NoSADV, leading to negative (positive) vertical diffusion anomalies above (below) the thermocline (Fig. 3.19f). However, resulting surface cooling is damped by zonal advection (Fig. 3.19c), and there are no net differences in the total tendency term between the two sets of experiments (Figs. 3.19a, b). Therefore, although the pIOD-related salinity anomalies act to destabilize the upper ocean and assist the surface cooling in the southeastern tropical IO, their effects are counteracted by advective processes and no significant changes in SST are seen there. These results again demonstrate that a simple "one-dimensional" consideration of salinity impacts on the upper ocean stratification and SST is not a universal principle, and delineate the complexity of the interplay between salinity anomalies and related physical processes.

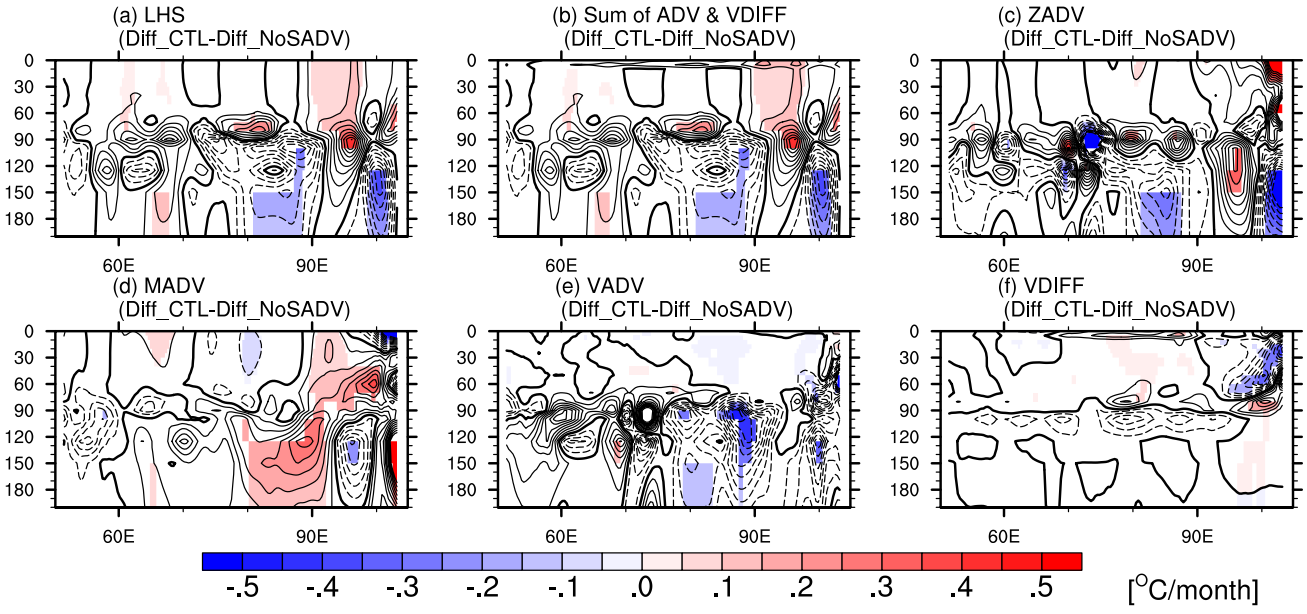

Figure 3.19: As in Fig. 3.11, but for the off-equatorial region (averaged over 8°S-4°S).

Chapter 4

General conclusions

In this thesis, mechanisms and impacts of salinity variations associated with the Indian Ocean Dipole (IOD) have been investigated through analysis of observational/reanalysis datasets and a series of sensitivity experiments using a regional ocean model system (ROMS) and a linear continuously stratified model (LCSM). The key findings of this thesis are visually illustrated in Fig. 4.1. We first summarize the main findings obtained in the course of this work in section 4.1, and then discuss several important issues that have not been treated in the main chapters in section 4.2. Some caveats of our results are also remarked there. Finally, possible implications for future studies are presented in section 4.3.

4.1 Summary

In Chapter 2 (see blue rectangular in Fig. 4.1), we have examined the features of salinity variability in the tropical Indian Ocean (IO) during the IOD using observational datasets and ocean reanalysis products. It is found that during a positive IOD (pIOD) event, the central-eastern equatorial IO (southeastern tropical IO) experiences significant surface freshening (saltening), as previously reported by many studies (Grunseich et al., 2011; Thompson et al., 2006; Y. Zhang et al., 2013). In addition to these surface anomalies, conspicuous salinity variations near the halocline, with anomalous saltening (freshening) in the eastern equatorial IO (southeastern tropical IO) are detected for the first time in this study. The spatial pattern of these subsurface salinity anomalies is distinct from that of the surface anomalies. A partial regression analysis reveals that these salinity variations in the tropical IO are mainly caused by the local IOD-related forcing, rather than by remote influences related to the El Niño-Southern Oscillation (ENSO). These surface and subsurface anomalies, as well as variations of other oceanic variables associated with the IOD are successfully captured in a hindcast simulation of a regional ocean model forced by realistic atmospheric and

lateral boundary conditions.

The mechanisms and processes giving rise to these salinity anomalies are then examined for the first time by conducting an online salinity budget analysis and a series of sensitivity experiments using the regional ocean model. It turns out that a large fraction of surface and subsurface salinity anomalies associated with the pIOD are primarily induced by dynamical effects of wind stress anomalies. On the other hand, freshwater flux anomalies in the southeastern tropical IO, caused by both enhanced evaporation due to stronger wind speed and reduction of precipitation, are also important for positive SSS anomalies there. Other effects, such as shortwave radiation anomalies and changes in the lateral boundary forcing, have a negligible contribution to the salinity anomalies.

A detailed decomposition of advective anomalies demonstrated that large-scale current anomalies induced by anomalous wind stress related to the pIOD are the dominant factors explaining the total salinity advection anomalies, again consistent with many recent works (J. Li et al., 2016; Y. Zhang et al., 2013). However, the low-frequency modulation of nonlinear salinity advection associated with high-frequency variability, which has not been explicitly discussed so far, is also shown to be crucial for the generation of the pIOD-related salinity anomalies, particularly in regions with vigorous intraseasonal variability. In the eastern equatorial Indian Ocean (EEIO), the cumulative effect of the nonlinear meridional salinity advection by intraseasonal mixed Rossby-gravity waves is net freshening near the pycnocline, and the vertical displacement of the pycnocline in response to the pIOD leads to an upward shift of these nonlinear salinity advection, resulting in a vertical dipole of meridional salinity advection anomalies, with anomalous freshening (saltening) above (below) the climatological pycnocline. The validity of this dynamical explanation is further corroborated by additional sensitivity experiments using an LCSM that contains essential

physics. In the southeastern tropical IO, on the other hand, the intensification of mesoscale eddy activity during the pIOD gives rise to the modulation of eddy-induced salinity advection, and affects the evolution of SSS there.

Impacts of the pIOD-related salinity anomalies investigated in Chapter 2 and related physical processes are then explored in Chapter 3 (see red rectangular in Fig. 4.1). Decomposition of density anomalies reveals that the pIOD-related salinity anomalies have comparable, or even larger impacts on the total density stratification, suggesting their potential impacts on the upper ocean fields. Partial regression and SVD analyses suggest that the pIOD-related salinity anomalies tend to be accompanied by SST warming in the EEIO with a slight lag (i.e. salinity anomalies leads the SST tendency), implying some possible roles of the salinity anomalies on the SST evolution. To assess these impacts in a quantitative manner, we have designed and carried out several sensitivity experiments using the ROMS adopted in Chapter 2. Considering the fact that the dominant factor causing these salinity anomalies is anomalous salinity advection, we have artificially modified salinity advection in the ROMS to assess their collective impacts. Our results have shown that the experiments without the pIOD-related salinity anomalies exhibit stronger SST cooling in the EEIO compared to the original experiments (i.e. experiments containing the salinity anomalies), implying that the pIOD-related salinity variations act to damp the negative SST anomalies in the eastern pole of the IOD. Remarkable differences are also found in other variables, such as SSH, thermocline depth, and current fields.

The causes of these changes in the upper ocean temperature and circulation are then pursued through comprehensive diagnostics of heat and zonal momentum budget analyses. It is shown that anomalous surface freshening and subsurface saltening in the EEIO strengthen the density stratification and shoal the mixed layer during the pIOD. As a consequence, the momentum

forcing injected by the wind stress is more confined to the surface, and associated anomalous zonal circulation along the equator, with westward (eastward) current anomalies near the surface (below the thermocline), is lifted upward. Correspondingly, upwelling near the thermocline is substantially weakened in the EEIO, and eventually leads to suppression of SST cooling there.

To confirm the plausibility of the above-mentioned mechanism and isolate the essential dynamical process, we have further conducted a series of LCSM experiments, which only differ in the background density stratification used to calculate the wind projection coefficients in the model. We have obtained qualitatively similar results to those of the ROMS experiments, again indicating the robustness of our results and validity of physical interpretations. An additional LCSM experiment, forced with the background density stratifications calculated with constant salinity, successfully reproduced the features appeared in the sensitivity experiment of Masson et al. (2004). Thus, apparent discrepancies in their conclusions and those of this study stem from the fact that the mean salinity stratification and its fluctuation associated with the pIOD exert influences of the opposite signs on the vertical velocity near the thermocline.

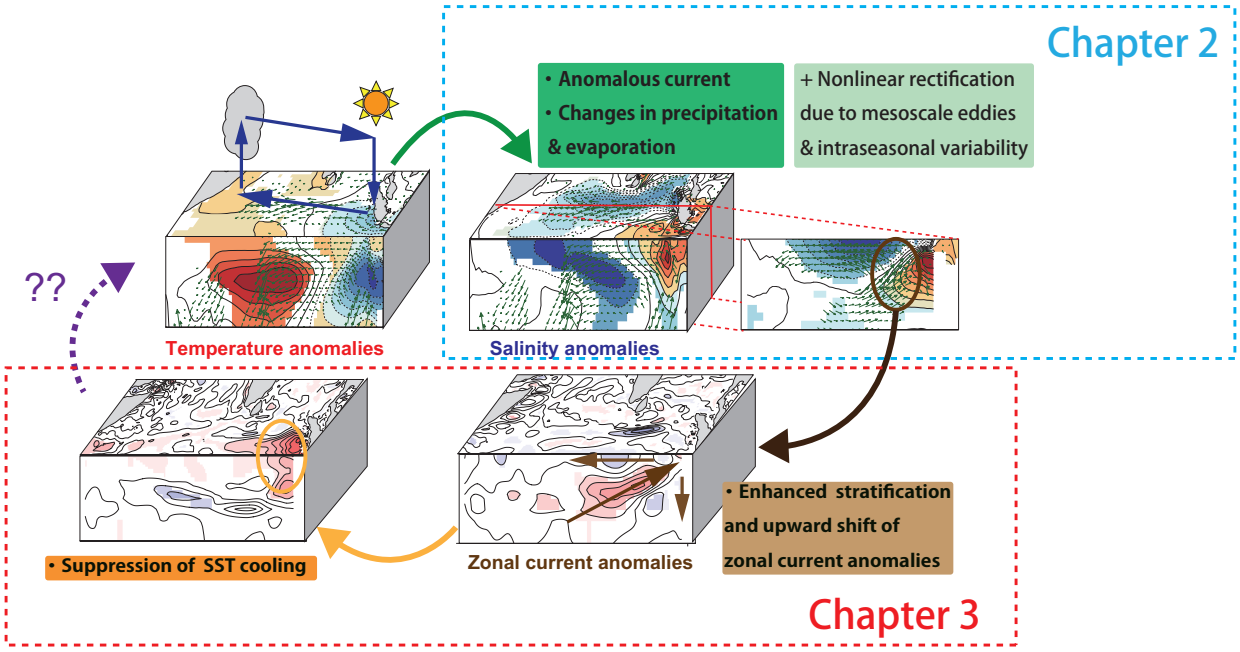

Figure 4.1: Schematic diagram illustrating the key findings obtained in the present thesis.

4.2 Discussions

One of the key findings highlighted in this thesis is the importance of rectified effects of high-frequency variability in the generation of low-frequency salinity anomalies. Even though the interactive feedback between low-frequency anomalies and eddies (e.g. storm tracks) has been shown to be critical in shaping low-frequency anomalies of the midlatitude atmosphere (Branstator, 1995; Held et al., 1989; Kushnir et al., 2002; Peng & Whitaker, 1999), less attention has been paid to such effects in the field of tropical physical oceanography. This may be due to the fact that past studies have primarily resorted to datasets with a coarse temporal resolution (e.g. data with monthly resolution) that cannot fully capture high-frequency variation. Thanks to continuing efforts, spatiotemporally finer data have been steadily accumulated recently, but the detection of such low-frequency modulation of rectified effects from observation is still very difficult at present. To accurately monitor these kinds of interesting phenomena and confirm validity of the hypothesis put

forward by the present study, long-term data with high temporal and spatial resolution is required. Continuous maintenance of satellite remote sensing of SSS as well as in-situ observational platforms (e.g. RAMA program: McPhaden et al., 2009) will be beneficial for further understanding of related physical processes (Hermes et al., 2019). In addition, similar interactions between low-frequency anomalies and high-frequency variability may also contribute to salinity variation in other regions and/or at different timescales, and further studies are needed to assess their significance.

Over the course of this study, we have only focused on the pIOD, but here we briefly touch upon the negative IOD (nIOD). During nIOD events, similar surface and subsurface salinity anomalies with the opposite sign are observed, but those anomalies are located slightly to the south and weaker than those of pIOD events. To identify the causes of associated salinity anomalies, we have carried out similar ROMS sensitivity experiments used in Chapter 2 for nIOD events (1960, 1973, 1989, 1992, 1996, 1998, and 2010), and found that the relative contribution of individual forcing is basically similar to the pIOD events. Comparison of salinity budget terms, as done in Chapter 2, also supports this idea. These results suggest that processes giving rise to salinity variations associated with the nIOD are mostly a mirror image of those associated with the pIOD, despite considerable asymmetries in the atmospheric anomalies between the two (Grunseich et al., 2011).

We have also conducted a similar series of sensitivity experiments described in Chapter 3 (i.e. the NoSADV experiments) to assess the impacts of nIOD-related salinity anomalies. Though a slight cooling in the EEIO is also generated by the nIOD-related salinity anomalies, salinity anomalies seem to play a smaller role in the nIOD compared to the pIOD. In other words, salinity anomalies serve as a negative feedback for both positive and negative IOD, but this damping effect is much greater for the pIOD than the nIOD.

It is well known that SST anomalies associated with the pIOD are generally larger than those with the nIOD (Cai et al., 2012; Hong et al., 2008), and several mechanisms are proposed to explain this asymmetry, such as a nonlinearity of SST-cloud-radiation feedback (Hong & Li, 2010), an asymmetry in thermocline feedback (Ogata et al., 2013; X.-T. Zheng et al., 2010), and nonlinear dynamical heating (Cai & Qiu, 2013; Hong et al., 2008). Since our results suggest that salinity variations tend to strongly weaken the pIOD than the nIOD events, they are not likely the major source of the positive skewness of the IOD. The relative contributions of various factors to the asymmetry of the IOD and their relationship with salinity variation will be an interesting topic for future studies.

A caveat of this study is the biases in simulated salinity. As mentioned in Chapter 2, discrepancies between model and observation are identified for both mean and anomalies of salinity, and possible culprits for such biases are inadequate representation of vertical mixing processes and uncertainty in the forcing fields. Since the mean salinity field potentially affects salinity anomalies through advective and diffusive processes, the biases in the mean state and anomalies are inseparable and seem to be intimately linked. The extent to which the model biases affects our conclusions should be further investigated using models with different configurations. More accurate atmospheric and lateral boundary forcing, a refined parameterization of subgrid-scale processes, and/or a higher horizontal/vertical resolution may improve the mean state and structure and amplitude of anomalies. Also, as our assessments of salinity anomalies are based solely on a series of sensitivity experiments using a single ocean model, it is worthwhile to re-evaluate their impacts using other ocean models. Different experimental strategies, such as adoption of data assimilation techniques, may also be useful for further deepening of our understanding on the role of salinity in the evolution of the IOD.

4.3 Impacts of this thesis and future perspectives

The primary focus of the present study is the link between salinity and the IOD. However, recent studies have reported that significant salinity variations are also caused by other climate modes, such as the ENSO (Hasson et al., 2013), the Madden-Julian Oscillation (Y. Li et al., 2015), the Atlantic zonal/meridional modes (Awo et al., 2018), and the Ningaloo Niño (Feng et al., 2015). However, investigations on the mechanisms of these interesting phenomena have just begun and further quantitative assessments are needed. The approaches adopted in this thesis, namely, the closed-salinity budget analysis and detailed decomposition of advection (Chapter 2), would be helpful to address these issues. Furthermore, if these salinity variations are attributed to changes in advective processes as for the IOD, the impacts of salinity anomalies associated with these climate modes can be quantified by applying the experimental configuration used in this study (Chapter 3). Such studies will further deepen our understanding on the role of salinity in the climate system, and may potentially contribute to improvements in the prediction skill of these climate modes.

Another interesting topic for future studies is the link between long-term variations of the IOD (Tozuka et al., 2007; Ummenhofer et al., 2017; L. Zhang et al., 2018) and those of salinity. Recently, Du et al. (2015) reported the significant freshening of the upper ocean salinity in the southeastern tropical Indian Ocean since the mid-1990s. The existence of such multidecadal variations of SSS have been subsequently reported by Y. Zhang et al. (2018) using an ocean reanalysis product. These long-term variations of salinity will alter the background conditions and potentially affect the evolution of pIOD-related anomalies. The mechanisms and influences of these low frequency variations in the mean thermohaline structure on the property of the IOD should be investigated further in future studies. We also note that the amplification of the hydrological cycle in response to global warming (Held & Soden, 2006) is anticipated to increase the contrast of the

present mean SSS (Durack & Wijffels, 2010), superimposing on the multidecadal variation. Such changes in the mean horizontal and vertical salinity gradient may modulate the pIOD-related salinity anomalies, since advection of the mean salinity gradient by the large-scale current anomalies is the dominant mechanism causing them. Thus, understanding the link between the low frequency modulation of the mean salinity and interannual salinity variability is also important for understanding the projected future changes of the IOD properties (Cai et al., 2013, 2014, 2018).

In Chapter 1, we have proposed a possibility that salinity plays an active role in air-sea coupled modes of climate variability. To obtain a clue to this formidable problem, we have investigated how salinity is affected by large-scale atmospheric anomalies, and how does it modify the upper ocean field and generate SST anomalies, with a particular focus on the pIOD. Though the oceanic adjustments involving salinity to the IOD-related atmospheric anomalies have been clearly and quantitatively elucidated in this study, we should keep in mind that it is just a prologue of the whole story of the coupled process. It should be emphasized that all sensitivity experiments in the present work have been performed using "forced" ocean models (both ROMS and LCSM), and atmospheric conditions are specified as prescribed forcing in all experiments. In the natural climate system, the atmosphere will respond to changes in SST caused by salinity anomalies, and associated adjustments may modulate wind and precipitation patterns. These altered atmospheric conditions, in turn, potentially affect the initial salinity anomalies and kick off a loop of feedback. Given that the mean SST in the EEIO is close to the critical threshold of deep atmospheric convection (which is about 28°C) (Gadgil et al., 1984; Graham & Barnett, 1987) and the impacts of salinity anomalies on SST there are about 30-60% of total anomalies associated with the IOD, such scenario is likely to occur in reality. On the other hand, a recent study using a regional coupled model suggests that salinity has negligible impacts on the mean climatic conditions in the northern Indian Ocean due to

the compensation by atmospheric adjustments (Krishnamohan et al., 2019). Whether the atmosphere-ocean coupling amplifies or damps the effects of salinity-related anomalies is an intriguing and important question that warrants further studies. Well-designed sensitivity experiments using an atmospheric general circulation model and/or a coupled general circulation model may provide useful insights into this challenging problem.

Though this study has not explicitly dealt with air-sea interaction, it does have certain implications for coupled modeling. First, it has been demonstrated that many CGCMs tend to have larger amplitude of the IOD, and SST anomalies in the EEIO extends too far to the west, compared to the observation (Cai & Cowan, 2013; L. Liu et al., 2011, 2014). Biases in mean thermocline depth in the east and associated overestimation of the Bjerknes feedback are believed to be the major culprit of these biases (Cai & Cowan, 2013; G. Li et al., 2015, 2016; L. Liu et al., 2014), but this study offers another potential factor, namely, the difference in representation of negative feedback induced by salinity variations. Since many models have large biases in the salinity field (Parekh et al., 2016; Rahaman et al., 2020), it is expected that significant biases are also found in the simulated IOD-related salinity variation. A careful intercomparison of CGCMs and quantitative assessments of each feedback are possible approaches to address this issue. If this argument holds, improved salinity fields in CGCMs may also contribute to better representation of the IOD.

Another implications of this study are directed toward predictability of coupled climate variability. Recently, several studies have demonstrated the importance of salinity assimilation in dynamical coupled forecast systems (Hackert et al., 2011, 2014, 2019; Yang et al., 2010; Zhao et al., 2014; Zhu et al., 2015; Zhu & Kumar, 2019). However, there are substantial spreads in resulting improvements in the prediction skills among the models and products used in assimilation, and physical processes behind them are not fully understood. As demonstrated in our LCSM sensitivity

experiments, the mean component of salinity and its anomalies may exert distinctive influences on the upper ocean state and the coupled response. Since most of these studies have attempted to estimate the total impacts of salinity, without explicitly isolating contributions from its mean and variable component, the resulting "impacts" are superimpositions of various effects and may be blurred by complicated interference among them. A clear separation of these effects might not to be so straightforward, but the use of "anomaly assimilation" technique (Keenlyside et al., 2008; Smith et al., 2007) would be useful for more accurate estimation of the impacts of salinity anomalies. Given that the prediction skill of the IOD is considerably lower than that of the ENSO (Luo et al., 2007; Shi et al., 2012; Wajsowicz, 2005; Wu & Tang, 2019) and its potential predictability (H. Liu et al., 2017; Zhao & Hendon, 2009), it is of great interest to investigate whether assimilation of salinity anomalies will improve its prediction skill, as for the ENSO (Zhu et al., 2015). Though careful considerations on experimental designs and their evaluations are essential, such study will open a new door to seasonal prediction of climate modes.

References

Alexander, M. A., Scott, J. D., & Deser, C. (2000). Processes that influence sea surface temperature and ocean mixed layer depth variability in a coupled model. *Journal of Geophysical Research: Oceans*, *105*(C7), 16823–16842. https://doi.org/10.1029/2000jc900074

Ando, K., & McPhaden, M. J. (1997). Variability of surface layer hydrography in the tropical Pacific Ocean. *Journal of Geophysical Research: Oceans*, *102*(C10), 23063–23078. https://doi.org/10.1029/97JC01443

Annamalai, H., Murtugudde, R., Potemra, J., Xie, S.-P., Liu, P., & Wang, B. (2003). Coupled dynamics over the Indian Ocean: spring initiation of the Zonal Mode. *Deep Sea Research Part II: Topical Studies in Oceanography*, *50*(12–13), 2305–2330. https://doi.org/10.1016/S0967-0645(03)00058-4

Awo, F. M., Alory, G., Da-Allada, C. Y., Delcroix, T., Jouanno, J., Kestenare, E., & Baloïtcha, E. (2018). Sea surface salinity signature of the tropical Atlantic interannual climatic modes. *Journal of Geophysical Research: Oceans*, *123*(10), 7420–7437. https://doi.org/10.1029/2018JC013837

Ballabrera-Poy, J., Murtugudde, R., & Busalacchi, A. J. (2002). On the potential impact of sea surface salinity observations on ENSO predictions. *Journal of Geophysical Research: Oceans*, *107*(C12), 8007. https://doi.org/10.1029/2001JC000834

Balmaseda, M. A., Vidard, A., & Anderson, D. L. T. (2008). The ECMWF ocean analysis system: ORA-S3. *Monthly Weather Review*, *136*(8), 3018–3034. https://doi.org/10.1175/2008MWR2433.1

Balmaseda, M. A., Mogensen, K., & Weaver, A. T. (2013). Evaluation of the ECMWF ocean reanalysis system ORAS4. *Quarterly Journal of the Royal Meteorological Society*, *139*(674),

1132–1161. https://doi.org/10.1002/qj.2063

Battisti, D. S., & Hirst, A. C. (1989). Interannual variability in a tropical atmosphere–ocean model: Influence of the basic state, ocean geometry and nonlinearity. *Journal of the Atmospheric Sciences*, *46*(12), 1687–1712. https://doi.org/10.1175/1520-0469(1989)046<1687:IVIATA>2.0.CO;2

Bingham, F. M., Foltz, G. R., & McPhaden, M. J. (2012). Characteristics of the seasonal cycle of surface layer salinity in the global ocean. *Ocean Science*, *8*(5), 915–929. https://doi.org/10.5194/os-8-915-2012

Bjerknes, J. (1969). Atmospheric teleconnections from the equatorial Pacific. *Monthly Weather Review*, *97*(3), 163–172. https://doi.org/10.1175/1520-0493(1969)097<0163:ATFTEP>2.3.CO;2

Boyer, T. P., Levitus, S., Antonov, J. I., Locarnini, R. A., & Garcia, H. E. (2005). Linear trends in salinity for the World Ocean, 1955–1998. *Geophysical Research Letters*, *32*(1), L01604. https://doi.org/10.1029/2004GL021791

Branstator, G. (1995). Organization of storm track anomalies by recurring low-frequency circulation anomalies. *Journal of the Atmospheric Sciences*, *52*(2), 207–226. https://doi.org/10.1175/1520-0469(1995)052<0207:OOSTAB>2.0.CO;2

Bretherton, C. S., Smith, C., & Wallace, J. M. (1992). An intercomparison of methods for finding coupled patterns in climate data. *Journal of Climate*, *5*(6), 541–560. https://doi.org/10.1175/1520-0442(1992)005<0541:aiomff>2.0.co;2

Cai, W., & Cowan, T. (2013). Why is the amplitude of the Indian Ocean Dipole overly large in CMIP3 and CMIP5 climate models? *Geophysical Research Letters*, *40*(6), 1200–1205. https://doi.org/10.1002/grl.50208

References

Cai, W., & Qiu, Y. (2013). An observation-based assessment of nonlinear feedback processes associated with the Indian Ocean Dipole. *Journal of Climate*, *26*(9), 2880–2890. https://doi.org/10.1175/JCLI-D-12-00483.1

Cai, W., Van Rensch, P., Cowan, T., & Hendon, H. H. (2012). An asymmetry in the IOD and ENSO teleconnection pathway and its impact on australian climate. *Journal of Climate*, *25*(18), 6318–6329. https://doi.org/10.1175/JCLI-D-11-00501.1

Cai, W., Zheng, X.-T., Weller, E., Collins, M., Cowan, T., Lengaigne, M., et al. (2013). Projected response of the Indian Ocean Dipole to greenhouse warming. *Nature Geoscience*, *6*(12), 999–1007. https://doi.org/10.1038/ngeo2009

Cai, W., Santoso, A., Wang, G., Weller, E., Wu, L., Ashok, K., et al. (2014). Increased frequency of extreme Indian Ocean Dipole events due to greenhouse warming. *Nature*, *510*(7504), 254–258. https://doi.org/10.1038/nature13327

Cai, W., Wang, G., Gan, B., Wu, L., Santoso, A., Lin, X., et al. (2018). Stabilised frequency of extreme positive Indian Ocean Dipole under 1.5 °C warming. *Nature Communications*, *9*(1), 1419. https://doi.org/10.1038/s41467-018-03789-6

Carton, J. A. (1991). Effect of seasonal surface freshwater flux on sea surface temperature in the tropical Atlantic Ocean. *Journal of Geophysical Research*, *96*(C7), 12593–12598. https://doi.org/10.1029/91JC01256

Carton, J. A., & Giese, B. S. (2008). A reanalysis of ocean climate using Simple Ocean Data Assimilation (SODA). *Monthly Weather Review*, *136*(8), 2999–3017. https://doi.org/10.1175/2007MWR1978.1

Chang, P., Ji, L., & Li, H. (1997). A decadal climate variation in the tropical Atlantic Ocean from thermodynamic air-sea interactions. *Nature*, *385*(6616), 516–518.

https://doi.org/10.1038/385516a0

Chen, G., Han, W., Li, Y., Wang, D., & McPhaden, M. J. (2015). Seasonal-to-interannual time scale dynamics of the Equatorial Undercurrent in the Indian Ocean. *Journal of Physical Oceanography*, *45*(6), 1532–1553. https://doi.org/10.1175/JPO-D-14-0225.1

Chen, G., Han, W., Li, Y., & Wang, D. (2016). Interannual variability of equatorial eastern Indian Ocean upwelling: local versus remote forcing. *Journal of Physical Oceanography*, *46*(3), 789–807. https://doi.org/10.1175/JPO-D-15-0117.1

Chen, G., Han, W., Shu, Y., Li, Y., Wang, D., & Xie, Q. (2016). The role of Equatorial Undercurrent in sustaining the eastern Indian Ocean upwelling. *Geophysical Research Letters*, *43*(12), 6444–6451. https://doi.org/10.1002/2016GL069433

Chowdary, J. S., Gnanaseelan, C., & Xie, S.-P. (2009). Westward propagation of barrier layer formation in the 2006–07 Rossby wave event over the tropical southwest Indian Ocean. *Geophysical Research Letters*, *36*(4), L04607. https://doi.org/10.1029/2008GL036642

Cooper, N. S. (1988). The effect of salinity on tropical ocean models. *Journal of Physical Oceanography*, *18*, 697–707. https://doi.org/10.1175/1520-0485(1988)018<0697:TEOSOT>2.0.CO;2

Cravatte, S., Delcroix, T., Zhang, D., McPhaden, M. J., & Leloup, J. (2009). Observed freshening and warming of the western Pacific Warm Pool. *Climate Dynamics*, *33*(4), 565–589. https://doi.org/10.1007/s00382-009-0526-7

Cronin, M. F., & McPhaden, M. J. (2002). Barrier layer formation during westerly wind bursts. *Journal of Geophysical Research: Oceans*, *107*(C12), 8020. https://doi.org/10.1029/2001JC001171

Currie, J. C., Lengaigne, M., Vialard, J., Kaplan, D. M., Aumont, O., Naqvi, S. W. A., & Maury, O.

References

(2013). Indian Ocean Dipole and El Niño/Southern Oscillation impacts on regional chlorophyll anomalies in the Indian Ocean. *Biogeosciences*, *10*(10), 6677–6698. https://doi.org/10.5194/bg-10-6677-2013

Czaja, A., & Frankignoul, C. (2002). Observed impact of Atlantic SST anomalies on the North Atlantic Oscillation. *Journal of Climate*, *15*(6), 606–623. https://doi.org/10.1175/1520-0442(2002)015<0606:OIOASA>2.0.CO;2

Dee, D. P., Uppala, S. M., Simmons, A. J., Berrisford, P., Poli, P., Kobayashi, S., et al. (2011). The ERA-Interim reanalysis: configuration and performance of the data assimilation system. *Quarterly Journal of the Royal Meteorological Society*, *137*(656), 553–597. https://doi.org/10.1002/qj.828

Delcroix, T., & Hénin, C. (1991). Seasonal and interannual variations of sea surface salinity in the tropical Pacific Ocean. *Journal of Geophysical Research*, *96*(C12), 22135. https://doi.org/10.1029/91JC02124

Delcroix, T., Chaigneau, A., Soviadan, D., Boutin, J., & Pegliasco, C. (2019). Eddy-induced salinity changes in the tropical Pacific. *Journal of Geophysical Research: Oceans*, *124*(1), 374–389. https://doi.org/10.1029/2018JC014394

Delman, A. S., McClean, J. L., Sprintall, J., Talley, L. D., & Bryan, F. O. (2018). Process-specific contributions to anomalous Java mixed layer cooling during positive IOD events. *Journal of Geophysical Research: Oceans*, *123*(6), 4153–4176. https://doi.org/https://doi.org/10.1029/2017JC013749

Deser, C., Alexander, M. A., Xie, S., & Phillips, A. S. (2010). Sea surface temperature variability: patterns and mechanisms. *Annual Review of Marine Science*, *2*(1), 115–143. https://doi.org/10.1146/annurev-marine-120408-151453

Drushka, K., Gille, S. T., & Sprintall, J. (2014). The diurnal salinity cycle in the tropics. *Journal of Geophysical Research: Oceans*, *119*(9), 5874–5890. https://doi.org/10.1002/2014JC009924

Du, Y., & Zhang, Y. (2015). Satellite and Argo observed surface salinity variations in the tropical Indian Ocean and their association with the Indian Ocean Dipole mode. *Journal of Climate*, *28*(2), 695–713. https://doi.org/10.1175/JCLI-D-14-00435.1

Du, Y., Cai, W., & Wu, Y. (2013). A new type of the Indian Ocean Dipole since the mid-1970s. *Journal of Climate*, *26*(3), 959–972. https://doi.org/10.1175/JCLI-D-12-00047.1

Du, Y., Zhang, Y., Feng, M., Wang, T., Zhang, N., & Wijffels, S. E. (2015). Decadal trends of the upper ocean salinity in the tropical Indo-Pacific since mid-1990s. *Scientific Reports*, *5*, 16050. https://doi.org/10.1038/srep16050

Duchon, C. E. (1979). Lanczos filtering in one and two dimensions. *Journal of Applied Meteorology*, *18*(8), 1016–1022. https://doi.org/10.1175/1520-0450(1979)018<1016:LFIOAT>2.0.CO;2

Duncan, B., & Han, W. (2012). Influence of atmospheric intraseasonal oscillations on seasonal and interannual variability in the upper Indian Ocean. *Journal of Geophysical Research: Oceans*, *117*(C11). https://doi.org/10.1029/2012JC008190

Durack, P. J., & Wijffels, S. E. (2010). Fifty-year trends in global ocean salinities and their relationship to broad-scale warming. *Journal of Climate*, *23*(16), 4342–4362. https://doi.org/10.1175/2010JCLI3377.1

Durack, P. J., Wijffels, S. E., & Matear, R. J. (2012). Ocean salinities reveal strong global water cycle intensification during 1950 to 2000. *Science*, *336*(6080), 455–458. https://doi.org/10.1126/science.1212222

Durack, P. J., Wijffels, S. E., & Boyer, T. P. (2013). Long-term salinity changes and implications for the global water cycle. In *International Geophysics* (2nd ed., Vol. 103, pp. 727–757). Elsevier

Ltd. https://doi.org/10.1016/B978-0-12-391851-2.00028-3

Durand, F., Alory, G., Dussin, R., & Reul, N. (2013). SMOS reveals the signature of Indian Ocean Dipole events. *Ocean Dynamics*, *63*(11–12), 1203–1212. https://doi.org/10.1007/s10236-013-0660-y

Fairall, C. W., Bradley, E. F., Hare, J. E., Grachev, A. A., & Edson, J. B. (2003). Bulk parameterization of air-sea fluxes: Updates and verification for the COARE algorithm. *Journal of Climate*, *16*(4), 571–591. https://doi.org/10.1175/1520-0442(2003)016<0571:BPOASF>2.0.CO;2

Feng, M., & Wijffels, S. E. (2002). Intraseasonal variability in the South Equatorial Current of the east Indian Ocean. *Journal of Physical Oceanography*, *32*(1), 265–277. https://doi.org/10.1175/1520-0485(2002)032<0265:IVITSE>2.0.CO;2

Feng, M., McPhaden, M. J., Xie, S.-P., & Hafner, J. (2013). La Niña forces unprecedented Leeuwin Current warming in 2011. *Scientific Reports*, *3*(1), 1277. https://doi.org/10.1038/srep01277

Feng, M., Benthuysen, J., Zhang, N., & Slawinski, D. (2015). Freshening anomalies in the Indonesian throughflow and impacts on the Leeuwin Current during 2010-2011. *Geophysical Research Letters*, *42*(20), 8555–8562. https://doi.org/10.1002/2015GL065848

Fukumori, I., Raghunath, R., & Fu, L.-L. (1998). Nature of global large-scale sea level variability in relation to atmospheric forcing: A modeling study. *Journal of Geophysical Research: Oceans*, *103*(C3), 5493–5512. https://doi.org/10.1029/97jc02907

Furuichi, N., Hibiya, T., & Niwa, Y. (2012). Assessment of turbulence closure models for resonant inertial response in the oceanic mixed layer using a large eddy simulation model. *Journal of Oceanography*, *68*(2), 285–294. https://doi.org/10.1007/s10872-011-0095-3

Gadgil, S., Joseph, P. V., & Joshi, N. V. (1984). Ocean–atmosphere coupling over monsoon regions.

Nature, *312*(5990), 141–143. https://doi.org/10.1038/312141a0

Godfrey, S., & Lindstrom, E. (1989). The heat budget of the equatorial western Pacific surface mixed layer. *Journal of Geophysical Research*, *94*(C6), 8007. https://doi.org/10.1029/JC094iC06p08007

Graham, N. E., & Barnett, T. P. (1987). Sea surface temperature, surface wind divergence, and convection over tropical oceans. *Science*, *238*(4827), 657–659. https://doi.org/10.1126/science.238.4827.657

Grunseich, G., Subrahmanyam, B., Murty, V. S. N., & Giese, B. S. (2011). Sea surface salinity variability during the Indian Ocean Dipole and ENSO events in the tropical Indian Ocean. *Journal of Geophysical Research*, *116*(C11), C11013. https://doi.org/10.1029/2011JC007456

Hackert, E., Ballabrera-Poy, J., Busalacchi, A. J., Zhang, R.-H., & Murtugudde, R. (2011). Impact of sea surface salinity assimilation on coupled forecasts in the tropical Pacific. *Journal of Geophysical Research: Oceans*, *116*(5), 1–18. https://doi.org/10.1029/2010JC006708

Hackert, E., Busalacchi, A. J., & Ballabrera-Poy, J. (2014). Impact of Aquarius sea surface salinity observations on coupled forecasts for the tropical Indo-Pacific Ocean. *Journal of Geophysical Research: Oceans*, *119*(7), 4045–4067. https://doi.org/10.1002/2013JC009697

Hackert, E., Kovach, R. M., Busalacchi, A. J., & Ballabrera-Poy, J. (2019). Impact of Aquarius and SMAP satellite sea surface salinity observations on coupled El Niño/Southern Oscillation forecasts. *Journal of Geophysical Research: Oceans*, *124*(7), 2019JC015130. https://doi.org/10.1029/2019JC015130

Halkides, D. J., & Lee, T. (2009). Mechanisms controlling seasonal-to-interannual mixed layer temperature variability in the southeastern tropical Indian Ocean. *Journal of Geophysical Research*, *114*(C2), C02012. https://doi.org/10.1029/2008JC004949

References

Han, W., & McCreary, J. P. (2001). Modeling salinity distributions in the Indian Ocean. *Journal of Geophysical Research: Oceans*, *106*(C1), 859–877. https://doi.org/10.1029/2000JC000316

Han, W., McCreary, J. P., & Kohler, K. E. (2001). Influence of precipitation minus evaporation and Bay of Bengal rivers on dynamics, thermodynamics, and mixed layer physics in the upper Indian Ocean. *Journal of Geophysical Research: Oceans*, *106*(C4), 6895–6916. https://doi.org/10.1029/2000JC000403

Han, W., Webster, P. J., Lukas, R., Hacker, P., & Hu, A. (2004). Impact of atmospheric intraseasonal variability in the Indian Ocean: Low-frequency rectification in equatorial surface current and transport. *Journal of Physical Oceanography*, *34*(6), 1350–1372. https://doi.org/10.1175/1520-0485(2004)034<1350:IOAIVI>2.0.CO;2

Hartmann, D. L. (2016). *Global Physical Climatology*. *Global Physical Climatology: Second Edition*. Elsevier. https://doi.org/10.1016/C2009-0-00030-0

Hasson, A. E. A., Delcroix, T., & Dussin, R. (2013). An assessment of the mixed layer salinity budget in the tropical Pacific Ocean. Observations and modelling (1990-2009). *Ocean Dynamics*, *63*(2–3), 179–194. https://doi.org/10.1007/s10236-013-0596-2

Held, I. M., & Soden, B. J. (2006). Robust responses of the hydrological cycle to global warming. *Journal of Climate*, *19*(21), 5686–5699. https://doi.org/10.1175/JCLI3990.1

Held, I. M., Lyons, S. W., & Nigam, S. (1989). Transients and the extratropical response to El Niño. *Journal of the Atmospheric Sciences*, *46*(1), 163–174. https://doi.org/10.1175/1520-0469(1989)046<0163:TATERT>2.0.CO;2

Hermes, J. C., Masumoto, Y., Beal, L. M., Roxy, M. K., Vialard, J., Andres, M., et al. (2019). A sustained ocean observing system in the Indian Ocean for climate related scientific knowledge and societal needs. *Frontiers in Marine Science*, *6*. https://doi.org/10.3389/fmars.2019.00355

Hirst, A. C. (1986). Unstable and damped equatorial modes in simple coupled ocean- atmosphere models. *Journal of the Atmospheric Sciences*, *43*(6), 606–630. https://doi.org/10.1175/1520-0469(1986)043<0606:uademi>2.0.co;2

Hong, C.-C., & Li, T. (2010). Independence of SST skewness from thermocline feedback in the eastern equatorial Indian Ocean. *Geophysical Research Letters*, *37*, L11702. https://doi.org/10.1029/2010GL043380

Hong, C.-C., Li, T., LinHo, & Kug, J.-S. (2008). Asymmetry of the Indian Ocean Dipole. Part I: Observational analysis. *Journal of Climate*, *21*(18), 4834–4848. https://doi.org/10.1175/2008JCLI2222.1

Horel, J. D., & Wallace, J. M. (1981). Planetary-scale atmospheric phenomena associated with the Southern Oscillation. *Monthly Weather Review*, *109*(4), 813–829. https://doi.org/10.1175/1520-0493(1981)109<0813:PSAPAW>2.0.CO;2

Hosoda, S., Ohira, T., & Nakamura, T. (2008). A monthly mean dataset of global oceanic temperature and salinity derived from Argo float observations. *JAMSTEC Report of Research and Development*, *8*(November), 47–59. https://doi.org/10.5918/jamstecr.8.47

Hosoda, S., Suga, T., Shikama, N., & Mizuno, K. (2009). Global surface layer salinity change detected by Argo and its implication for hydrological cycle intensification. *Journal of Oceanography*, *65*(4), 579–586. https://doi.org/10.1007/s10872-009-0049-1

Howden, S. D., & Murtugudde, R. (2001). Effects of river inputs into the Bay of Bengal. *Journal of Geophysical Research: Oceans*, *106*(C9), 19825–19843. https://doi.org/10.1029/2000jc000656

Jin, F.-F. (1997). An equatorial ocean recharge paradigm for ENSO. Part I: Conceptual model. *Journal of the Atmospheric Sciences*, *54*(7), 811–829. https://doi.org/10.1175/1520-0469(1997)054<0811:AEORPF>2.0.CO;2

References

Kataoka, T., Tozuka, T., Behera, S. K., & Yamagata, T. (2014). On the Ningaloo Nino/Nina. *Climate Dynamics*, *43*, 1463–1482. https://doi.org/10.1007/s00382-013-1961-z

Kataoka, T., Kimoto, M., Watanabe, M., & Tatebe, H. (2019). Wind–Mixed Layer–SST feedbacks in a tropical air–sea coupled system: Application to the Atlantic. *Journal of Climate*, *32*(13), 3865–3881. https://doi.org/10.1175/JCLI-D-18-0728.1

Katsura, S., Oka, E., Qiu, B., & Schneider, N. (2013). Formation and subduction of North Pacific Tropical Water and their interannual variability. *Journal of Physical Oceanography*, *43*(11), 2400–2415. https://doi.org/10.1175/JPO-D-13-031.1

Keenlyside, N. (2002). Annual cycle of equatorial zonal currents in the Pacific. *Journal of Geophysical Research*, *107*(C8), 3093. https://doi.org/10.1029/2000JC000711

Keenlyside, N., Latif, M., Jungclaus, J., Kornblueh, L., & Roeckner, E. (2008). Advancing decadal-scale climate prediction in the North Atlantic sector. *Nature*, *453*(7191), 84–88. https://doi.org/10.1038/nature06921

Keerthi, M. G., Lengaigne, M., Vialard, J., de Boyer Montégut, C., & Muraleedharan, P. M. (2013). Interannual variability of the tropical Indian Ocean mixed layer depth. *Climate Dynamics*, *40*(3–4), 743–759. https://doi.org/10.1007/s00382-012-1295-2

Kido, S., & Tozuka, T. (2017). Salinity variability associated with the positive Indian Ocean Dipole and its impact on the upper ocean temperature. *Journal of Climate*, *30*(19), 7885–7907. https://doi.org/10.1175/JCLI-D-17-0133.1

Klein, S. A., & Hartmann, D. L. (1993). The seasonal cycle of low stratiform clouds. *Journal of Climate*, *6*(8), 1587–1606. https://doi.org/10.1175/1520-0442(1993)006<1587:TSCOLS>2.0.CO;2

Köhler, J., Serra, N., Bryan, F. O., Johnson, B. K., & Stammer, D. (2018). Mechanisms of

mixed-layer salinity seasonal variability in the Indian Ocean. *Journal of Geophysical Research: Oceans*, *123*(1), 466–496. https://doi.org/10.1002/2017JC013640

Krishnamohan, K. S., Vialard, J., Lengaigne, M., Masson, S., Samson, G., Pous, S., et al. (2019). Is there an effect of Bay of Bengal salinity on the northern Indian Ocean climatological rainfall? *Deep Sea Research Part II: Topical Studies in Oceanography*, *166*, 19–33. https://doi.org/10.1016/j.dsr2.2019.04.003

Kummerow, C., Barnes, W., Kozu, T., Shiue, J., & Simpson, J. (1998). The Tropical Rainfall Measuring Mission (TRMM) sensor package. *Journal of Atmospheric and Oceanic Technology*, *15*(3), 809–817. https://doi.org/10.1175/1520-0426(1998)015<0809:TTRMMT>2.0.CO;2

Kushnir, Y., Robinson, W. A., Bladé, I., Hall, N. M. J., Peng, S., & Sutton, R. (2002). Atmospheric GCM response to extratropical SST anomalies: Synthesis and evaluation. *Journal of Climate*, *15*(16), 2233–2256. https://doi.org/10.1175/1520-0442(2002)015<2233:AGRTES>2.0.CO;2

Lee, C., Minobe, S., & Sasaki, Y. N. (2018). Origin of intraseasonal variability in the eastern equatorial Indian Ocean: intrinsic variability and local and remote wind stress forcings. *Journal of Oceanography*. https://doi.org/10.1007/s10872-018-0489-6

Lee, T., Lagerloef, G., Gierach, M. M., Kao, H. Y., Yueh, S., & Dohan, K. (2012). Aquarius reveals salinity structure of tropical instability waves. *Geophysical Research Letters*, *39*(12), 1–6. https://doi.org/10.1029/2012GL052232

Li, G., Xie, S.-P., & Du, Y. (2015). Monsoon-induced biases of climate models over the tropical Indian Ocean. *Journal of Climate*, *28*(8), 3058–3072. https://doi.org/10.1175/JCLI-D-14-00740.1

Li, G., Xie, S.-P., & Du, Y. (2016). A robust but spurious pattern of climate change in model projections over the tropical Indian Ocean. *Journal of Climate*, *29*(15), 5589–5608.

https://doi.org/10.1175/JCLI-D-15-0565.1

Li, J., Liang, C., Tang, Y., Dong, C., Chen, D., Liu, X., & Jin, W. (2016). A new dipole index of the salinity anomalies of the tropical Indian Ocean. *Scientific Reports*, *6*(1), 24260. https://doi.org/10.1038/srep24260

Li, J., Liang, C., Tang, Y., Liu, X., Lian, T., Shen, Z., & Li, X. (2018). Impacts of the IOD-associated temperature and salinity anomalies on the intermittent equatorial undercurrent anomalies. *Climate Dynamics*, *51*(4), 1391–1409. https://doi.org/10.1007/s00382-017-3961-x

Li, T., & Philander, S. G. H. (1996). On the annual cycle of the eastern equatorial Pacific. *Journal of Climate*. https://doi.org/10.1175/1520-0442(1996)009<2986:OTACOT>2.0.CO;2

Li, T., Hogan, T. F., & Chang, C.-P. (2000). Dynamic and thermodynamic regulation of ocean warming. *Journal of the Atmospheric Sciences*, *57*(20), 3353–3365. https://doi.org/10.1175/1520-0469(2000)057<3353:DATROO>2.0.CO;2

Li, T., Zhang, Y., Lu, E., & Wang, D. (2002). Relative role of dynamic and thermodynamic processes in the development of the Indian Ocean Dipole: An OGCM diagnosis. *Geophysical Research Letters*, *29*(23), 25-1-25–4. https://doi.org/10.1029/2002GL015789

Li, T., Wang, B., Chang, C.-P., & Zhang, Y. (2003). A theory for the Indian Ocean dipole–zonal mode. *Journal of the Atmospheric Sciences*, *60*(17), 2119–2135. https://doi.org/10.1175/1520-0469(2003)060<2119:ATFTIO>2.0.CO;2

Li, Y., Han, W., Shinoda, T., Wang, C., Lien, R. C., Moum, J. N., & Wang, J.-W. (2013). Effects of the diurnal cycle in solar radiation on the tropical Indian Ocean mixed layer variability during wintertime Madden-Julian Oscillations. *Journal of Geophysical Research: Oceans*, *118*(10), 4945–4964. https://doi.org/10.1002/jgrc.20395

Li, Y., Han, W., & Lee, T. (2015). Intraseasonal sea surface salinity variability in the equatorial

Indo-Pacific Ocean induced by Madden-Julian Oscillations. *Journal of Geophysical Research: Oceans*, *120*(3), 2233–2258. https://doi.org/10.1002/2014JC010647

Liu, H., Tang, Y., Chen, D., & Lian, T. (2017). Predictability of the Indian Ocean Dipole in the coupled models. *Climate Dynamics*, *48*(5–6), 2005–2024. https://doi.org/10.1007/s00382-016-3187-3

Liu, L., Yu, W., & Li, T. (2011). Dynamic and thermodynamic air–sea coupling associated with the Indian Ocean Dipole diagnosed from 23 WCRP CMIP3 Models. *Journal of Climate*, *24*(18), 4941–4958. https://doi.org/10.1175/2011JCLI4041.1

Liu, L., Xie, S.-P., Zheng, X.-T., Li, T., Du, Y., Huang, G., & Yu, W. (2014). Indian Ocean variability in the CMIP5 multi-model ensemble: the zonal dipole mode. *Climate Dynamics*, *43*(5–6), 1715–1730. https://doi.org/10.1007/s00382-013-2000-9

Lukas, R., & Lindstrom, E. (1991). The mixed layer of the western equatorial Pacific Ocean. *Journal of Geophysical Research*, *96*(S01), 3343–3357. https://doi.org/10.1029/90JC01951

Luo, J., Masson, S., Behera, S. K., & Yamagata, T. (2007). Experimental forecasts of the Indian Ocean Dipole using a coupled OAGCM. *Journal of Climate*, *20*(10), 2178–2190. https://doi.org/10.1175/JCLI4132.1

Maes, C. (2002). Salinity barrier layer and onset of El Niño in a Pacific coupled model. *Geophysical Research Letters*, *29*(24), 2206. https://doi.org/10.1029/2002GL016029

Maes, C., Picaut, J., & Belamari, S. (2005). Importance of the salinity barrier layer for the buildup of El Niño. *Journal of Climate*, *18*(1), 104–118. https://doi.org/10.1175/JCLI-3214.1

Marchesiello, P., McWilliams, J. C., & Shchepetkin, A. (2001). Open boundary conditions for long-term integration of regional oceanic models. *Ocean Modelling*, *3*(1–2), 1–20. https://doi.org/10.1016/S1463-5003(00)00013-5

References

Masson, S., Menkes, C., Delecluse, P., & Boulanger, J.-P. (2003). Impacts of salinity on the eastern Indian Ocean during the termination of the fall Wyrtki Jet. *Journal of Geophysical Research*, *108*(C3), 1–22. https://doi.org/10.1029/2001JC000833

Masson, S., Boulanger, J.-P., Menkes, C., Delecluse, P., & Yamagata, T. (2004). Impact of salinity on the 1997 Indian Ocean dipole event in a numerical experiment. *Journal of Geophysical Research*, *109*(C2), C02002. https://doi.org/10.1029/2003JC001807

Masson, S., Luo, J., Madec, G., Vialard, J., Durand, F., Gualdi, S., et al. (2005). Impact of barrier layer on winter-spring variability of the southeastern Arabian Sea. *Geophysical Research Letters*, *32*(7), 1–4. https://doi.org/10.1029/2004GL021980

Masumoto, Y., & Meyers, G. (1998). Forced Rossby waves in the southern tropical Indian Ocean. *Journal of Geophysical Research: Oceans*, *103*(C12), 27589–27602. https://doi.org/10.1029/98JC02546

McCreary, J. P. (1980). *Modeling wind-driven ocean circulation*.

McCreary, J. P. (1981). A Linear Stratified Ocean Model of the Coastal Undercurrent. *Philosophical Transactions of the Royal Society A: Mathematical, Physical and Engineering Sciences*, *302*(1469), 385–413. https://doi.org/10.1098/rsta.1981.0176

McPhaden, M. J., Zebiak, S. E., & Glantz, M. H. (2006). ENSO as an Integrating Concept in Earth Science. *Science*, *314*(5806), 1740–1745. https://doi.org/10.1126/science.1132588

McPhaden, M. J., Meyers, G., Ando, K., Masumoto, Y., Murty, V. S. N., Ravichandran, M., et al. (2009). Supplement to RAMA: The Research Moored Array for African—Asian—Australian monsoon analysis and prediction. *Bulletin of the American Meteorological Society*, *90*(4), ES5–ES8. https://doi.org/10.1175/2008BAMS2608.2

Melnichenko, O., Amores, A., Maximenko, N., Hacker, P., & Potemra, J. (2017). Signature of

mesoscale eddies in satellite sea surface salinity data. *Journal of Geophysical Research: Oceans*, *122*(2), 1416–1424. https://doi.org/10.1002/2016JC012420

Miller, J. R. (1976). The salinity effect in a mixed layer ocean model. *Journal of Physical Oceanography*, *6*(1), 29–35. https://doi.org/10.1175/1520-0485(1976)006<0029:TSEIAM>2.0.CO;2

Miyama, T., McCreary, J. P., Jensen, T. G., Loschnigg, J., Godfrey, S., & Ishida, A. (2003). Structure and dynamics of the Indian-Ocean cross-equatorial cell. *Deep Sea Research Part II: Topical Studies in Oceanography*, *50*(12–13), 2023–2047. https://doi.org/10.1016/S0967-0645(03)00044-4

Miyama, T., McCreary, J. P., Sengupta, D., & Senan, R. (2006). Dynamics of biweekly oscillations in the equatorial Indian Ocean. *Journal of Physical Oceanography*, *36*(5), 827–846. https://doi.org/10.1175/JPO2897.1

Morioka, Y., Tozuka, T., & Yamagata, T. (2010). Climate variability in the southern Indian Ocean as revealed by self-organizing maps. *Climate Dynamics*, *35*(6), 1075–1088. https://doi.org/10.1007/s00382-010-0843-x

Murtugudde, R. R., & Busalacchi, A. J. (1998). Salinity effects in a tropical ocean model. *Journal of Geophysical Research: Oceans*, *103*(C2), 3283–3300. https://doi.org/10.1029/97JC02438

Murtugudde, Raghu, McCreary, J. P., & Busalacchi, A. J. (2000). Oceanic processes associated with anomalous events in the Indian Ocean with relevance to 1997-1998. *Journal of Geophysical Research: Oceans*, *105*(C2), 3295–3306. https://doi.org/10.1029/1999JC900294

Murtugudde, Ragu, & Busalacchi, A. J. (1999). Interannual variability of the dynamics and thermodynamics of the tropical Indian Ocean. *Journal of Climate*, *12*(8), 2300–2326. https://doi.org/10.1175/1520-0442(1999)012<2300:IVOTDA>2.0.CO;2

References

Nagura, M., & McPhaden, M. J. (2010). Dynamics of zonal current variations associated with the Indian Ocean Dipole. *Journal of Geophysical Research*, *115*(C11), C11026. https://doi.org/10.1029/2010JC006423

Nagura, M., Masumoto, Y., & Horii, T. (2014). Meridional heat advection due to mixed Rossby gravity waves in the e quatorial Indian Ocean. *Journal of Physical Oceanography*, *44*(1), 343–358. https://doi.org/10.1175/JPO-D-13-0141.1

Neelin, J. D., Battisti, D. S., Hirst, A. C., Jin, F.-F., Wakata, Y., Yamagata, T., & Zebiak, S. E. (1998). ENSO theory. *Journal of Geophysical Research: Oceans*, *103*(C7), 14261–14290. https://doi.org/10.1029/97JC03424

Nyadjro, E. S., & McPhaden, M. J. (2014). Variability of zonal currents in the eastern equatorial Indian Ocean on seasonal to interannual time scales. *Journal of Geophysical Research: Oceans*, *119*(11), 7969–7986. https://doi.org/10.1002/2014JC010380

Ogata, T., & Masumoto, Y. (2010). Interactions between mesoscale eddy variability and Indian Ocean Dipole events in the southeastern tropical Indian Ocean - Case studies for 1994 and 1997/1998. *Ocean Dynamics*, *60*(3), 717–730. https://doi.org/10.1007/s10236-010-0304-4

Ogata, T., Xie, S.-P., Lan, J., & Zheng, X.-T. (2013). Importance of ocean dynamics for the skewness of the Indian Ocean Dipole mode. *Journal of Climate*, *26*(7), 2145–2159. https://doi.org/10.1175/JCLI-D-11-00615.1

Ogata, T., Nagura, M., & Masumoto, Y. (2017). Mean subsurface upwelling induced by intraseasonal variability over the equatorial Indian Ocean. *Journal of Physical Oceanography*, *47*(6), 1347–1365. https://doi.org/10.1175/JPO-D-16-0257.1

Parekh, A., Chowdary, J. S., Sayantani, O., Fousiya, T. S., & Gnanaseelan, C. (2016). Tropical Indian Ocean surface salinity bias in climate forecasting system coupled models and the role of

upper ocean processes. *Climate Dynamics*, *46*(7–8), 2403–2422. https://doi.org/10.1007/s00382-015-2709-8

Paulson, C. A., & Simpson, J. J. (1977). Irradiance measurements in the upper ocean. *Journal of Physical Oceanography*, *7*(6), 952–956. https://doi.org/10.1175/1520-0485(1977)007<0952:IMITUO>2.0.CO;2

Peng, S., & Whitaker, J. S. (1999). Mechanisms determining the atmospheric response to midlatitude SST anomalies. *Journal of Climate*, *12*(5), 1393–1408. https://doi.org/10.1175/1520-0442(1999)012<1393:MDTART>2.0.CO;2

Philander, S. G. H. (1990). *El Nino, La Nina, and the Southern Oscillation*. *International Geophysics Vol 46*. Academic Press.

Philander, S. G. H., Yamagata, T., & Pacanowski, R. C. (1984). Unstable air-sea interactions in the tropics. *Journal of the Atmospheric Sciences*, *41*(4), 604–613. https://doi.org/10.1175/1520-0469(1984)041<0604:UASIIT>2.0.CO;2

Picaut, J., Ioualalen, M., Menkes, C., Delcroix, T., & McPhaden, M. J. (1996). Mechanism of the zonal displacements of the Pacific warm pool: Implications for ENSO. *Science*, *274*(5292), 1486–1489. https://doi.org/10.1126/science.274.5292.1486

Qiu, Y., Cai, W., Li, L., & Guo, X. (2012). Argo profiles variability of barrier layer in the tropical Indian Ocean and its relationship with the Indian Ocean Dipole. *Geophysical Research Letters*, *39*, L08605. https://doi.org/10.1029/2012GL051441

Qu, T., & Meyers, G. (2005). Seasonal variation of barrier layer in the southeastern tropical Indian Ocean. *Journal of Geophysical Research*, *110*(C11), C11003. https://doi.org/10.1029/2004JC002816

Rahaman, H., Srinivasu, U., Panickal, S., Durgadoo, J. V., Griffies, S. M., Ravichandran, M., et al.

References

(2020). An assessment of the Indian Ocean mean state and seasonal cycle in a suite of interannual CORE-II simulations. *Ocean Modelling*, *145*, 101503. https://doi.org/10.1016/j.ocemod.2019.101503

Ramanathan, V., & Collins, W. (1991). Thermodynamic regulation of ocean warming by cirrus clouds deduced from observations of the 1987 El Niño. *Nature*, *351*(6321), 27–32. https://doi.org/10.1038/351027a0

Rao, R. R., & Sivakumar, R. (2003). Seasonal variability of sea surface salinity and salt budget of the mixed layer of the north Indian Ocean. *Journal of Geophysical Research*, *108*(C1), 3009. https://doi.org/10.1029/2001JC000907

Rao, S. A., & Behera, S. K. (2005). Subsurface influence on SST in the tropical Indian Ocean: Structure and interannual variability. *Dynamics of Atmospheres and Oceans*, *39*, 103–135. https://doi.org/10.1016/j.dynatmoce.2004.10.014

Rao, S. A., & Yamagata, T. (2004). Abrupt termination of Indian Ocean dipole events in response to intraseasonal disturbances. *Geophysical Research Letters*, *31*(19), L19306. https://doi.org/10.1029/2004GL020842

Rao, S. A., Behera, S. K., Masumoto, Y., & Yamagata, T. (2002). Interannual subsurface variability in the tropical Indian Ocean with a special emphasis on the Indian Ocean Dipole. *Deep Sea Research Part II: Topical Studies in Oceanography*, *49*(7–8), 1549–1572. https://doi.org/10.1016/S0967-0645(01)00158-8

Ren, L., & Riser, S. C. (2009). Seasonal salt budget in the northeast Pacific Ocean. *Journal of Geophysical Research*, *114*(C12), C12004. https://doi.org/10.1029/2009JC005307

Richter, I., Behera, S. K., Masumoto, Y., Taguchi, B., Komori, N., & Yamagata, T. (2010). On the triggering of Benguela Niños: Remote equatorial versus local influences. *Geophysical Research*

Letters, *37*, L20604. https://doi.org/10.1029/2010GL044461

Roemmich, D., & Gilson, J. (2009). The 2004-2008 mean and annual cycle of temperature, salinity, and steric height in the global ocean from the Argo Program. *Progress in Oceanography*, *82*(2), 81–100. https://doi.org/10.1016/j.pocean.2009.03.004

Saji, N. H., & Yamagata, T. (2003). Possible impacts of Indian Ocean Dipole mode events on global climate. *Climate Research*, *25*(2), 151–169. https://doi.org/10.3354/cr025151

Saji, N. H., Goswami, B. N., Vinayachandran, P. N., & Yamagata, T. (1999). A dipole mode in the tropical Indian Ocean. *Nature*, *401*(6751), 360–363. https://doi.org/10.1038/43854

Schopf, P. S., & Suarez, M. J. (1988). Vacillations in a coupled ocean–atmosphere model. *Journal of the Atmospheric Sciences*, *45*(3), 549–566. https://doi.org/10.1175/1520-0469(1988)045<0549:VIACOM>2.0.CO;2

Schott, F. A., Xie, S.-P., & McCreary, J. P. (2009). Indian Ocean circulation and climate variability. *Reviews of Geophysics*, *47*(1), RG1002. https://doi.org/10.1029/2007RG000245

Sengupta, D., Senan, R., Murty, V. S. N., & Fernando, V. (2004). A biweekly mode in the equatorial Indian Ocean. *Journal of Geophysical Research*, *109*(C10), C10003. https://doi.org/10.1029/2004JC002329

Shannon, L. V., Boyd, A. J., Brundrit, G. B., & Taunton-Clark, J. (1986). On the existence of an El Niño-type phenomenon in the Benguela System. *Journal of Marine Research*, *44*(3), 495–520. https://doi.org/10.1357/002224086788403105

Shchepetkin, A. F., & McWilliams, J. C. (2005). The regional oceanic modeling system (ROMS): a split-explicit, free-surface, topography-following-coordinate oceanic model. *Ocean Modelling*, *9*(4), 347–404. https://doi.org/10.1016/j.ocemod.2004.08.002

Shi, L., Hendon, H. H., Alves, O., Luo, J.-J., Balmaseda, M. A., & Anderson, D. (2012). How

References

Predictable is the Indian Ocean Dipole? *Monthly Weather Review*, *140*(12), 3867–3884. https://doi.org/10.1175/MWR-D-12-00001.1

Shinoda, T., & Han, W. (2005). Influence of the Indian Ocean Dipole on atmospheric subseasonal variability. *Journal of Climate*, *18*(18), 3891–3909. https://doi.org/10.1175/JCLI3510.1

Shinoda, T., Hendon, H. H., & Alexander, M. A. (2004). Surface and subsurface dipole variability in the Indian Ocean and its relation with ENSO. *Deep Sea Research Part I: Oceanographic Research Papers*, *51*(5), 619–635. https://doi.org/10.1016/j.dsr.2004.01.005

Smith, D. M., Cusack, S., Colman, A. W., Folland, C. K., Harris, G. R., & Murphy, J. M. (2007). Improved surface temperature prediction for the coming decade from a global climate model. *Science*, *317*(5839), 796–799. https://doi.org/10.1126/science.1139540

Smyth, W. D., Durland, T. S., & Moum, J. N. (2015). Energy and heat fluxes due to vertically propagating Yanai waves observed in the equatorial Indian Ocean. *Journal of Geophysical Research: Oceans*, *120*(1), 1–15. https://doi.org/10.1002/2014JC010152

Sprintall, J., & Tomczak, M. (1992). Evidence of the barrier layer in the surface layer of the tropics. *Journal of Geophysical Research*, *97*(C5), 7305–7316. https://doi.org/10.1029/92JC00407

Stenseth, N. C. (2002). Ecological Effects of Climate Fluctuations. *Science*, *297*(5585), 1292–1296. https://doi.org/10.1126/science.1071281

Stuecker, M. F., Timmermann, A., Jin, F.-F., McGregor, S., & Ren, H.-L. (2013). A combination mode of the annual cycle and the El Niño/Southern Oscillation. *Nature Geoscience*, *6*(7), 540–544. https://doi.org/10.1038/ngeo1826

Sun, Q., Du, Y., Zhang, Y., Feng, M., Chowdary, J. S., Chi, J., et al. (2019). Evolution of sea surface salinity anomalies in the southwestern tropical Indian Ocean during 2010–2011 influenced by a negative IOD event. *Journal of Geophysical Research: Oceans*, *124*(5), 3428–3445.

https://doi.org/10.1029/2018JC014580

Suzuki, T., Yamazaki, D., Tsujino, H., Komuro, Y., Nakano, H., & Urakawa, S. (2018). A dataset of continental river discharge based on JRA-55 for use in a global ocean circulation model. *Journal of Oceanography*, *74*(4), 421–429. https://doi.org/10.1007/s10872-017-0458-5

Swapna, P., & Krishnan, R. (2008). Equatorial undercurrents associated with Indian Ocean Dipole events during contrasting summer monsoons. *Geophysical Research Letters*, *35*(14), 1–5. https://doi.org/10.1029/2008GL033430

Thompson, B., Gnanaseelan, C., & Salvekar, P. S. (2006). Variability in the Indian Ocean circulation and salinity and its impact on SST anomalies during dipole events. *Journal of Marine Research*, *64*(6), 853–880. https://doi.org/10.1357/002224006779698350

Tozuka, T., & Cronin, M. F. (2014). Role of mixed layer depth in surface frontogenesis: The Agulhas Return Current front. *Geophysical Research Letters*, *41*(7), 2447–2453. https://doi.org/10.1002/2014GL059624

Tozuka, T., Luo, J.-J., Masson, S., & Yamagata, T. (2007). Decadal modulations of the Indian Ocean Dipole in the SINTEX-F1 coupled GCM. *Journal of Climate*, *20*(13), 2881–2894. https://doi.org/10.1175/JCLI4168.1

Trenberth, K. E., Branstator, G. W., Karoly, D., Kumar, A., Lau, N.-C., & Ropelewski, C. (1998). Progress during TOGA in understanding and modeling global teleconnections associated with tropical sea surface temperatures. *Journal of Geophysical Research: Oceans*, *103*(C7), 14291–14324. https://doi.org/10.1029/97JC01444

Tsujino, H., Urakawa, S., Nakano, H., Small, R. J., Kim, W. M., Yeager, S. G., et al. (2018). JRA-55 based surface dataset for driving ocean–sea-ice models (JRA55-do). *Ocean Modelling*, *130*, 79–139. https://doi.org/10.1016/j.ocemod.2018.07.002

References

Ummenhofer, C. C., Biastoch, A., & Böning, C. W. (2017). Multidecadal Indian Ocean variability linked to the Pacific and implications for preconditioning Indian Ocean Dipole events. *Journal of Climate*, *30*(5), 1739–1751. https://doi.org/10.1175/JCLI-D-16-0200.1

Uppala, S. M., KÅllberg, P. W., Simmons, A. J., Andrae, U., Bechtold, V. D. C., Fiorino, M., et al. (2005). The ERA-40 re-analysis. *Quarterly Journal of the Royal Meteorological Society*, *131*(612), 2961–3012. https://doi.org/10.1256/qj.04.176

Vialard, J., & Delecluse, P. (1998). An OGCM Study for the TOGA decade. Part I: Role of salinity in the physics of the Western Pacific fresh pool. *Journal of Physical Oceanography*, *28*(6), 1071–1088. https://doi.org/10.1175/1520-0485(1998)028<1071:AOSFTT>2.0.CO;2

Vimont, D. J., Wallace, J. M., & Battisti, D. S. (2003). The seasonal footprinting mechanism in the pacific: Implications for ENSO. *Journal of Climate*, *16*(16), 2668–2675. https://doi.org/10.1175/1520-0442(2003)016<2668:TSFMIT>2.0.CO;2

Vinayachandran, P. N., & Nanjundiah, R. S. (2009). Indian Ocean sea surface salinity variations in a coupled model. *Climate Dynamics*, *33*(2–3), 245–263. https://doi.org/10.1007/s00382-008-0511-6

Vinayachandran, P. N., Iizuka, S., & Yamagata, T. (2002). Indian Ocean Dipole mode events in an ocean general circulation model. *Deep Sea Research Part II: Topical Studies in Oceanography*, *49*(7–8), 1573–1596. https://doi.org/10.1016/S0967-0645(01)00157-6

Wajsowicz, R. C. (2005). Potential predictability of tropical Indian Ocean SST anomalies. *Geophysical Research Letters*, *32*(24), L24702. https://doi.org/10.1029/2005GL024169

Webster, P. J., & Lukas, R. (1992). TOGA COARE: The Coupled Ocean—Atmosphere Response Experiment. *Bulletin of the American Meteorological Society*, *73*(9), 1377–1416. https://doi.org/10.1175/1520-0477(1992)073<1377:TCTCOR>2.0.CO;2

Webster, P. J., Moore, A. M., Loschnigg, J. P., & Leben, R. R. (1999). Coupled ocean-atmosphere dynamics in the Indian Ocean during 1997-98. *Nature*, *401*(6751), 356–360. https://doi.org/10.1038/43848

Wu, Y., & Tang, Y. (2019). Seasonal predictability of the tropical Indian Ocean SST in the North American multimodel ensemble. *Climate Dynamics*, *53*(5–6), 3361–3372. https://doi.org/10.1007/s00382-019-04709-0

Wyrtki, K. (1973). An equatorial jet in the Indian Ocean. *Science*, *181*(4096), 262–264. https://doi.org/10.1126/science.181.4096.262

Xie, S.-P., & Philander, S. G. H. (1994). A coupled ocean-atmosphere model of relevance to the ITCZ in the eastern Pacific. *Tellus A*. https://doi.org/10.1034/j.1600-0870.1994.t01-1-00001.x

Xie, S.-P., Annamalai, H., Schott, F. A., & McCreary, J. P. (2002). Structure and mechanisms of south Indian Ocean climate variability. *Journal of Climate*, *15*(8), 864–878. https://doi.org/10.1175/1520-0442(2002)015<0864:SAMOSI>2.0.CO;2

Yamagata, T., Behera, S. K., Luo, J., Masson, S., Jury, M. R., & Rao, S. A. (2004). Coupled ocean-atmosphere variability in the tropical Indian Ocean. *Geophysical Monograph Series*, *147*, 189–211. https://doi.org/10.1029/147GM12

Yang, S.-C., Rienecker, M., & Keppenne, C. (2010). The impact of ocean data assimilation on seasonal-to-interannual forecasts: A case study of the 2006 El Niño event. *Journal of Climate*, *23*(15), 4080–4095. https://doi.org/10.1175/2010JCLI3319.1

Yu, L., & Rienecker, M. M. (1999). Mechanisms for the Indian Ocean warming during the 1997-98 El Niño. *Geophysical Research Letters*, *26*(6), 735–738. https://doi.org/10.1029/1999GL900072

Yu, L., & Weller, R. A. (2007). Objectively analyzed air-sea heat fluxes for the global ice- free oceans (1981-2005). *Bulletin of the American Meteorological Society*.

https://doi.org/10.1175/BAMS-88-4-527

Yu, W., Xiang, B., Liu, L., & Liu, N. (2005). Understanding the origins of interannual thermocline variations in the tropical Indian Ocean. *Geophysical Research Letters*, *32*(24), L24706. https://doi.org/10.1029/2005GL024327

Yu, Z., & Potemra, J. (2006). Generation mechanism for the intraseasonal variability in the Indo-Australian basin. *Journal of Geophysical Research*, *111*(C1), C01013. https://doi.org/10.1029/2005JC003023

Zebiak, S. E. (1993). Air-sea interaction in the equatorial Atlantic region. *Journal of Climate*, *6*(8), 1567–1586. https://doi.org/10.1175/1520-0442(1993)006<1567:AIITEA>2.0.CO;2

Zhang, D., McPhaden, M. J., & Lee, T. (2014). Observed interannual variability of zonal currents in the equatorial Indian Ocean thermocline and their relation to Indian Ocean Dipole. *Geophysical Research Letters*, *41*(22), 7933–7941. https://doi.org/10.1002/2014GL061449

Zhang, L., Du, Y., & Cai, W. (2018). Low-frequency variability and the unusual Indian Ocean Dipole events in 2015 and 2016. *Geophysical Research Letters*, *45*(2), 1040–1048. https://doi.org/10.1002/2017GL076003

Zhang, Y., Du, Y., Zheng, S., Yang, Y., & Cheng, X. (2013). Impact of Indian Ocean Dipole on the salinity budget in the equatorial Indian Ocean. *Journal of Geophysical Research: Oceans*, *118*(10), 4911–4923. https://doi.org/10.1002/jgrc.20392

Zhang, Y., Du, Y., & Qu, T. (2016). A sea surface salinity dipole mode in the tropical Indian Ocean. *Climate Dynamics*, *47*(7–8), 2573–2585. https://doi.org/10.1007/s00382-016-2984-z

Zhang, Y., Du, Y., & Feng, M. (2018). Multiple time scale variability of the sea surface salinity dipole mode in the tropical Indian Ocean. *Journal of Climate*, *31*(1), 283–296. https://doi.org/10.1175/JCLI-D-17-0271.1

Zhao, M., & Hendon, H. H. (2009). Representation and prediction of the Indian Ocean dipole in the POAMA seasonal forecast model. *Quarterly Journal of the Royal Meteorological Society*, *135*(639), 337–352. https://doi.org/10.1002/qj.370

Zhao, M., Hendon, H. H., Alves, O., & Yin, Y. (2014). Impact of improved assimilation of temperature and salinity for coupled model seasonal forecasts. *Climate Dynamics*, *42*(9–10), 2565–2583. https://doi.org/10.1007/s00382-014-2081-0

Zheng, F., & Zhang, R.-H. (2012). Effects of interannual salinity variability and freshwater flux forcing on the development of the 2007/08 La Niña event diagnosed from Argo and satellite data. *Dynamics of Atmospheres and Oceans*, *57*, 45–57. https://doi.org/10.1016/j.dynatmoce.2012.06.002

Zheng, F., & Zhang, R.-H. (2015). Interannually varying salinity effects on ENSO in the tropical Pacific: A diagnostic analysis from Argo. *Ocean Dynamics*, *65*(5), 691–705. https://doi.org/10.1007/s10236-015-0829-7

Zheng, F., Zhang, R.-H., & Zhu, J. (2014). Effects of interannual salinity variability on the barrier layer in the western-central equatorial Pacific: A diagnostic analysis from Argo. *Advances in Atmospheric Sciences*, *31*(3), 532–542. https://doi.org/10.1007/s00376-013-3061-8

Zheng, X.-T., Xie, S.-P., Vecchi, G. A., Liu, Q., & Hafner, J. (2010). Indian Ocean Dipole response to global warming: Analysis of ocean–atmospheric feedbacks in a coupled model. *Journal of Climate*, *23*(5), 1240–1253. https://doi.org/10.1175/2009JCLI3326.1

Zhu, J., & Kumar, A. (2019). Role of sea surface salinity feedback in MJO predictability: A Study with CFSv2. *Journal of Climate*, *32*(18), 5745–5759. https://doi.org/10.1175/JCLI-D-18-0755.1

Zhu, J., Huang, B., Zhang, R.-H., Hu, Z.-Z., Kumar, A., Balmaseda, M. A., et al. (2015). Salinity anomaly as a trigger for ENSO events. *Scientific Reports*, *4*, 6821.

References

https://doi.org/10.1038/srep06821

Zweng, M. M., Reagan, J. R., Antonov, J. I., Mishonov, A. V., Boyer, T. P., Garcia, H. E., et al. (2013). *World Ocean Atlas 2013, Volume 2: Salinity*. *NOAA Atlas NESDIS*.

https://doi.org/10.1182/blood-2011-06-357442